UAB
Universitat Autònoma de Barcelona

First-principles simulations of amorphous GeSe compounds for memory selectors

Linda-Sheila Medondjio

Universitat Autònoma de Barcelona

DOCTORAL THESIS

First-principles simulations of amorphous GeSe compounds for memory selectors

Linda-Sheila Medondjio

Dissertation presented to the Department of Physics at the Autonomous University of Barcelona in partial fulfillment of the requirements for the degree of **Doctor of Philosophy in Physics**.

2024

Theory and Simulation group

Catalan Institute of Nanoscience and Nanotechnology

ICN2 Institut Català de Nanociència i Nanotecnologia

EXCELENCIA SEVERO OCHOA

Supervisors	Prof. Pablo Ordejón
	Dr. Roberta Farris
Tutor	Prof. Jordi Sort

To Saa Haniel Andrew

Abstract

Ovonic Threshold Switching (OTS) is a nonlinear current-voltage phenomenon in certain amorphous materials. Recently, OTS selectors based on chalcogenide compounds have been successfully integrated with innovative phase-change memories in 3D cross-point arrays for switching memory. The selector controls data accessibility and transmission quality within and outside the entire memory cell. a-Ge_xSe_{1-x} are among the most promising compounds for this application.

Understanding electronic properties and the related structural features is crucial for designing and optimizing these materials. This work addresses some of the most significant challenges in generating amorphous materials using first-principles calculations (chapter 3). Density functional theory methods are used to gain new insights into the structural and electronic properties of the undoped and doped a-Ge_xSe_{1-x} (chapters 4 and 5). We have developed realistic density functional theory-based structural models of a-Ge_xSe_{1-x} without resorting to experimental information or adjusted interatomic potential. A series of a-Ge_xSe_{1-x} with three stoichiometries (x = 0.4, 0.5, and 0.6) and dopants (Si, As, P, S, Te) with various concentrations (1%, 3%, 5%,7%, 10%, 15%) has been generated with the melt and quench protocol.

We analyze each sample's structural and electronic properties and unveil the link between each localized state's electronic and structural properties within the mobility gap. Our results indicate that the a-Ge_xSe_{1-x} is mainly Ge(3): Se(3) coordinated. The results show that there is Ge and Se clustering in Ge and Se-rich structures, respectively; the Ge-rich structures tend to have a larger coordination number, opposite to the Se-rich structures. Well-defined Ge-Se first-neighbor shells are found, similar to the Ge-Se bond in the GeSe crystalline structure. We have analyzed the electronic properties, including the inverse partition ratio and the density of states. We have also analyzed the correlation between their most relevant features and the microscopic structure of our models. We have found that the mobility gap is very sensitive to the composition around the stochiometric GeSe compound, and in particular, that it decreases with Ge concentration, to the point of becoming essentially metallic already for x=0.6.

We show the structural motifs at the origin of the localized states in the mobility gap. Specifically, we found that the localized states are predominantly due to the Se-Se bonds and a minor contribution to Se lone pairs and tetrahedra. These bonding

configurations are at the origin of conduction and valence band tail states, leading to nonlinear conduction in OTS. The a-$Ge_{0.6}Se_{0.4}$ sample is metallic.

We have also generated and studied the structure of the three a-Ge_xSe_{1-x} compounds in the presence of dopants species (Si, As, P, S, Te) with various concentrations (1%, 3%, 5%,7%, 10%, 15%). The dopants behave similarly with their iso-valent hosting ions, with some delicate differences. We found a new kind of structural motif, the germanium chalcogenide cubane, symbolizing the presence of structurally ordered assemblies in disordered materials. The structural origin of localized states has also been explored. Bicoordinated and pentacoordinated Ge give rise to localized states in all the dopants. For the Si-doped and pnictogen-doped a-Ge_xSe_{1-x}, we observe the presence of defect states originating from substitutional doping. In the case of chalcogenide doping, we also observe the chalcogenide lone pairs, homopolar bonds, and the valence alternation pair, all of which yield localized states.

These results are useful to understand the electronic properties of these materials and could help to provide guidelines for improving the memory-switching performance of a-Ge_xSe_{1-x}.

Acknowledgments

Completing this PhD thesis has been a challenging yet rewarding journey, made possible by the support and guidance of many individuals. I would like to take this opportunity to express my heartfelt gratitude to all those who contributed to its completion.

I am especially grateful to my supervisors, Pablo Ordejón and Roberta Farris, for believing in me and my work. Their insights and feedback have been vital in bringing this research to fruition, and their expertise has significantly shaped both this thesis and my research skills.

I would also like to express my gratitude to He Xu and Matthieu Verstraete who devoted his time to guiding and encouraging me through the most challenging moments of this research.

I extend my sincere gratitude to Sergiu Clima, Arrigo Calzolari, Francesco Tavanti, Amine Slassi, and many others for sharing their knowledge and experience with me.

Special thanks are due to the honorable members of the jury, whose insightful remarks will enrich my training and this work.

I also acknowledge the fruitful discussions I had with all current and former members of the Theory and Simulation group at ICN2 and their moral support.

Finally, I want to thank my lovely parents, brothers, and sisters for their unwavering support and love throughout my academic journey.

Contents

1 Introduction

Information and communication technologies have been historically all-silicon-based platforms. The current and major worldwide drive for the fast and efficient processing of large data sets forces the semiconductor industry to enhance device density and achieve robust communication optimization. This provides a unique opportunity and a clean slate to deploy novel technologies based on innovative materials and devices. Thus, innovative approaches for fabricating disruptive nanoelectronic solutions are urgently needed. This requires a fast exploration of materials' properties (e.g., structure, composition, doping, stability, electrical and thermal response) and establishing clear links between these properties and performance in novel, unexplored architectures. Inspired by the power efficiency of the human brain, synaptic electronics [GV16; KYW13; Mer+14] and neuromorphic computing [Mea90; YSS12] emerged as top candidates to reduce the power consumption of big data analysis and perform robust and fault-tolerant computation. The idea behind such a novel computation scheme is to process the information similar to what happens within the brain, where memory and computing are co-located within the same biological system.

Among the emerging technologies for neuromorphic computing, switching memories such as phase-change memories (PCMs) and resistive random access memories (RRAM) [Bur+10; WY19] are the most extensively researched by the semiconductor industry. These memories are integrated into complex 3D cross-point arrays, interconnected by selectors that control data access and transmission quality within and outside the memory cells [AT16]. Selectors act as dynamic switches, optimizing the encoding mode to minimize bit error rates during data transmission [Hua+13].

Developing these new electronics relies on designing and characterizing materials and devices. Albeit implicitly interconnected, the interplay between the materials' characteristics and device performance is hard to determine. Materials modeling can play a key role in this process by minimizing experimental trials and promoting efficient top-down and bottom-up design approaches.

Amorphous chalcogenide alloys are emerging as a potential alternative to address the scaling limitations of current Si-based technologies. New disruptive electronics based on amorphous chalcogenides have emerged, such as in-memory devices, where data are processed within the same element as the memory. This new

disruptive electronic helps in data storage and energy scavenging applications thanks to its significant non-linear optical and electrical properties, along with its low vibrational thermal conductivity.

While extensive research has focused on GeTe as a prototypical phase-change material, the quasi-stoichiometric GeSe compound remains far less understood. Nonetheless, GeSe has been recently exploited for developing selectors units [Cha+19]. However, there is insufficient information about the structural properties of amorphous GeSe (a-GeSe) materials, either from experiments or theory [Tav+20]. The first results indicate that amorphous GeSe exhibits ovonic electrical switching, and even moderate modulation of the stoichiometry ratio significantly impacts the device's electrical response, affecting both I-V characteristics and power dissipation [Liu+19b; Yoo+18]. However, the origin of this behavior remains unknown. Theoretically, understanding the interplay between local-order structures, trap states, and the resulting electrical response poses a significant challenge: it requires the ability to model large systems at the atomistic level, including their electronic structure. Due to the inherently disordered nature of amorphous materials, this necessitates large-scale first-principles simulations, which involve constructing extensive atomistic models to accurately represent the material. A critical aspect is the capability of treating/understanding systems with a high degree of structural disorder, including the role of defects and impurities without specific experimental results of a-GeSe.

In this thesis, we aim to develop a realistic model based on first-principles simulations for a-GeSe and investigate its structural and electronic properties. This includes the structure of the material, the atomic coordination, the short- and medium-range order (S-MRO) and the electronic properties. We also want to examine the existence of localized electronic states induced by structural defects in the amorphous network, and explore the effect of the presence of deviation from stoichiometry, as well as of dopants, on the structure and the electronic properties of the material. We aim to explore the interplay between structural and electronic properties without relying on experimental information or adjusted empirical potentials.

The thesis is organized into the following chapters: chapter 2 provides an overview of the current knowledge on crystal and amorphous structures in general, with a focus on crystalline GeSe and a-Ge_xSe_{1-x}. Chapter 3 introduces the fundamental concepts, theories and tools used to study the crystalline structure and generate a-Ge_xSe_{1-x} along with the computational details. Chapter 4 discusses the electronic and structural properties of a-GeSe, while chapter 5 examines the electronic and structural properties of doped a-Ge_xSe_{1-x}.

2 State-of-the-art in amorphous semiconductors

2.1 The Crystalline and Amorphous Materials: Historical Perspectives and Technological Implications

The history of civilization is deeply intertwined to the discovery and development of new materials. Historically, entire periods were named after the material predominantly used during that time. We distinguish the Stone Age, the Bronze Age, and the Iron Age. In the 18th and 19th centuries, scientists started to question the structure of matter. Later in the 20th century, scientists such as Thomson [Tho13a; Tho13b; Tho97], Rutherford [Rut11; Rut19; Rut20] and Bohr [Boh13a; Boh13b], proposed atomic models to explain experimental observations [Ste23]. Before 1900, fractography studies were used to coin the term amorphous structure to a structure with a formless fracture surface. With the advent of X-ray diffraction experiments later, their non-crystallinity was evidenced. They do not exhibit sharp reflections associated with a crystalline structure [Bag74]. Solid-state materials could be classified into crystalline and amorphous. A perfect crystal is a solid material with a unit cell and translational symmetry—when extended in 3 dimensions, the unit cell gives the structure of the materials. In contrast to crystalline materials, the amorphous structure is characterized by the lack of long-range periodicity (the absence of a regular, repeating, and well-defined structural pattern over extended distances). While adopting the absence of long-range order as an essential criterion, the terms 'non-crystalline,' 'glass,' 'vitreous,' and 'amorphous' are often used synonymously.

In his seminal work in 1932, Zachiaren [Zac32] defined glass as supercooled liquids and investigated its structural arrangement. In 1964, Bernal [Ber64], by analyzing the structure of liquids for the first time, used the random packings of spheres model to define liquid as homogeneous with irregular assemblies of molecules. The lack of long-range order in amorphous materials results in the absence of Bloch states [Blo29], which in turn reduces electron mobility and conductivity. Due to their disordered structure, amorphous materials were once thought to have no potential for technological applications. Additionally, doping amorphous materials is often challenging and, in some cases, impossible [Bah18]. Undoped amorphous

chalcogenides (a-CG) have limitations that make them unsuitable for specific applications. Due to their lower electrical conductivity, undoped chalcogenides are unsuitable for high-power electronic devices. The amorphous chalcogenides have lower thermal stability than crystalline materials. Consequently, they can degrade at elevated temperatures, making them unsuitable for applications requiring exposure to extreme heat, such as aerospace.

However, amorphous materials have many advantages over crystalline materials due to their non-periodic atomic structure, allowing a more straightforward manufacturing method, such as deposition techniques like sputtering or evaporation. When engineered properly, amorphous semiconductors can have enhanced electron mobility, making them suitable for thin-film transistor applications.

To fine-tune the properties of amorphous GeSe for specific applications, alloying and doping with other materials have been explored. Due to the lack of long-range order in amorphous materials, it was long believed that they could not exhibit semiconductor properties. In 1955, Goryunova and Kolomiets discovered that one of their amorphous compositions, $TlAsSe_2$, demonstrated the typical semiconductor conductivity behavior [GK55]. Anderson introduced the concept of localization to explain hoping conduction on compensated crystalline semiconductors [And58]. In 1960, Ioffe and Regel [IR60] demonstrated that the band gap depends on short-range order instead of long-range order in the lattice. They proposed that the first coordination number of the crystal is maintained in the amorphous structure. Mott and Twose [MT61] showed that all states in a one-dimensional energy band became localized as soon as the disorder was introduced. The *mobility edge*, which separates localized energy states from extended electronic states, was first introduced by Cohen et al. [CFP67]. They describe an ideal covalent random network structure with extended wave functions, where localized states exist in the gap between the valence band (E_v) and the conduction band (E_c). At both E_v and E_c, the electron and hole mobility drops sharply, while the Fermi level lies near the center of the gap. Various deviations exist from ideal covalent random networks, such as vacancies, dangling bonds, and chain ends, leading to localized states with various energies and a curve of non-monotonic density of localized states.

2.1.1 Structural characteristics of amorphous solids: Short-Range and Medium-Range Order

The term glassy has been reserved for amorphous solids, prepared by melt-quenching, that exhibit a glass transition [KS15]. Glassy materials are subsets of amorphous solids; all glasses are unstructured, but all amorphous are not necessarily glasses

[Liu+19a]. The amorphous Ge_xSe_{1-x} are glass-forming systems for $0 \leq x \leq 0.43$ [ATB75; Zei+17]. On a general footing, short-range order in disordered solids is similar to its crystalline counterpart materials in the same composition. But bonding angles between adjacent atoms deviate slightly, and the dihedral angle among them causes disorder in the rings, disrupting the periodicity. Figure 2.1 deepens our understanding of the loss of long-range order in an amorphous structure and vividly highlights the preservation of short-range order (SRO) in amorphous structure and structural distinctions.

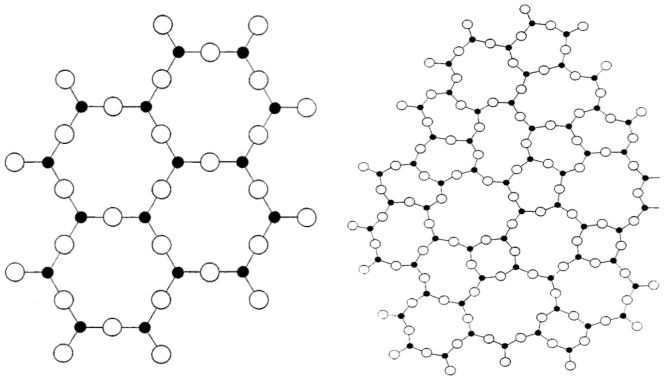

Figure 2.1: Comparison of short-range order in crystal (left) and amorphous material (right) [Zac32] showing the preservation of the short-range order in amorphous

Unveiling the relationship between structure and macroscopic properties of amorphous materials has been a fundamental problem due to their lack of periodicity. Although SRO implies a similar coordination and bond shortest distance between the crystal and the amorphous phases, only slight distortion destroys the long-range order. One example is the atomic coordination in the crystal and glasses As_2S_3, which are almost the same [Luc72]. Nevertheless, there are amorphous materials that do not have the same SRO as in the crystalline state. There has been a debate in the literature on the SRO of the germinate chalcogenide glasses (Ge_xCh_{1-x} where Ch=S, Se, Te), the subject of our studies. According to [E77; FT74; FWB79; PSV80; TSS82] amorphous GeSe relaxes into a 4:2 coordinated structure each atom satisfying its normal valence requirements different from its crystalline counterparts. On the contrary, the local structure of amorphous GeSe studied by [Oya+81; Tro+77] reveal a 3:3 coordination for Ge and Se, respectively, which is the same as in the crystal.

Based on the bonding type among atoms, amorphous semiconductors can be classified into: (1) ionic, (2) covalent, (3) metallic, (4) van der Waals, and (5) hydrogen

bonding. The compounds of interest here, namely the germinate chalcogens with sulfur (S), selenium (Se), and tellurium (Te), fall under covalently bonded glasses. Covalent glasses have a much higher SRO [Zhd+79] than metallic glasses [SM75; TJD00].

In addition to short-range order, the study of these amorphous chalcogenides has revealed the presence of medium-range order (MRO) as introduced by Elliot [Ell89]. The MRO results from an extended order beyond the SRO. There are three types of MRO: small-scale medium-range order (3-5 Å), intermediate-scale medium-range order (5-8 Å), and large-scale medium-range order (8-10 Å) as reported by Elliot [Gas79].

2.1.2 Electronic structure in amorphous semiconductors: models and insights

The band theory in quantum mechanics was derived to describe a crystal's optical [BC69] and electronic properties using the Bloch theorem [Blo29] to account for the periodicity of the atomic arrangement. When applied to crystal, it helps to derive bands, which refer to ranges of energy in which electronic states are present. Consequently, it allowed us to distinguish between the allowed energy bands and the electronic band gap. The critical difference between the crystal and the amorphous semiconductor is that crystalline material has extended states in the valence and conduction band and no mobility edge. Figure 2.2 panel (a) shows the band diagram of a crystalline structure. An energy band gap separates the conduction and the valence band. Furthermore, the conduction and valence band edges are delimited by a sharply defined edge where the DOS goes to zero. In contrast, the amorphous structure has some localized states that extend beyond the mobility edge. While defects create some of these localized states, most are made by losing long-range order and are unique to amorphous solids. Anderson [And58] was the first to show systematically that the variation of energy site by site due to the disorder in the lattice will result in localized states in the band structure. Various models have been proposed to explain the high defect density and the band structure observed in amorphous semiconductors.

Cohen-Fritzsche-Ovshinsky (CFO) model

In 1968, Cohen-Fritzsche-Ovshinsky [CFO69] proposed a model to explain the electrical switching in chalcogenide glasses. In the CFO model (Figure 2.2 b), the disorder is significant, causing the overlap of the band tail states in the middle of the gap, leading to the appreciable density of the states in the mobility gap.

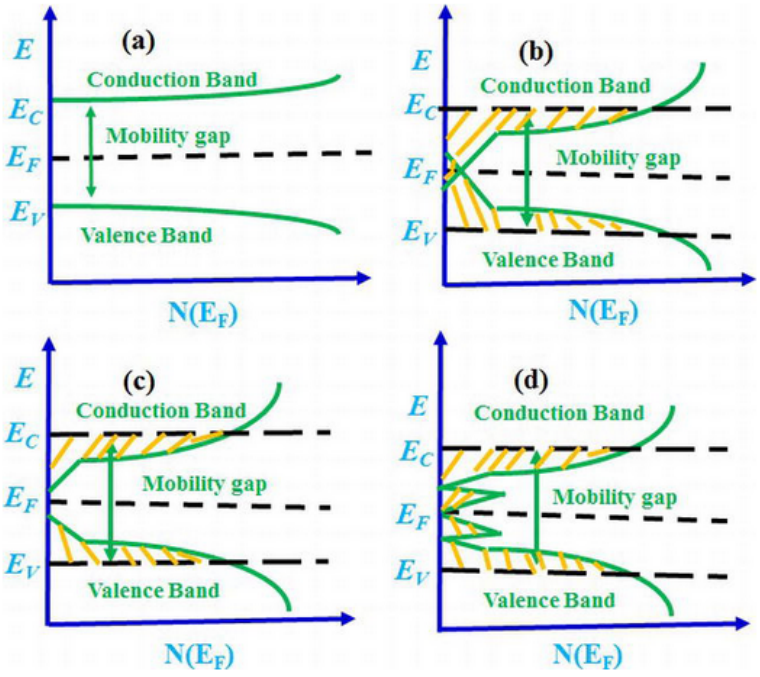

Figure 2.2: Schematic Density of States models for semiconductors materials [GZ14]. (a) DOS of a crystalline semiconductor, (b) DOS models proposed by Cohen, Fritzsche, and Ovshinski (CFO) [CFO69], showing the localized states extending across the forbidden gap (c) DOS models proposed by Mott [Mot98], showing the smearing out of the band edges caused by local variations in the lattice parameters and (d) DOS models proposed by Marshall and Owen [MO71] containing deep donors below acceptors.

The overlapping of states in the tails of the conduction and valence bands lead to a redistribution of electrons, forming negatively charged occupied states in the conduction band tail and empty states in the valence band, which are positively charged. The CFO cannot describe some of the transparency observed in some chalcogenide semiconductor below a well-defined absorption edge.

Davis and Mott (DM) model

Davis and Mott [DM70] took on the CFO model due to its shortcomings in describing the transparency observed in some chalcogenides. They modified it by considering a band of localized states a few tenths of an electron volt near the center of the gap. Figure 2.2 c illustrates the Davis Mott Model, where E_C and E_V represent

the energies that separate the extended and localized states in the valence and conduction band, respectively.

Marshall-Owen model

Cohen-Fritzsche-Ovshinsky previously assumed that the disorder-induced tail state defects would cover up the defects such as dangling bonds, vacancies, interstitials, impurities, etc., present in crystalline and amorphous structures. Marshall and Owen [MO71] instead proposed a model wherein the defect states lead to localized energy states in the form of electron and hole traps in the band gap. The acceptor and the donor states are alike. They suggested that the position of the Fermi level is determined by the acceptor and donor states, which self-adjust themselves such that the Fermi level remains in its intrinsic position. This auto-compensation mechanism is essential because even a tiny fraction of the defect state in the band gap can make the doping ineffective.

Street and Mott model

Despite the strong evidence of high density of defect states in chalcogenide materials from photoluminescence [SSA73],[SSA74a], [SSA74b], field effect[MO71], photoconductivity, drift mobility [MO71], and a pinned Fermi energy [MD71], the absence of spin magnetism in the Electron Spin Resonance (ESR) has made it challenging to chemically identify the defect state in the bonding configuration in the band gap of chalcogenide materials. Anderson [And58] proposed a model in which a pair of electrons in the same state of amorphous material can be attractive because of the coupling to atomic motion. Street and Mott [SM75] derived a model of charged defects instead of the neutral dangling bond in amorphous chalcogenides, assuming that a large density of dangling bond in the material acts both as an acceptor and donor and that the atomic motion lower sufficiently the total energy to maintaining the effective correlation energy negative, resulting in a charged state. In their work, Street and Mott consider the As_2Se_3 containing 10^{18}-10^{19} cm^{-3} dangling bonds. Because of topological constraints, the normal lattice configuration of Se(2) and As(3) can not be satisfied; dangling bonds exit, and those could be occupied by 0, 1, or 2 electrons labeled D^0, D^+, D^- respectively. The following reaction occurs because of the strong lattice distortion induced by the modification of the electron occupation of the dangling bond.

$$2D^0 \rightleftharpoons D^+ + D^- \tag{2.1}$$

The D^+ center is particularly attracted by the lone pair that constitutes the

edge of the valence band. Such bonding involving the lone pair (LP) causes a release of energy because of its involvement in a deep bonding state. The extra electrons introduced in D^+ occupied the next highest state, the conduction-band-like antibonding orbital, in contrast to the D^+, D^- forms an acceptor level. The mechanism follows: the two electrons of D^- cannot form a covalent bond with the neighboring atom but instead occupy a valence-band-like lone pair state. This model effectively explains the diverse externally induced phenomena in chalcogenide semiconductors, including photoconductivity, thermal process, luminance, etc.

Kastner Adler and Fritzsche (KAF) model

Kastner, Adler, and Fritzsche's [KAF76] take on the Mott and Streets model and proposed a Valence Alternation Pair (VAP) model to describe the bonding configuration that gives rise to positively and negatively charged states. They built upon Ovshinsky's idea that suggested the interaction between the LP of different atoms and their local environment causes localized states, showing that the specific interactions between the non-bonding orbitals give rise to VAP. Kastner defined the valence alternation by considering two chalcogens in their normal lattice configuration (2-fold), ground state, form instead one positively charged 3-fold coordinated atom and a negatively charged singly coordinated atom through the involvement of lone-pair electron. The VAP is the lowest energy defect because the total number of bonds is conserved.

Let C labeled a chacogen atom. The lowest energy-neutral dangling bond defect is C_3^0, where "3" is the coordination and "0" indicates neutrality. However, it is unstable and then decays to C_3^+ and C_3^- following the equation 2.2. The subscript denoted the coordination of each of them.

$$2C_3^0 \rightarrow C_3^+ + C_3^- \tag{2.2}$$

This reaction is endothermic. Breaking one of the three bonds of C_3^-, it takes its normal lattice configuration C_2^0 converting the nearest C_2^0 site into a single coordinated atom C_1^-. The following reaction captures the process

$$C_3^- + C_2^0 \rightarrow C_2^0 + C_1^- \tag{2.3}$$

Summing the two equations give

$$2\mathrm{C_3}^0 \rightarrow \mathrm{C_3}^+ + \mathrm{C_1}^- \tag{2.4}$$

2.2 Crystalline GeSe

2.2.1 The structure of crystal GeSe

At atmospheric pressure, GeSe crystallizes into an orthorhombic structure with a Pnma space group. The GeSe crystal structure is shown in Figure 2.3. The unit cell consists of two layers, each comprising four atoms. The layers are weakly coupled by van der Waals interactions along the c-axis. Along the b-axis, the atoms formed a zigzag Ge-Se chain and an armchair Ge–Se chain along the a-axis. The atoms within a layer form strong covalent Ge–Se bonds. Each atom of Ge has 3 Se neighbors, and each atom of Se has 3 Ge neighbors.

In this chapter, we have calculated the properties of the crystalline GeSe phase, which we present below. The calculation has been done using the parameters described in section 3.7. The obtained cell parameters are a = 3.802 Å, b = 4.471 Å, and c=10.946 Å. The experimental values are a=3.83 Å, b=4.39 Å and c=10.83 Å [Sis+17]. Within the layer, we obtain a bond length of 2.59 Å in agreement with the GGA calculation [Yan+19], which also reports a bond length of 2.59 Å.

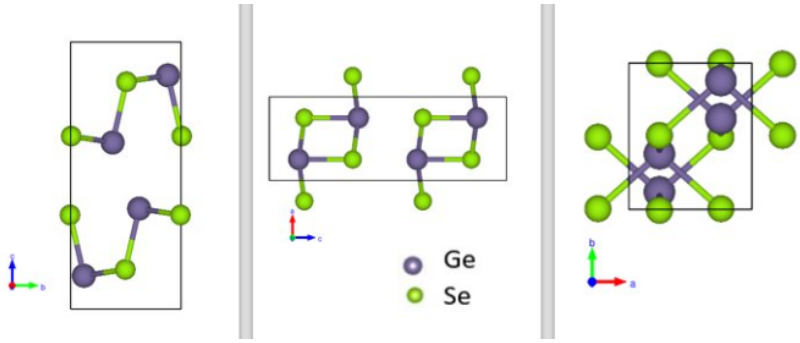

Figure 2.3: The crystal structure of orthorhombic GeSe (space group: Pnma). The layers are coupled weakly by a van der Waals interaction along the c-direction. Atoms within a layer are covalently bonded and formed armchair along the b-axis and zigzag chain along the c-axis

2.2.2 Electronic structure of crystal GeSe

Here we present the result for the crystalline phase of GeSe. They will serve as a reference for our results for the amorphous phases.

To understand the coordination of the crystal we now analyse the electronic occupation of each species according to the octet rule.

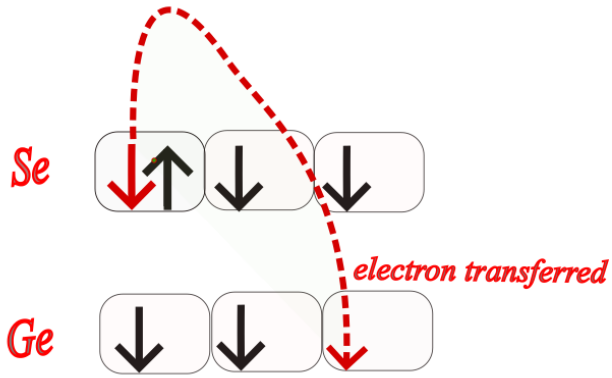

Figure 2.4: p shells orbital diagram of Ge and Se and their bonding mechanism

Figure 2.4 shows the electronic occupation of the p orbitals of Se and Ge in the free atom (the s orbital is doubly occupied). To satisfy the octet rule, Se would like to form two covalent bonds while Ge would need four covalent bonds. However, the coordination in the crystal is 3:3. This bonding structure can be understood if one p electron of Se is transferred to the p states of Ge. In that way, both species satisfy the octet rule by forming three covalent bonds, as in the experiment crystalline structure. The electron transfers from Se to Ge does not really occur as the chemical bonds are not completely covalent but rather ionic, due to the high electronegativity of Se in comparison to Ge (2.4 and 1.8, respectively). As found in the Mulliken charge analysis, the Se atom has a charge of 6.118, and the Ge has a charge of 3.881. A covalent bonding with a strong polar character for c-GeSe is therefore suggested.

We now discuss the electronic structure of the GeSe crystal. Figure 2.5 shows the band structure along the high symmetry points in the Brillouin zone. We obtain an indirect band gap of 0.724 eV, compared to the experimental value of 1.14 eV [Liu+19c]. This underestimation is common to the semi-local functional. Our values are similar to those obtained by other authors using similar functionals: 0.81 eV by Liu et al. [Liu+19c] and 0.85 eV by Hao et al. [Hao+16].

Figure 2.5 shows the projected density of states of Ge (blue) and Se (red) and the total DOS (black) of the GeSe crystal. The conduction band has more of a Ge character, while the valence band has more weight on Se.

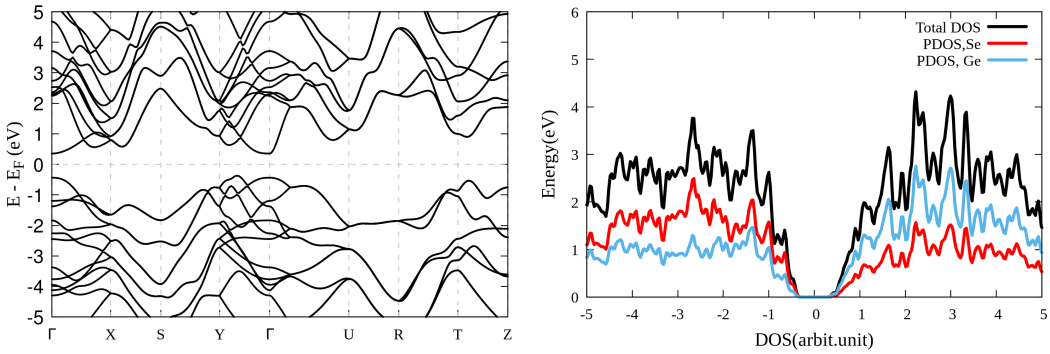

Figure 2.5: The electronic band structure (left) and the Density of states (DOS) in black and the partial DOS of Se in red and Ge in red of the orthorhombic GeSe crystalline structure(right). The energy levels are Fermi level shifted.

DFT+U

One of the shortcomings of the DFT calculation is its accuracy in describing one site's strong electron interactions when solving the Schrodinger equation due to the approximate exchange-correlation functional choice. The DFT + Hubbard (DFT+U) correction helps account for the on-site electron interactions and, thus, overcomes the underestimation of the electronic band gap by the standard DFT approach. Following the protocol and approach proposed by [ACB15], the U term is applied to c-GeSe such that $U_{\mathrm{Se}} = 14.25 \times U_{\mathrm{Ge}}$. Table 2.1 shows the different values of the band gap obtained for various values of U_{Se} and U_{Ge}.

U_{Ge}	U_{Se}	E_g
0.0	0.0	0.72
0.1	1.425	1.0882
0.12	1.71	1.1156
0.14	1.995	1.1434
0.16	2.2800	1.1715
0.20	2.85	1.2299

Table 2.1: Table showing the U_{Se} and the U_{Ge} such that $U_{\mathrm{Se}} = 14.25 \times U_{\mathrm{Ge}}$ and the corresponding band gap E_g. The value colored in red corresponds to the experimental band gap observed in c-GeSe [Yan+19].

Figure 2.6 shows the band structure of the c-GeSe obtained from the DFT(black

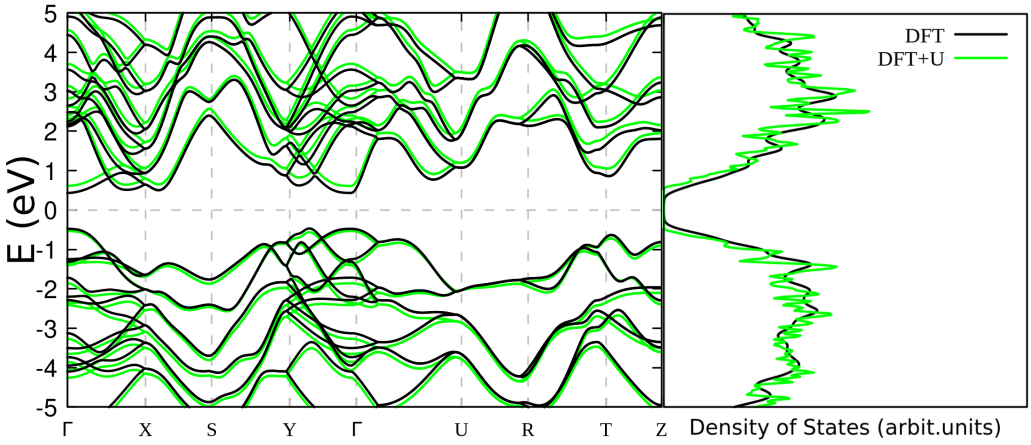

Figure 2.6: Band structures obtained from density functional theory calculations (black curve) and density functional theory plus the Hubbard correction (green curve), with U_{Ge} = 0.14 eV and U_{Se} = 1.995 eV.

curve) and DFT+U (green curve). The electronic band gap found is E_g = 0.72 eV using the exchange-correlation functional (GGA-PBE), which tends to underestimate band gaps, whereas using the (GGA(optB88-vdW)) in [Yan+19], E_g=0.89 eV.

Adding the Hubbard term increased the value of the electronic band gap to the experimental value of 1.14 eV. Except for the numerical values of the bandgap observed in figure 2.6, the DFT and the DFT+U give very similar electronic structures and do not affect the structural motifs, giving rise to localized states within the mobility gap.

3 Methodology

This chapter introduces the fundamental concepts, theories, and tools applied to generate and describe the amorphous structures from structural and electronic standpoints. It is divided into six sections: the first five sections introduce the theoretical and computational frameworks adopted. Topics include the density functional theory, pseudopotentials, basis sets, the SIESTA method, and analysis tools, while the last section outlines the computational details used to generate, relax, and obtain the final structures studied in the following chapters.

3.1 Density Functional Theory

3.1.1 Quantum mechanics and the Born-Oppenheimer approximation

The discovery of quantum mechanics brought the hope of explaining our everyday surroundings using equations at the atomic scale. In 1926, Erwin Schrödinger formulated an equation describing how a physical system's quantum state evolves over time. While the time-dependent version of the equation provides a complete solution that includes all possible effects, here we are particularly interested in studying the ground state of a system. For this reason, the time-independent Schrödinger equation is used, simplifying the analysis by eliminating time evolution and focusing on determining the system's stationary states.

The first step in determining the ground state properties of a quantum system is to solve the time-independent Schrödinger equation, which can be written as:

$$\hat{H}\psi = E\psi \tag{3.1}$$

where $\hat{H}$ is the Hamiltonian operator, ψ is the wave function of the quantum system, and E is the system's energy.

The wave function $\psi(\mathbf{x}_1, ..., \mathbf{x}_N)$ depends on the coordinates of the particles in the system $\mathbf{x}_i \equiv (x_i, y_i, z_i)$ [1]. It is not an observable, but the square of the absolute value of the wave function, $|\psi|^2$, represents the probability density of finding the particles

1 For simplicity we do not include the spin of the particles in this discussion

at the positions $\mathbf{x}_1, ..., \mathbf{x}_N$. The integral over all space must equal 1, which ensures that the total probability of finding the system in any possible configuration is 100%.

$$\int |\psi|^2 d\mathbf{x}_1, ..., d\mathbf{x}_N = 1 \tag{3.2}$$

The particle density is obtained by:

$$n(\mathbf{x}_1) = N \int |\psi|^2 d\mathbf{x}_2, ..., d\mathbf{x}_N \tag{3.3}$$

We now focus on condensed matter systems formed by electrons and nuclei, for which the general Hamiltonian is

$$\begin{aligned} \hat{H} = & -\frac{\hbar^2}{2m_e}\sum_i^n \nabla_i^2 - \frac{\hbar^2}{2M_A}\sum_A^M \nabla_A^2 + \sum_{i=1}^n \sum_{j>i}^n \frac{e^2}{|\mathbf{r}_i - \mathbf{r}_j|} + \sum_{A=1}^M \sum_{B>A}^M \frac{Z_B Z_A e^2}{|\mathbf{R}_A - \mathbf{R}_B|} \\ & - \sum_{i=1}^n \sum_{A=1}^M \frac{Z_A e^2}{|\mathbf{r}_i - \mathbf{R}_A|} + \hat{V}_{ext} \\ & = \hat{T}_e + \hat{T}_N + \hat{V}_{ee} + \hat{V}_{NN} + \hat{V}_{eN} + \hat{V}_{ext} \end{aligned} \tag{3.4}$$

The subscripts i and j represent the electrons, while the subscripts A, and B represent the nuclei. n and M are the number of electrons and nuclei in the system respectively. $\hat{T}_e$ and $\hat{T}_N$ are the kinetic energy of the electron and nuclei, respectively. $\hat{V}_{ee}$ and $\hat{V}_{NN}$ are the electron-electron and nuclei-nuclei Coulomb repulsion respectively. $\hat{V}_{eN}$ is the interaction between electrons and nuclei. $\hat{V}_{ext}$ accounts for external potentials like magnetic or electric fields.

The wave function in this system is a function of the coordinates of all the electrons and nuclei. It is therefore a very complex mathematical object that cannot be obtained exactly even for the simplest systems. For realistic systems approximations must be made which are described in the following.

The adiabatic or Born-Oppenheimer approximation

The first approximation we use is the adiabatic approximation, which decouples the motion of the nuclei and the electrons. This approximation finds its foundation because the electrons move faster than the much heavier nuclei. Consequently, during a cycle of electron motion, the change in nuclear configuration is negligible.

Thus, it can be assumed that the electrons are in the adiabatic equilibrium of their ground state with respect to the position of the nuclei at all times. Hence, we can effectively treat the motion of electrons and nuclei as decoupled and search for solutions to the electronic part of the wave function while keeping the nuclei's positions fixed (Born Oppenheimer approximation [BO27]). i.e., reducing the problem to the solution of the dynamics of the electrons in a frozen configuration of the nuclei:

$$\left[-\frac{\hbar^2}{2m_e} \sum_{i=1}^{n} \nabla_i^2 - \sum_{i=1}^{n} \sum_{A=1}^{M} \frac{Z_A e^2}{|\mathbf{r}_i - \mathbf{R}_A|} + \sum_{i=1}^{n} \sum_{j>i}^{n} \frac{e^2}{r_{ij}} \right] \psi = E\psi \tag{3.5}$$

$$\psi(\{\mathbf{r}_1, \ldots, \mathbf{r}_n\}, \{\mathbf{R}_1, \ldots, \mathbf{R}_M\}) = \Phi_e(\mathbf{r}_1, \ldots, \mathbf{r}_n \{\mathbf{R}_1, \ldots, \mathbf{R}_M\}) \phi_n(\{\mathbf{R}_1, \ldots, \mathbf{R}_M\}) \tag{3.6}$$

Where r_{ij} is the distance between electron i and electron j. Φ_e is the electronic wave function dependent on the electron's positions with the nuclei positions as parameters since they are considered fixed, and ϕ_n represents the nuclear wave function. A further common approximation that we use throughout this work is to treat the nuclei as a classical particle, following Newton's dynamics, while the electrons are treated as quantum particles.

However, solving this equation is still complex, even for small systems. Further simplifications that allow the total energy calculations to be performed accurately and efficiently for most systems of interest can be introduced. These include the Hartree-Fock (HF) approximation or Density Functional Theory (DFT) method to treat the electron-electron interactions.

3.1.2 Hohenberg-Kohn theorems

In 1964, Hohenberg and Kohn [HK64] lay the foundation of the density functional theory (DFT), establishing a crucial link between the electronic density n(r) in a system's ground state and the external potential U. They showed that the density uniquely determines the many-body wave function in its lowest energy state. n(r), in principle, contains all the information of the many-body wave functions. Two many electron systems differ by the external potential U and the number of electrons. Hohenberg and Kohn next showed that if the ground state density n(r) of the many-electron system is known, the external potential in which the electron resides can be determined up to an overall constant.

Following the Hohenberg-Kohn theorem, consider a many-electron system where electrons interact with each other via the Coulomb potential while moving in a potential U and satisfying the Schrödinger equation. If the charge density as a

function of position is known, then the potential U could be determined, allowing us to solve for all the properties of the system. Consequently, the ground state energy can be expressed as:

$$\varepsilon[n] = T[n] + U[n] + U_{ee}[n] \tag{3.7}$$

Hohenberg and Kohn next observed that if one can find the functional $\varepsilon[n]$ then the true ground-state density $n(r)$ minimizes it, subject only to the constraint that

$$\int d\mathbf{r}\, n(\mathbf{r}) = N \tag{3.8}$$

The energy functional can be written as

$$\varepsilon[n] = \int d\mathbf{r}\, n(\mathbf{r})U(\mathbf{r}) + F_{HK}[n], \tag{3.9}$$

where F_{HK} is the sum of the kinetic and the Coulomb energies:

$$F_{HK}[n] = T[n] + U_{ee}[n]. \tag{3.10}$$

$F_{HK}[n]$ is a universal function of density independent of $U(\mathbf{r})$. The functional $F_{HK}[n]$ is the minimum over all wave functions producing density $n(\mathbf{r})$

$$F_{HK}[n] = \min_{\psi \to n} \langle \psi | T + U_{ee} | \psi \rangle. \tag{3.11}$$

The ground state ε_0 is then defined as:

$$\varepsilon_0 = \min_{\psi \to n} \left[F_{HK}[n] + \int U(\mathbf{r}) n(\mathbf{r})\, d\mathbf{r} \right] = \min_{\psi \to n} \varepsilon[n] \tag{3.12}$$

The functional F in quantum mechanics is universal and independent of the potential $U(\mathbf{r})$. The functional F is a helpful tool to solve quantum mechanics problems, but its form is unknown; for that reason, some approximations are introduced. Through years of experimentation and observation, researchers have developed functional forms that hold a great deal of accumulated physical insight.

3.1.3 Kohn-Sham approach

The Kohn-Sham approach represents the electrons as a set of non-interacting one-particle wave functions that generate the same electron density as the actual system of interacting particles. This leads to the replacement of the many-body problem by

an independent one-particle problem placed in an effective potential that considers both exchange and correlation effects [KS65a].

The ground state density of the non-interacting particles is given by:

$$n(\mathbf{r}) = \sum_{\sigma} \sum_{i=1}^{n} |\Psi_i^{\sigma}(\mathbf{r})|^2 \tag{3.13}$$

Here, $\Psi_i^{\sigma}(\mathbf{r})$ is a one-particle wave function.

An auxiliary Hamiltonian with two components is defined: the first term represents the usual kinetic operator, and the second term comprises all the interactions in the system:

$$\hat{H}_{\text{aux}}^{\sigma}(\mathbf{r}) = -\frac{\hbar^2}{2m_e}\nabla^2 + V_{\text{KS}}^{\sigma}(\mathbf{r}) \tag{3.14}$$

The kinetic term in the auxiliary Hamiltonian is

$$T_s = -\frac{\hbar^2}{2m_e} \sum_{\sigma} \sum_{i=1}^{n} \int d^3\mathbf{r} \left|\nabla \Psi_i^{\sigma}(\mathbf{r})\right|^2 \tag{3.15}$$

The Kohn-Sham energy potential is given by:

$$V_{\text{KS}}^{\sigma}(\mathbf{r}) = V_{\text{ext}} + V_{\text{Hartree}} + V_{\text{NN}} + V_{\text{XC}} \tag{3.16}$$

where V_{ext} is the interaction energy of the nuclei with the external field, V_{Hartree} is the self-interacting energy of the electron density, V_{NN} is the interaction between nuclei, and V_{XC} is the exchange-correlation term that includes all many-body effects. The term V_{XC} has no known mathematical formulation, and the predictive accuracy of the calculation depends on the approximation used to define it, as we shall discuss in section 3.1.4.

The ground state energy functional is:

$$E_{\text{KS}} = T_s[n] + E_{\text{Hartree}}[n] + E_{\text{NN}}[n] + E_{\text{XC}}[n] + \int d\mathbf{r} V_{\text{ext}}(\mathbf{r}) n(\mathbf{r})$$

3.1.4 Approximating the exchange-correlation functionals: LDA and GGA

The Local Density Approximation (LDA) functional [Pay+92] and the semi-local GGA functional [PBE96] approximate the exchange-correlation energy arising from the interactions between electrons in a many-electron system.

Local density approximation

The LDA is a local approximation based on the electron density at a given point in space and does not consider the spatial variations in the density.

$$E_{xc}^{LDA}[n(\mathbf{r})] = \int n(\mathbf{r})\varepsilon_{xc}(n(\mathbf{r}))d\mathbf{r} \tag{3.17}$$

LDA proved to work well for many systems, especially for those with a slowly varying spatial electron density, but otherwise, it proved to overestimate the binding energy and, consequently, the bond lengths, which in turn could severely underestimate lattice parameters in the case of crystal structures.

Generalised density approximation

The semi-local GGA functionals [PBE96] are more accurate for many systems and properties than the local LDA [Pay+92]. They are handy for describing the energetics and structural properties of molecules, surfaces, and solids, including transition metals, where electron correlation effects play a significant role. GGA builds upon the LDA by considering the electron density at a given point in space and the spatial gradient (the derivative) of the electron density. This inclusion of gradient information allows GGA to capture more accurately the variations in electron density and electron-electron correlation effects in a system, especially in regions where the electron density changes rapidly, such as near atomic nuclei and chemical bonds.

$$E_{xc}^{GGA}[n(\mathbf{r})] = \int \varepsilon_{xc}(n(\mathbf{r}), \nabla n(\mathbf{r}))d\mathbf{r} \tag{3.18}$$

$E_{xc}^{GGA}[n]$ is the exchange-correlation energy within the GGA, $n(\mathbf{r})$ the electron density at position $\mathbf{r}$, and $\nabla n(\mathbf{r})$ the electron density gradient. However, GGA has its limitations, and it may still fail in strongly correlated electron systems and systems with dispersion interactions (van der Waals forces). To address these limitations, more sophisticated functionals like meta-GGA (meta-generalized gradient approximation) and hybrid functionals have been developed, incorporating additional information about the electron density and its gradients to improve accuracy further.

3.1.5 DFT+U: An extension of density functional theory for modeling strongly correlated materials

Standard Density Functional Theory (DFT) has inherent shortcomings in accurately describing strongly correlated electron systems and transition metal compounds. To address this, DFT can be extended with the Hubbard U term, referred to as DFT+U, which incorporates on-site electron-electron interactions into the DFT Hamiltonian. Adding the Hubbard correction aims to correct for the orbitals self-interaction error [PZ81] and the derivative discontinuity in the exchange-correlation function responsible for underestimating the energy gap[Per+82; PL83].

Selecting the appropriate Hubbard U parameter is crucial for DFT+U calculations; this often necessitates empirical calibration or theoretical estimation specific to the material under study. Additionally, DFT+U calculations can be computationally demanding due to the increased complexity of electron-electron interactions, which is why they are generally reserved for focused investigations of materials with strong correlations.

In our calculations, we utilize a parameter based on our previous work [Sla+23] and earlier research conducted by Luis A. Agapito et al. [Aga+13].

3.1.6 Capability of the DFT

With computer hardware and software advancements, it is now possible to simulate molecules and materials with more significant numbers of atoms. Because of this, order-N algorithms, which allow for linear scaling of computer time and memory with the size of the simulated system, are becoming increasingly important. The order-N algorithms are the core principle of the SIESTA method [Sol+02; YJ20]. Results include the total energy, electronic density, wavefunction, HOMO-LUMO gap, atomic charges, molecular orbitals, optimized geometry, vibrational frequencies, reaction energies, thermodynamic properties, magnetic properties, and dipole/quadrupole moments. The specific output depends on the type of calculation. Researchers use this information to gain insights into molecules, crystals, and materials and predict chemical and physical phenomena.

3.2 Pseudopotentials

The pseudopotential refers to an approximation whereby only the valence electrons play a role in the interaction between atoms, with the core electron states considered chemically inert. The pseudopotential is developed for each atomic

species, replacing the Coulomb potential of each nucleus and the effects of the tightly bound core electrons with an effective ionic potential. The valence electron pseudopotential is crucial for accurately reproducing the behavior and properties of the valence electrons. Using the pseudopotential has several advantages:

- the replacement of the true wavefunction that contains nodes with a smooth function without nodes.
- the reduction in the size of basis sets: the number of basis functions needed for the calculation can be significantly reduced without sacrificing accuracy in treating the valence shell electrons.
- to elude the use of a logarithmically dense grid closer to the center of the atom due to the acute localization of the core electron; instead, a uniform spatial grid is sufficient.

3.3 Basis sets

The electronic wave function of an atom or molecule represents the distribution of electrons in its quantum state. To solve the many-body problem, many implementations expand the lattice periodic part of Kohn-Sham orbitals in terms of a set of basis functions $\phi_n(\mathbf{r})$.

$$\psi_{i\mathbf{k}}^{KS}(\mathbf{r}) = e^{i\mathbf{k}\cdot\mathbf{r}} \sum_n c_{i\mathbf{k}}\, \phi_n(\mathbf{r}) \tag{3.19}$$

The effective potential $V_{\mathrm{KS}}(\mathbf{r})$ retains the symmetries of the lattice crystal. Therefore, the Kohn-Sham states $\psi_{i\mathbf{k}}^{\mathrm{KS}}$, for simplicity's sake, denoted by $\psi_{i\mathbf{k}}(\mathbf{r})$ below, which are one-electron wave functions, can be decomposed into a lattice periodic part $u_{i\mathbf{k}}$ and a phase:

$$\psi_{i\mathbf{k}}(\mathbf{r}) = e^{i\mathbf{k}\cdot\mathbf{r}} u_{i\mathbf{k}}(\mathbf{r}).$$

Hence, plane waves are a natural choice for the basis expansion for periodic solids:

$$\psi_{i\mathbf{k}}(\mathbf{r}) = e^{i\mathbf{k}\cdot\mathbf{r}} \sum_K c_{i\mathbf{k}}(K) e^{i\mathbf{k}\cdot\mathbf{K}}, \tag{3.20}$$

where $\mathbf{K}$ is the reciprocal lattice vector; however, plane waves are less suited to describe molecules. Localized basis sets are an alternative commonly used in quantum chemistry to model molecules.

They are composed of functions centered around discrete points in space, usually at the positions of the nuclei. These basis functions are often expressed as the product of a spherical harmonic $Y_{l,m}$ and a radial part $\varphi_{n,l}$, and the Kohn-Sham states is expressed as:

$$\psi_{i,\mathbf{k}}(\mathbf{r}) = e^{i\mathbf{k}\cdot\mathbf{r}} \sum_{\mathbf{R}\alpha} \sum_{n,l,m} c_{i\mathbf{k}}^{\alpha,n,l,m} \Phi_{\alpha,n,l,m}(\mathbf{r}-\mathbf{R}) \tag{3.21}$$

$$= e^{i\mathbf{k}\cdot\mathbf{r}} \sum_{\mathbf{R}\alpha} \sum_{n,l,m} c_{i\mathbf{k}}^{\alpha,n,l,m} \phi_{n,l}(|\mathbf{r}-\mathbf{R}_\alpha| - \mathbf{R}) Y_{l,m}(\theta,\phi), \tag{3.22}$$

where α runs over all atoms in the unit cell and R over all lattice vectors. The most common localized basis sets include Slater-type orbitals [Sla30] ($\phi_{n,l} \sim r^l e^{-\alpha r}$), Gaussian-type orbitals [Boy50] ($\phi_{n,l}(r) \sim r^l e^{-\alpha r^2}$), and numerical atomic orbitals [AE73]. Numerical atomic orbitals are defined as numerical solutions to the Schrödinger equation for electrons in the (pseudo)potential of the isolated atom. It is usually expanded as a linear combination of basis sets. This approximation allows for the tractable description of the electronic wave function.

Depending on the accuracy required for the calculation, available computational resources, and research objectives, one can choose among different types of basis sets. Examples include minimal, double-ζ, double-ζ plus polarization, triple-ζ, triple-ζ plus polarization, diffuse, correlation-consistent, segmented, and custom basis sets [Art+99]. Researchers often perform basis set benchmarking to determine the appropriate level of accuracy for their research questions.

3.4 The SIESTA method

Until now, several approximations have been made to consider solving the Schrödinger equation numerically. This includes the Born Oppenheimer approximation, the treatment of exchange and correlation (XC) within Kohn–Sham DFT[KS65b], and pseudopotentials. To solve the Schrödinger equation, One must choose the proper way to describe the electronic wave function adequately. While achieving the order O(N) iterations using plane waves is difficult, the linear combination of atomic orbitals (LCAO) is the most fitting option see section 3.3 as implemented in the SIESTA package.

At first, in SIESTA, one finds the extent of the radial component of the wave function by solving the Schrödinger equation for an isolated atom restricted to a finite sphere r_c, whose value can differ for each orbital. A single-ζ basis is

constructed by solving the Kohn-Sham eigenvalue problem for the isolated atom with an additional confinement potential V_{conf} , which is flat in the sphere's center and diverges at r_c^l [SN89].

$$\left(-\frac{1}{2r}\frac{d^2}{dr^2}r + \frac{l(l+1)}{2r^2} + V_l^{PP}(r) + V_{\text{conf}}\right)\phi_l^{1\zeta}(r) = (\epsilon_l + \delta\epsilon_l)\phi_l^{1\zeta}(r) \tag{3.23}$$

$$\phi_l^{1\zeta}(r_c^l) = 0 \tag{3.24}$$

Where V^{PP} is the pseudopotential. Including a soft-confinement potential as defined in equation (3.25) [Jun+01] ensures continuous derivatives and reduces problems in calculating forces and stresses.

$$V_{\text{conf}}(r) = V_0 \frac{e^{-\frac{r_c - r_i}{r - r_i}}}{r_c - r} \tag{3.25}$$

Where V_0 is a parameter, r_c is the confinement radius where the potential asymptotically tends to infinity, and r_i is the starting point for the potential.

Within the SIESTA package, one can use one or multiple radial functions for each angular momentum l. Once the single-ζ basis has been derived to define the multiple-ζ, one has to keep the same extent r_c and the same tail within some range ($r^s \leq \mathrm{r} \leq \mathrm{r_c}$). Below r^s, the split radius, a polynomial function is used. It corresponds to the default method in SIESTA, called the split-valence method. For each orbital $\phi^{1\zeta}(r)$, a modified orbital

$$\phi_l^{2\zeta}(r) = \begin{cases} r^l(a_l - b_l r^2) & \text{if } r < r_l^s \\ \phi_l^{1\zeta}(r) & \text{if } r \geq r_l^s \end{cases} \tag{3.26}$$

is defined. r_l^s is optimized so that the norm of $\int_0^{r_l^s} r^l \phi^{1\zeta}(r)\, dr$ corresponds to a specific value (typically 0.15), and a_l and b_l are chosen so that $\phi_l^{2\zeta}$ and its first derivative are continuous. The new basis orbital is then given by

$$\phi^{2\eta}(r) = \phi_l^{1\zeta}(r) - \phi_l^{2\zeta}(r).$$

This procedure can be repeated with smaller split norms to create a multiple-ζ basis set.

When the bonds are formed, the atomic orbitals are distorted. In that sense, constructing the basis set required using polarization orbitals. One can achieve that in SIESTA by two means: By including the polarization flag in the basis

description, SIESTA automatically generates an l+1 basis function for the polarized orbital; alternatively, one could manually parametrize and optimize the polarization function included.

The SIESTA method is distinguished from other DFT approaches by choosing the atomic orbitals as basis sets to expand the electronic wave function. This often means that the number of basis functions required is smaller than other methods [Ang+02; Art+99; Jun+01]. In addition, strict localization of the orbitals leads to sparse matrices, and sparse methods can be exploited for efficiency.

3.5 Analysis Tools

3.5.1 Structural analysis techniques: radial distribution function, and angle distribution function

The radial distribution function

The Radial Distribution Function (RDF) measures the probability of finding an atom at a distance r from another atom with respect to the probability one would have in an ideal gas when particles are entirely uncorrelated. From the practical point of view, we count the number of atoms that have a neighbor between r and $r + dr$ and normalize this number by the density of the system times the volume of the spherical shell defined by r and $r + dr$. Moreover, we average on all the atoms of the system. For dr going to zero, the formula is:

$$g(r) = \frac{1}{4\pi r^2 N\rho} \sum_i \sum_{j \neq i} \delta(r - r_{ij}) \tag{3.27}$$

where

$$\rho = \frac{N}{V}$$

the density of the system and r_{ij} the distance between atom i and j.

A partial RDF can be defined by looking at the probability of finding an atom of specie η in the proximity of an atom of specie ν:

$$g_{\mu\eta}(r) = \frac{1}{4\pi r^2 N_\eta \rho_\mu} \sum_{i \in \eta} \sum_{j \in \mu \neq i} \delta(r - r_{ij}) \tag{3.28}$$

with N_η number of atoms of η specie and ρ_μ density of μ specie. Then:

$$g(r) = \sum_{\eta\mu} \frac{N_\eta N_\mu}{N} g_{\eta\mu}(r) \tag{3.29}$$

The Angle Distribution Function

The Angle Distribution Function (ADF) is a statistical tool used to analyze molecular systems and quantify the distribution of angles formed between bonds or molecular orientations. It provides insights into the frequency of certain angles occurring within a given configuration of particles or atoms in a simulation. The first step in computing the ADF involves defining bonds based on the total and partial radial distribution functions (RDFs). Subsequently, we create a histogram or probability distribution to analyze the angle distribution.

The order parameter for the tetrahedral structural motif

Quantifying structural order in glasses has proven more difficult than in crystals because no atoms are structurally equivalent. Herein, we defined an order parameter for the tetrahedral structural motif [ED01].

$$q = 1 - \frac{3}{8} \sum_{k>i} (\frac{1}{3} + cos\theta_{ijk})^2 \tag{3.30}$$

Where j is the central atom and $cos\theta_{ijk}$ is the angle formed by two neighboring atoms of j, i, and k. For a perfect tetrahedra network, q=1. For the Octahedral structure motif, q=0.

3.5.2 Electronic properties

Density Of States (DOS)

The density of states is a fundamental quantity in condensed matter physics and quantum mechanics. It describes the distribution of energy levels available in a material or physical system. It is fundamental for understanding materials' electronic and vibrational properties, including electrical and thermal conductivity. The DOS shows how densely packed or sparse the energy levels are at different energy values. A high DOS at a specific energy means many states are available for particles at that energy, while a low DOS means fewer states are available.

Let g(E) be the density of the state.

$$g(E) = \sum_{i}^{bands} \delta(E - E_i) \tag{3.31}$$

$\delta(E - E_i)$ represents a Dirac delta function, which is zero for all values of E except $E = E_i$. The energy E_i is the energy of the i-th band.

The Projected Density Of States (PDOS)

The Projected Density of States $g_\mu(E)dE$ is the number of one-electron levels with weight on orbital μ between E and E+dE

$$g_\mu(E) = \sum_{i}^{bands} \sum_{\nu} c^*_{\mu i} c_{\mu i} S_{\mu\nu} \delta(E - E_i) \tag{3.32}$$

where $c_{\mu i}$ are the coefficients of the eigenvector ψ_i with eigenvalue E_i, and $S_{\mu\nu}$ is the overlap matrix of the atomic orbitals basis.

The relation between the DOS and the PDOS:

$$g(E) = \sum_{\mu} g_\mu(E) \tag{3.33}$$

The inverse participation ratio

To characterize the spatial extent of each electronic state, we employ the Mulliken charge $q_i(E)$ residing at an atomic site i for an eigenstate with energy E. The inverse participation ratio (IPR), is defined by the following expression:

$$I(E) = \sum_{i=1}^{N_{\text{at}}} (q_i(E))^2. \tag{3.34}$$

It is a measure of the degree of localization of each state.

For an ideally localized state, only one atomic site contributes all the charge, so $I(E) = 1$. For a perfectly delocalized state, with equal weight on all the atoms in the system, $I(E) = 1/N_{at}$. High $I(E)$ values, therefore, correspond to localized states, while low values indicate stronger delocalization.

3.6 Convergence with respect to computational parameters

The importance of selecting suitable computational parameters and accurately representing electronic wave functions within a finite basis set cannot be overstated to ensure accurate and reliable calculations. In this section, we study the convergence of the energy and forces with respect to the k-point, real space grid, and the exchange-correlation function.

Convergence of the Energy with the number of k-points

Starting with the GeSe crystal structure, we run a SIESTA single point calculation using the diagonalization method for solving the Kohn-Sham equations. The calculation is carried out subject to two constraints: the position of the atoms in the unit cell is fixed and the lattice vectors are fixed.

Instead of using the MonkhorstPack method [MP76] to sample the k-points in reciprocal space for the Brillouin zone integration, we use the kgrid.Cutoff flag. This parameter controls the fineness of the k-grid used for Brillouin zone sampling. It allows for the definition of the k-point sampling using a single parameter. The kgrid cutoff flag gives the values for the sampling in each direction, which consider the cell's length in that direction so that fewer k-points are needed in the longer axes. It defines the k-points in the simulation cell that would correspond to a single k-point of a supercell with the lattice vectors with lengths defined by the kgrid cutoff parameter (which has the unit of length) [Sol+02].

Table 3.1 shows the GeSe crystal's total energy at different k-grid cutoff values. ΔE(eV) represents the energy difference between two consecutive values of the k-grid cutoff. We choose the value for which the energy difference ΔE(eV) is less than 0.01 eV, which is k-grid Cutoff = 14 Å.

Convergence of the calculation with respect to the Mesh Cutoff: The eggbox effect

SIESTA's *Mesh Cutoff* defines the finite 3D real-space grid for some integrals calculation and the representation of charge densities and potentials. It defines the plane-wave cut-off for the grid, determining its fineness. This means all the periodic plane waves with kinetic energy lower than the mesh cutoff can be represented on the grid without artifacts. A higher mesh cutoff corresponds to a finer grid and, thus, more accurate real-space integration and increased computational cost. However, when the energy cutoff is set too low in SIESTA, it can result in the

kgrid.Cutoff (Å)	Energy(eV)	ΔE(eV)
2	-1800.683176	
4	-1804.177351	-3.49418
6	-1804.632679	-0.455328
8	-1804.608987	0.023692
10	-1804.615019	-0.006032
12	-1804.593561	0.021458
14	-1804.591008	0.002553
16	-1804.592412	-0.001404
18	-1804.594940	-0.002528
20	-1804.595094	-0.000154

Table 3.1: Energetic data for the GeSe crystal at different values of the kgrid Cutoff. ΔE(eV) represents the energy difference between two consecutive values of the k-grid cutoff.

eggbox effect. The eggbox effect arises due to the charge density and the potential having plane wave components beyond the mesh cutoff, which introduces spurious periodic oscillations in properties like charge density and energy. This can lead to a loss of accuracy in calculating electronic properties, particularly in periodic systems like crystals or surfaces. Technically, the eggbox arises from numerical artifacts due to the misalignment between the grid and atomic positions when the grid resolution (set by the Mesh Cutoff) is too coarse. To mitigate the eggbox effect in SIESTA, choosing an appropriate energy cutoff value is essential. This depends on the material being studied, the desired level of accuracy, and the available computational resources.

We conduct convergence tests by gradually increasing the energy cutoff to ensure that the eggbox effect does not compromise the electronic structure calculations. This enables us to strike a balance between computational efficiency and the accuracy of the results. Let E_{cut} be the maximum kinetic energy of the plane waves that can be represented in the grid without aliasing.

$$E_{cut} = \frac{1}{2}\left(\frac{\pi}{\Delta x}\right)^2 \tag{3.35}$$

where Δx is the grid interval. We monitor the relative position of atoms by the input variable: *%blockAtomicCoordinatesOrigin* to specify the origin of the atomic coordinates in the input file. We find all the atomic orbitals that do not vanish at a given grid point to compute the density. Once the density is known, we compute the

charge density and the potentials. For each value of the Mesh CutOff, for example, 100 Ry, the grid of (InitMesh: MESH =) 24 x 30 x 72 = 51840 along the three lattice vectors is read in the output file. We compute the change in the energy and the forces when we displace rigidly all the atoms in the unit cell from one point of the grid to the next one (let us assume, in this case, in 10 steps)

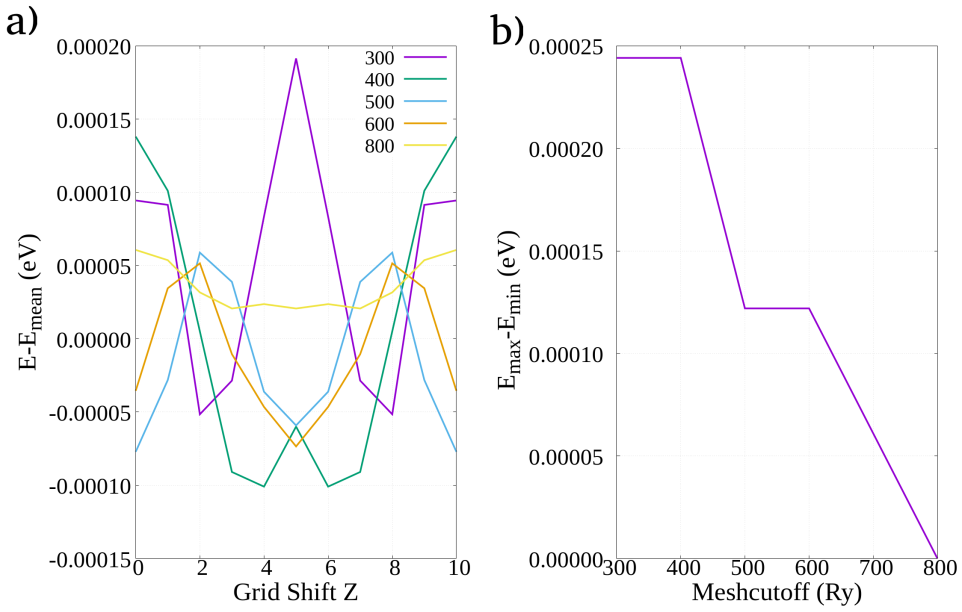

Figure 3.1: Convergence of the calculation with respect to the MeshCutoff. Panel a) shows the eggbox effect, and panel b) shows the variation in energy (the difference between maximum and minimum energy) changes with different values of the Mesh cutoff.

Figure 3.1 represents the convergence of the energy with respect to the Mesh cutoff. Higher mesh cutoff values (e.g., 800 Ry) generally show less pronounced and smother fluctuations compared to lower values (e.g., 300 Ry). This behavior could indicate that a finer grid leads to more sensitivity in energy calculations with respect to grid shifts. We choose the value for which the energy difference is less than 0.01 eV; here, mesh cutoff =350 Ry.

3.6.1 Effect of orbital-confining cutoff radii and the basis set size on the structure and the total energy of the crystal GeSe

Using the k-points and the mesh cutoff found in previous sections, we aim to find the cutoff radii and the basis set sizes that give the best (lowest) energy. For each basis set considered, we optimize the crystalline structure (lattice vectors and atomic positions) using the conjugate gradient minimization algorithm in SIESTA. The optimization of the unit cell vectors is carried out subject to one constraint: the shear stresses are nullified to keep the cell angles fixed to 90°, characteristic of the crystal GeSe structure. The tolerance for the maximum force is set to 0.01 $\frac{eV}{\text{Å}}$.

Herein, we will first analyze the effect of the orbital-confining cutoff radii and then analyze the effect of basis set sizes on the structure and total energy of crystalline GeSe. [2].

Effect of the orbital-confining cutoff radii and basis set sizes on the structure and the total energy of the crystal GeSe

In the SIESTA code[Sol+02; YJ20], the excitation energy of the pseudo-atomic orbital (PAO) due to the confinement to a finite range is defined by the flag PAO.EnergyShift. For four values of the confinement radius, PAO.EnergyShift 0.01, 0.005, 0.001, and 0.0005 Ry, we optimize the structure of the crystal GeSe.

Table 3.2 shows the cell vector modules (in Å) and the total energies (in eV) of the crystal GeSe computed using two exchange-correlation functionals—GGA [PBE96] and VDW [Dio+04; RS09]—at various PAO energy shift values with a DZP basis set. For both functionals, the cell vector modules change, reflecting an adjustment in the structure of GeSe as the confinement of the pseudo-atomic orbitals changes. The energy decreases as the PAO energy shift decreases, indicating that less tightly confined orbitals lead to a more stable (lower energy) configuration. For all the PAO energy shifts, the semi-local GGA functional, which does not account for the non-local electron-electron interaction, shows smaller values of the lattice parameters in comparison to the VDW functional [TS09]

From 3.2, the PAO energy shift yielding the lowest total energy is 0.0005 Ry. However, this basis set is more computationally expensive due to longer orbitals. The 0.001 Ry basis set provides nearly identical structural and energetic results, so

2 While this section focuses on the Ge and Se basis set, the same analysis has been applied to each dopant. For brevity, we discuss only the Ge and Se basis set here.

3 In the cell vector modulus column, the first number corresponds to a, the second to b, and the third to c.

PAO Energy Shift (Ry)	XC Functional: GGA (PBE)		XC Functional: VDW (DRSLL)	
	Cell Vector Modules [3](Å)	Energy (eV)	Cell Vector Modules (Å)	Energy (eV)
0.01	3.846691 4.454381 10.924657	-1805.664451	3.859875 4.743117 11.580029	-1823.248988
0.005	3.844274 4.532334 11.065210	-1806.083828	3.871606 4.823299 11.724771	-1823.729704
0.001	3.846256 4.595637 11.079478	-1806.406595	3.870043 4.896345 11.830289	-1824.093938
0.0005	3.842017 4.600073 11.087940	-1806.461628	3.867308 4.897513 11.858031	-1824.151191

Table 3.2: Summary of PAO energy shift, cell vector modules, and total energies of the crystal GeSe for the GGA and VDW exchange-correlation functionals

lattice parameters	a (Å)	b (Å)	c (Å)
experiment [Sis+17]	3.83	4.39	10.83
GGA(PBE) [Hao+16]	3.88	4.52	11.17

Table 3.3: Literature references for the lattice parameters of the crystal GeSe.

we selected 0.001 Ry among the four PAO energy shifts, making it a good balance between accuracy and computational cost. Using that value, we obtain lattice parameters that are close to previous theoretical and experimental results (see table 3.3).

We now aim to analyze the effect of the basis set sizes on the GeSe structure and total energy for GGA and VDW exchange-correlation functionals.

Basis Set	XC.functional GGA(PBE)		XC.functional VDW(DRSLL)	
	Cell vector modules (Å)	Energy(eV)	Cell vector modules (Å)	Energy(eV)
SZ	4.032062 4.670248 11.454659	-1803.169510	4.096195 4.857251 12.006126	-1821.169435
SZP	3.944543 4.411208 11.199177	-1805.669476	3.980597 4.724612 11.788111	-1823.161862
DZ	3.957785 4.424865 10.962240	-1804.565464	3.998947 4.820632 11.608903	-1822.303889
DZP	3.844665 4.591954 11.063214	-1806.410241	3.866257 4.909486 11.803224	-1824.094737
TZ	3.944108 4.439915 10.954717	-1804.813399	3.970715 4.891818 11.804344	-1822.578579
TZP	3.840987 4.584748 11.075124	-1806.537884	3.861115 4.913848 11.860414	-1824.240501
TZDP	3.834064 4.563280 11.050677	-1806.820379	3.852030 4.896607 11.798794	-1824.475278
TZTP	3.836954 4.532393 10.960623	-1806.916253	3.847681 4.893051 11.772972	-1824.544012

Table 3.4: Cell parameters and total energy of the GeSe crystal structure for different basis set sizes and exchange-correlation functionals with a PAO energy shift = 0.001Ry.

Table 3.4 shows the lattice parameters and the total energy of the GeSe crystal for different basis set sizes considering GGA and VDW with a PAO energy shift of 0.001Ry. The cell vector modules show variations as the basis set changes: the cell dimensions are smaller at larger basis set sizes. Generally, the VDW functional shows a bigger cell dimension for the same basis set size than the GGA functional. Regarding the total energy, the GeSe crystal energy decreases more by adding polarized orbitals than by increasing the number of ζs on the occupied valence shells. The TZTP basis set yields the lowest total energy, since it is the most complete basis set of all considered. However, it is considerably more computationally expensive than the others. A good compromise between accuracy and computational cost is the DZP basis set, which produces a very similar structure and comparable energy (just 0.5 eV/unit cell higher than the TZTP basis).

The effect of the f shell on the structural and energetic properties of the GeSe crystal structure

As mentioned above, including more orbitals when defining basis sets improves the description of electronic states and orbital polarization. In previous sections, we used various PAOs to assess their effects on the energetic and structural properties of crystalline GeSe. Here, we evaluate the effect of adding the f shell on these properties.

f orbitals	XC Functional: GGA (PBE)		XC Functional: VDW (DRSLL)	
	Cell Vector Modules (Å)	Energy (eV)	Cell Vector Modules (Å)	Energy (eV)
No f	3.835790 4.515615 10.690529	-1806.688395	3.859922 4.896790 11.742750	-1824.236896
f orbital only on Ge	3.833193 4.463662 10.536487	-1806.961293	3.847597 4.924585 11.721244	-1824.439878
f orbital only on Se	3.861842 4.344108 10.693335	-1806.940039	3.848407 4.906291 11.662428	-1824.418959
f orbital on Ge and Se	3.869149 4.257673 10.584092	-1807.214559	3.848132 4.923343 11.677112	-1824.579122

Table 3.5: Comparison of cell vector modules and total energy in GGA and VDW approximations with f orbitals.

Table 3.5 shows the structural and energetic properties of GeSe crystals using GGA (PBE) and VDW (DRSLL) exchange-correlation functionals. First and foremost, the difference in value between the configuration without the f orbital in table 3.5 and the DZP basis set in table 3.4 is that table 3.5 includes perturbative d orbitals, while table 3.4 presents the energetic and structural data of the crystal GeSe using explicit PAOs as basis sets.
Across different f orbital configurations, the cell parameters for both functionals show slight variations, with VDW yielding larger cell parameters than GGA. The configuration with f orbitals on both Ge and Se has the lowest total energy for both functionals. The energy differences between configurations where the f orbital is added only on Ge or Se are minor, 0.021 eV for GGA and 0.0209 eV VDW.

For configurations without f orbitals, the energy differences relative to configurations with f orbitals on Ge(Se) is 0.273 (0.252) eV for GGA and 0.203(0.182) eV for VDW. When adding f orbitals to both Ge and Se, the energy difference is 0.526 eV for GGA and 0.342 eV for VDW. The configuration with the f orbitals on both the Ge and Se yields the lowest total energy since it is the most complete basis set of all considered. However, it is considerably more computationally expensive than the others. A good compromise between accuracy and computational cost is the configuration with no f orbital considered on either Ge or Se, which produces a similar structure and comparable energy (just 0.526 eV/unit cell higher than the basis set with f on both the Ge and Se).

3.7 Computational details

This section summarizes the computational details used to study the crystal GeSe and to generate the a-Ge_xSe_{1-x}.

We carry out first-principle DFT calculations using numerical atomic orbitals appropriate for large systems as implemented in the SIESTA package. Specifically, we used a split-valence double-ζ basis set, including polarization functions [Art+99] to expand the electronic wave function. The Pseudopotential Markup Language (PSML) obtained from the pseudo-dojo data set [Set+18] represents the valence and the ionic core interaction. Only the valence electrons were considered in the calculations, with the core being replaced by norm-conserving scalar relativistic pseudopotentials [TM91] factorized in the Kleinman-Bylander form [KB82] and to account for the electron-electron interaction, we used the GGA exchange-correlation functional as parametrized by Perdew, Burke, and Ernzerhof [PBE96]. The energy cutoff of the real space integration mesh was 350 Ry. To compute the charge density, the Brillouin zone was sampled with the method of Moreno and

Soler [MS92] with the kgrid cutoff of 14 Å for the crystal and at the gamma point for the amorphous structure (kgrid cutoff = 0 Å). Atomic positions were relaxed with a force tolerance below 0.01 eV/Å in the crystal GeSe and 0.04 eV/Å in a-Ge_xSe_{1-x}. Below, we show a SIESTA input of parameters used for the a-Ge_xSe_{1-x}.

```
SystemName                  a-GeSe
SystemLabel                 a-GeSe
NumberOfAtoms               336
NumberOfSpecies             2

%block ChemicalSpeciesLabel
  1    32   Ge
  2    34   Se
%endblock ChemicalSpeciesLabel

PAO.EnergyShift             0.001 Ry
PAO.BasisType               split
PAO.SplitNorm               0.150000
PAO.BasisSize               DZP
SolutionMethod              diagon


XC.functional               GGA
XC.Authors                  PBE

SpinPolarized               false
MeshCutoff                  350.000000 Ry
kgrid\_cutoff               0.000000 Bohr
ElectronicTemperature       300.000000 K
MaxSCFIterations            300
DM.NumberPulay              6
DM.MixingWeight             0.150000

MD.VariableCell             false
MD.MaxStressTol             1.000000 GPa
MD.MaxForceTol              0.040000 eV/Ang
```

3.7.1 Amorphous structure generation and simulation protocol

Herein, we present the protocol and method to generate our amorphous a-Ge_xSe_{1-x} models. Using the melt-and-quench method, we generated structures for three stoichiometries: one for the stoichiometric compound a-GeSe and two for slightly non-stochiometric ones, with x=0.4 and x=0.6, respectively. The a-Ge_xSe_{1-x} systems have been built starting from a 4(Ge):2(Se) coordinated initial structure obtained from a Markov Chain Monte Carlo method. We considered a potential energy with two components:

- a repulsive Coulomb interaction between atoms, which ensures a more homogeneous distribution within the cell, We randomly move one atom and evaluate the energy difference between the two configurations using a Gauss distribution. If the energy difference is below our threshold-defined value, the move is accepted; if not, it is rejected.
- and a potential dependent on the Ge and Se coordination to enforce coordination of 4 and 2 for Ge and Se, respectively see equations 3.36.

$$dE = \left| \sum_{i=1}^{N_{\text{at\_Ge}}} (n_{\text{Ge}} - 4) \right| + \left| \sum_{i=1}^{N_{\text{at\_Se}}} (n_{\text{Se}} - 2) \right| \tag{3.36}$$

  n_{Ge} is the coordination of Ge atoms, and n_{Se} is the coordination of Se atoms. $N_{\text{at\_Ge}}$ and $N_{\text{at\_Se}}$ are the total number of atoms of Ge and Se in the supercell, respectively.

This two terms potential energy is used to construct different cubic supercells of 336 atoms and a box size of $21 \times 21 \times 21$ Å^3, corresponding to a density of 4.57 g/cm^3 for a-$Ge_{0.5}Se_{0.5}$, 4.53 g/cm^3 for a-$Ge_{0.6}Se_{0.4}$, and 4.58 g/cm^3 for a-$Ge_{0.4}Se_{0.6}$. The resulting geometry was then relaxed before the melting-and-quenching procedure using a conjugate gradient algorithm [YJ20]. AIMD are then carried out within the isobaric-isothermal (NPT) ensemble at zero external pressure with an annealing algorithm by rescaling the velocities and the pressure at each time step of Δt = 1 fs and the characteristic relaxation time τ_{relax} = 1 ps. The simulations started by equilibrating each initial configuration at 1200 K for 12 ps, at which the system melts and loses the memory of the initial configuration. After equilibration, each system was quenched to 800 K throughout 3 ps; this corresponds to an average cooling rate of 133 $\frac{K}{ps}$. The configurations obtained at 800 K were quenched again to 400 K in 3 ps using a τ_{relax} = 750 fs.

For the doped a-Ge_xSe_{1-x}, $x = 0.4, 0.5, 0.6$, the initial structures are generated using the initial undoped 336-atom supercells. The percentage of Ge and Se atoms is randomly replaced with 1%, 3%, 5%, 7%, 10 % and 15% of the dopant concentration, ensuring that the dopants are homogeneously distributed throughout the structure. Afterward, the structures are melted and quenched following the same protocol as the undoped case.

4 Non-doped a-GeSe

Neuromorphic computing is envisaged as one of the most promising solutions for the power and memory limitations plaguing the development of standard CMOS (Complementary Metal-Oxide-Semiconductor) electronics architectures. The idea is to process information as the brain does, with memory and computing being co-located within the same biological system [KYW13; Mer+14]. Among the novel technologies that are being explored for neuromorphic computing, a class of switching memories, such as the phase-change memories (PCMs) [Bur+10] or resistive random-access memories (RRAM) [WY19], generate high expectations within the semiconductor industry. Developing these new electronics relies on designing and characterizing materials and devices. Albeit implicitly interconnected, the interplay between the parameters that characterize the materials (e.g., structure, composition, doping, stability, electrical and thermal response) and the function and performance of the device (e.g., data retention, power consumption, interconnection, switching time) is hard to determine.

Here, we focus on the structural and electronic properties of amorphous GeSe (a-Ge_xSe_{1-x}) compounds, which have been proposed as promising building block compounds for ovonic switching materials for non-volatile memory devices and selectors [Che+18; Kon+21]. While much effort has been devoted to GeTe as a prototypical phase change material, more knowledge is needed for the quasi-stoichiometric GeSe compound. Nonetheless, this material has been recently exploited to realize selectors units [Cha+21]. The first results indicate that GeSe exhibits ovonic electrical switching in the amorphous phase [Liu+19b] and that even moderate modulation of the stoichiometry ratio affects the electrical response of the device in terms of I-V characteristics and power dissipation. However, the origin of this phenomenon is yet to be understood. On the theoretical side, unraveling the interplay between the local order of structures, trap states, and the resulting electrical response is a significant challenge that requires the ability to treat large systems at the atomistic level along with their electronic structure. Given the amorphous material's intrinsically disordered nature, we need large-scale first-principles simulations, which implies building large atomistic models that can represent the material with sufficient fidelity. The influence of disorder causes essential differences in the electronic density of states of amorphous semiconductors. Actual materials contain structural defects that can dominate their physical and chemical

behavior. A description of the electronic properties will lead to understanding the structural origin of defects, the nature of the mobility gap states, and the conducting behavior of the different electronic states [KS15].

Understanding the local-order structure as a function of the composition in the a-Ge_xSe_{1-x} compounds is of fundamental relevance in designing materials for more efficient selectors. Local structural order in chalcogenides is expected to be closely related to their electronic properties, such as the electronic band gap, mobility of the electronic states, and the existence of the trap states [IR60]. However, a common consensus on the interplay between the electronic structure and the structural properties of amorphous chalcogenides is still to be developed. Raty et al. [Rat+01] showed that Ge-Ge homopolar bonds of a germanium-centered tetrahedron cause midgap states. In contrast, Zipoli et al. [ZKC16] suggested that the clustering of undercoordinated or overcoordinated Ge atoms is associated with midgap states (according to the 8-N rule [Mot67], the Ge atom, with its four valence electrons, would adopt a coordination number of 4). Moreover, Konstantinou et al. [Kon+19] found that a pentacoordinated Ge in the crystalline-like environment constitutes the local defective bonding environment, while Li et al. [LR20] identified that the Ge-Ge bond in a crystalline-like environment exhibits a negative U.

Using ab initio molecular dynamics (AIMD) to study amorphous $GeSe_{2-x}$, Li [LR19] found that the conduction band consists of Ge-Se σ^* states with a low effective mass and a broad tail of localized Ge-Ge σ^* states below this band edge. Certain Ge-Ge bonding configurations create conduction band tail states, leading to non-linear conduction. Guo et al. [Guo+19] studied the Se-rich a-$Ge_{0.4}Se_{0.6}$ sample and found that, structurally, the sample is chemically ordered, with predominantly fourfold-coordinated Ge sites and twofold-coordinated Se sites—the ground state mobility gap of approximatively 0.8 eV is found, with the Fermi level pin in the midgap.

Over several decades, there has been controversy over the coordination of the Te- and the Se-based chalcogenides. Experimental results based on X-ray photoelectron spectroscopy (XPS) and ultraviolet photoelectron spectroscopy (UPS) of a-GeTe [TSS82] suggest the presence of a chemically ordered structure. It has been shown that a thin film of a-GeTe deposited onto a cooled substrate has a 3:3-fold coordination (i.e., 3-fold coordinated Ge and 3-fold coordinated Te), but it relaxes onto a 4:2-fold coordination after thermal annealing (i.e., 4-fold coordinated Ge and 2-fold coordinated Te)[TSS82]. Other studies have also suggested a possible 4:2 folding of a-Ge_xSe_{1-x}. O'Reilly et al. [ORK81] stated that a-Ge_xSe_{1-x} may be a 3:3 coordinated structure. At the same time, Trodahl et al. [Tro82] used far-infrared absorption to show that the 4:2-fold coordinated model is more appropriate for this system, although the 3:3-fold is also possible. Trodahl [Tro84] also showed how

heteropolar bonds are favored over homopolar bonds. It is worth noting that these experimental studies do not have enough sensitivity to a small density of defects because the signal is averaged over the whole material.

This chapter aims to bridge the gap in the literature regarding realistic DFT-based structural models of amorphous a-Ge_xSe_{1-x} by examining both the structure and electronic properties and, more importantly, it seeks to unveil the interplay between the localized states and structural motifs in the amorphous network. The novelty of this work resides in developing realistic density functional theory-based structural models on a-Ge_xSe_{1-x} using the melt and quench protocol. For conciseness, only one model for each stoichiometry will be shown, even though we have generated and studied several.

To better understand the structural and electronic properties of a-Ge_xSe_{1-x} and explain the interplay between the electronic and structural features, we developed realistic DFT theory-based models of the compound. Then, we systematically studied each localized state, evaluated the weight of a particular electronic state on each atom, and linked it to a structural motif.

4.1 Structural features

The main short-range interaction within the covalently bonded network of amorphous materials are usually similar to those in their crystalline analogs [Hol+13]. The case of the germinate glasses (Ge_xCh_{1-x}, where Ch=Se, Te, S) may be an exception, although there is controversy in the literature, and different chalcogenides may behave differently.

Therefore, understanding the structural configuration of crystalline GeSe (c-GeSe) is a necessary preliminary step. We then describe in detail the structural and bonding characteristics of the amorphous models we have generated.

Lattice parameters [Å]	Atomic Angle [°]
a = 3.8447	α = 92.8006
b = 4.5919	β = 104.2916
c = 11.0631	

Table 4.1: Structural parameters of the GeSe crystalline phase and atomic angle obtained in our calculation. The experimental values are a = 3.8338 Å, b = 4.3900 Å and c = 10.8300 Å[Sis+17].

Figure 4.2 shows the partial radial distribution function (RDF) of a-Ge_xSe_{1-x} for all three stoichiometries considered here. The top panel shows the Ge-Se partial

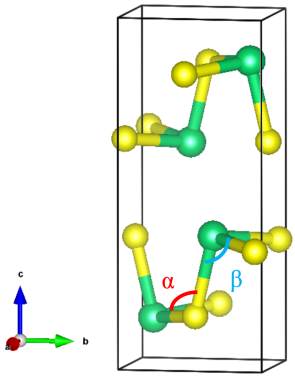

Figure 4.1: Crystal structure of GeSe (Pnma) and bond angle. Green: Ge and yellow: Se.

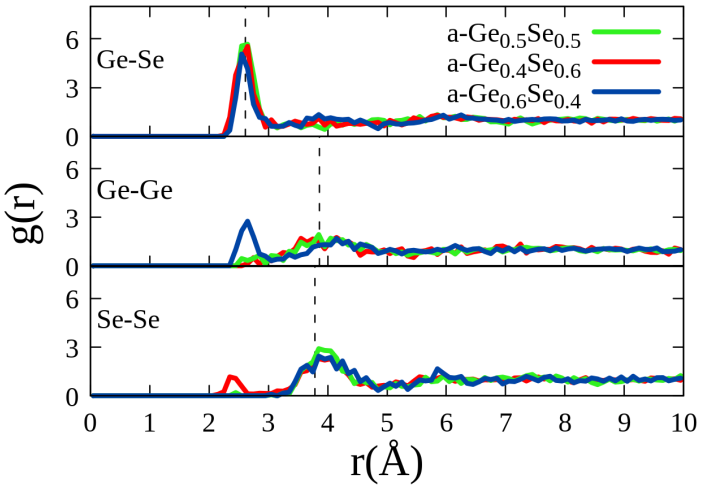

Figure 4.2: Radial distribution functions g(r) of the a-$Ge_{0.5}Se_{0.5}$, a-$Ge_{0.4}Se_{0.6}$, and the a-$Ge_{0.6}Se_{0.4}$. The top panel is the Ge-Se partial pair correlation function, the middle panel is the Ge-Ge partial pair correlation function, and the bottom panel is the Se-Se partial pair correlation function. The dashed line in each panel represents the corresponding distance in the crystalline structure.

pair correlation function, the middle panel shows the Ge-Ge partial pair correlation function, and the bottom panel shows the Se-Se partial pair correlation function. The Ge-Se RDF of the stoichiometric compound a-$Ge_{0.5}Se_{0.5}$ shows a well-defined first neighbor shell with a bonding distance narrowly distributed around 2.65 Å. Increasing the Ge or Se content shows a seemingly unaltered distribution of Se

around Ge. This is evident from the RDF of the Ge-rich and Se-rich samples, where the Ge-Se first neighbor shell's width and the height of all three functions are quite similar. The Ge-Se bonds are the first neighbor shell in a-Ge_xSe_{1-x} at all stoichiometries. For the Ge-Ge RDF of a-$Ge_{0.5}Se_{0.5}$ (middle panel), we observe that the Ge-Ge distance is primarily of the order of the second neighbor shell, with only a few Ge-Ge bonds. Upon increasing the concentration of Ge to 60%, the first-neighbour Ge-Ge shell becomes more prominent, with a Ge-Ge peak at a distance of less than 3 Å. A similar tendency is seen for the Se-Se RDF in the Se-rich sample. Increasing the concentration of an atomic species beyond that of the stoichiometric compound gives rise to the formation of the corresponding homonuclear bonds. The Ge-Ge second neighbor peak is broader across all three stoichiometries compared to the Se-Se second neighbor peak, suggesting that the $\angle$(Ge−Se−Ge) angular distribution function (ADF) is broader than the $\angle$(Se−Ge−Se) ADF, in order to maintain the homogeneity of Se distribution relative to Ge within the first neighbor shell. For the Se-Se RDF (bottom panel), we count only two Se-Se bonds in the a-$Ge_{0.5}Se_{0.5}$ sample, while no Se-Se bonds are observed in the Ge-rich sample. The resulting Ge-Se RDF and Se-Se RDF of the amorphous structures have a prominent peak at about 2.65 Å for a-$Ge_{0.5}Se_{0.5}$ and a-$Ge_{0.4}Se_{0.6}$ and the Ge-Ge bond for the Ge-rich sample as well with the shortest bond being at 2.45 Å, which is consistent with the value of the Ge-Ge bond in elemental Ge [LZF17]. Lastly, a peak at 2.35 Å for Se-Se RDF in the Se-rich stochiometry is consistent with the bond distance in elemental Se. In the Ge-Se panel, the dashed line representing the Ge-Se bond in the crystalline GeSe aligns with the first peak in a-Ge_xSe_{1-x}, indicating the Ge-Se bond length. In the Ge-Ge and Se-Se panels, the dashed line is close to the second neighbor peak, suggesting bonds angles centered about the same value in the crystal and the amorphous materials, although the distribution in the latter case are quite broad.

The structural stability of amorphous chalcogenides is determined by their mean coordination number (MCN) [Phi79]. For chalcogenide glasses like GeSe, Tanaka's work reveals that the structural phase transition from floppy to rigid occurs when the mean coordination number is 2.67. A material with an MCN larger than Tanaka's threshold indicates a 3D network structure. Our results show an MCN of 3.06 for a-$Ge_{0.5}Se_{0.5}$, close to the theoretical predicted value of 3 by Tanaka [Tan89] obtained based on the 8-N rule, and 3.24 for a-$Ge_{0.6}Se_{0.4}$ compared to the theoretically predicted value of 3.2 [Tan89]. For the Se-rich structure, the MCN is 2.96, close to the theoretical predicted value of 2.8 [Tan89]. Therefore, our structural models for a-Ge_xSe_{1-x} have on a coordination close to the 3(Ge):3(Se) found in crystals (see table 4.2), although the amorphous models show a three-dimensional network while the crystal has a layered structure.

	Ge	Se
a-$Ge_{0.4}Se_{0.6}$	3.3134	2.623
a-$Ge_{0.5}Se_{0.5}$	3.232	2.946
a-$Ge_{0.6}Se_{0.4}$	3.593	2.895

Table 4.2: The average coordination number of the Ge and Se in a-Ge_xSe_{1-x}

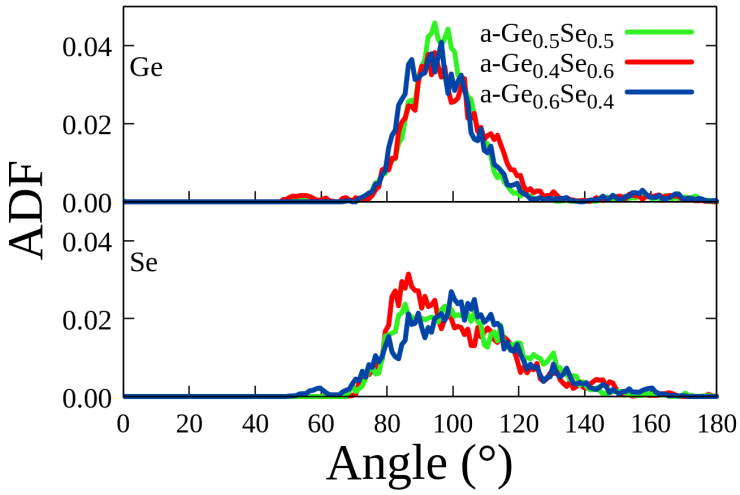

Figure 4.3: Angular distribution function of the a-$Ge_{0.4}Se_{0.6}$, a-$Ge_{0.5}Se_{0.5}$, and a-$Ge_{0.6}Se_{0.4}$.Top panel Ge-center and bottom panel Se-center ADF.

The top and bottom panels of figure 4.3 show the Ge-centered and the Se-centered angle distribution function of a-Ge_xSe_{1-x}. The Ge-centered ADF shows a symmetrical bell shape around 90° for all three stoichiometries. The a-$Ge_{0.5}Se_{0.5}$ and a-$Ge_{0.4}Se_{0.6}$ samples exhibit similar trends across the entire angle range while the distribution is a bit narrower for the a-$Ge_{0.6}Se_{0.4}$. For the Se-centered ADF, a-$Ge_{0.5}Se_{0.5}$ and a-$Ge_{0.6}Se_{0.4}$ are again quite similar. For a-$Ge_{0.6}Se_{0.4}$, a little hump appears at a smaller angle of about 60° . This indicates the presence of some edge-sharing tetrahedra, where two Ge-centered sub-units share two Se atoms or one Se atom.

For the Se-rich sample, the main peak of the Se-centered ADF is shifted toward smaller angles with a maximum around 90° . The se-rich sample follows the same trend as the two other stoichiometries at large angles. With the increase in Ge atoms

content, the Se-centered ADF of the a-$Ge_{0.5}Se_{0.5}$ and the a-$Ge_{0.6}Se_{0.4}$ configuration shift to larger angles around 109.5° , characteristic of tetrahedral units. The increase in Ge atoms content leads to a broader distribution of angles and a wider range of structural motifs.

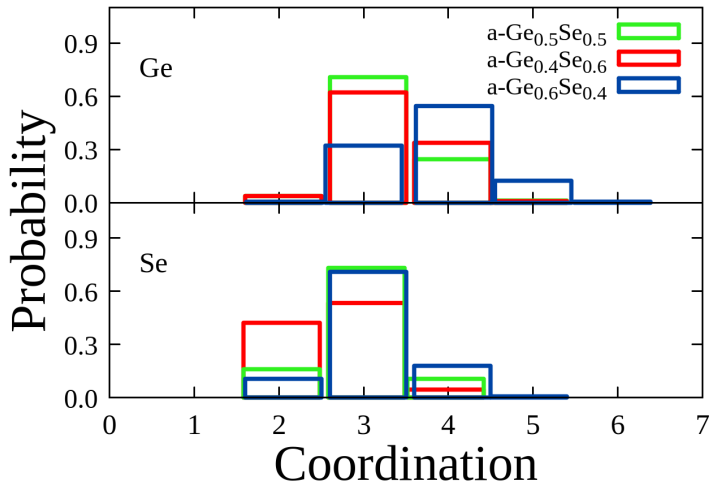

Figure 4.4: Coordination analysis of a-Ge_xSe_{1-x}. The top and panels show the Ge and Se coordination numbers, respectively

Figure 4.4 shows the Ge and Se coordination analysis of the a-$Ge_{0.4}Se_{0.6}$, a-$Ge_{0.5}Se_{0.5}$, and a-$Ge_{0.6}Se_{0.4}$. The Ge is primarily 3- and 4-fold coordinated in the a-$Ge_{0.5}Se_{0.5}$ stoichiometry, with 3-fold coordination being the most frequent. The coordination number for Ge increases in a-$Ge_{0.6}Se_{0.4}$, for which the most frequent is a four-fold structure, and where a substantial proportion of Ge is 5-fold and even one Ge atom is 6-fold coordinated. This hexacoordinated Ge indicates the presence of a distorted octahedral motif in the amorphous network, confirmed by the bond angle distribution function with a peak at 90° (see figure4.3).

For the Se-rich sample, the Ge coordination is very similar to the stoichiometric compound, 3 being the most frequent, but with a significant number of 4-fold Ge atoms (larger than in the stoichiometric material) and some 2- and 5-fold ones. The divalent Ge proportion remains unchanged compared to the a-$Ge_{0.5}Se_{0.5}$ sample.

For the Se coordination (bottom panel), in the a-$Ge_{0.5}Se_{0.5}$ stoichiometry, Se is mainly 2-, 3-, and 4-fold coordinated, with the predominant coordination being 3-fold. Upon increasing the Se content, the Se-coordination shifts to lower values, with

the proportion of 2-fold atoms growing significantly but with 3-fold coordination still being the most frequent.

Conversely, in the a-$Ge_{0.6}Se_{0.4}$ sample, increasing the Ge content raises the Se coordination, enhancing the frequency of 4-fold atoms and reducing the number of 2-fold ones. In our sample, we even observe one 5-fold Se atom.

In contrast to Figure 4.4, which shows the coordination of each atomic species independent of the species it forms a bond with, Table 4.3 presents the statistics of the homopolar bonds and existing tetrahedra in a-Ge_xSe_{1-x}. The first column lists the compositions, while the other three columns show the counts of Ge-Ge bonds, Se-Se bonds, and tetrahedra, respectively. From Table 4.3, in agreement with Figure 4.2, the a-$Ge_{0.6}Se_{0.4}$ sample has more Ge-Ge bonds and Ge-centered tetrahedra than the a-$Ge_{0.5}Se_{0.5}$ and a-$Ge_{0.4}Se_{0.6}$. Meanwhile, the count of Se-Se bonds is higher in a-$Ge_{0.4}Se_{0.6}$ than in a-$Ge_{0.5}Se_{0.5}$ and is nonexistent in the Ge-rich sample.

	#Ge-Ge	#Se-Se	# Ge-center tetrahedra (percentage %)
a-$Ge_{0.6}Se_{0.4}$	174	0	59 (34.23)
a-$Ge_{50}Se_{50}$	26	2	19 (11.30)
a-$Ge_{0.4}Se_{0.6}$	10	53	26 (19.4)

Table 4.3: Statistics of the Ge-Ge bonds, Se-Se bonds, and Ge-centered tetrahedra in a-Ge_xSe_{1-x}

We now analyze the ring statistics to study the amorphous network. This analysis of the topology of the networks allows us to gain insight into the structural motifs present in the structure. A ring is defined as a closed path, and a path is a series of nodes (atoms) connected sequentially (atomic bond) without redundancy. The total nodes of rings form a close path with n nodes, denoted as n-membered rings. The ring statistics hereafter have been carried out using 10 nodes as a maximum search depth. We use the primitive ring criterion [RJ10] to define this path as the shortest, which returns to a given atom from one of its nearest neighbors.

Figure 4.5 shows each ring size's proportion and connectivity from 3 to 10 in the amorphous network. $Rc(n)$ [RJ10] is the number of rings per cell. It is calculated by counting all the different rings of size n corresponding to the primitive ring criterion. In all the stoichiometries, there is a similar proportion of rings per cell with a size of 4. Rings with homopolar bonds (i.e., odd-sized rings) exist in all sizes analyzed. This confirms the existence of chemical defects in the amorphous network as indicated by homopolar bonds in the RDF (see figure 4.2). This is in agreement with the AIMD simulations results by [CD97; CDC96; MP08; MPC01] in the structure of glassy $GeSe_2$ whereby n-member rings from 3 to 10 exist.

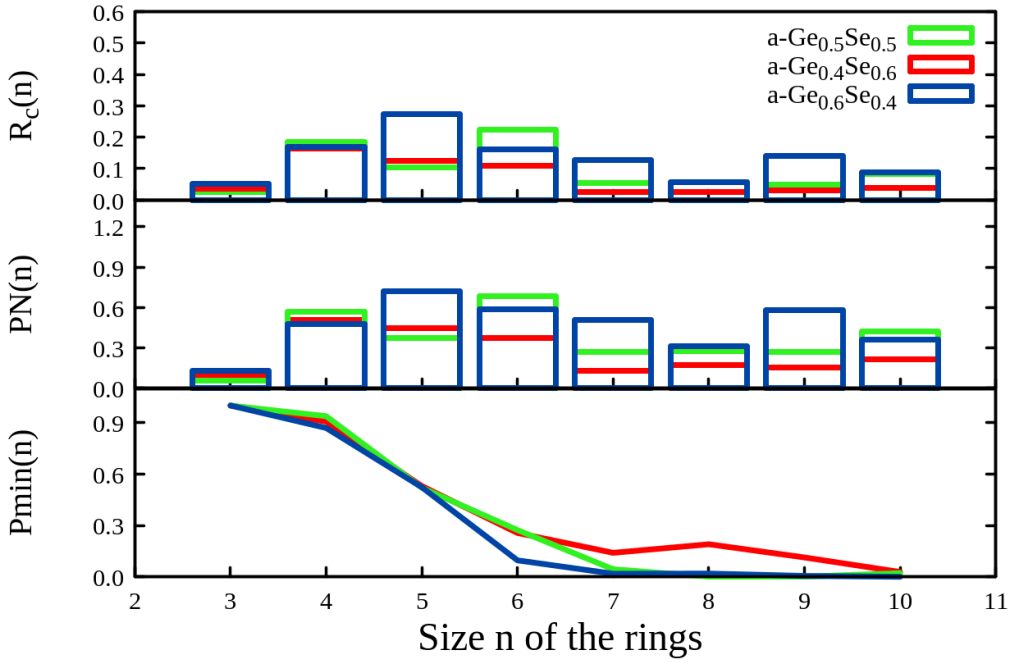

Figure 4.5: The connectivity profiles of a-Ge_xSe_{1-x} samples.

The 4- and 6-membered rings are predominant motifs in a-$Ge_{0.5}Se_{0.5}$, 4, 5, and 6-membered rings are predominant features for the a-$Ge_{0.4}Se_{0.6}$ whereas 5-membered rings are more frequent in a-$Ge_{0.6}Se_{0.4}$. We recall that the crystalline GeSe is made of 6-membered rings. As observed by D.E. Polk [Pol71], including the pentagonal rings does lead to a less pronounced third neighbor peak (see figure 4.2). So, the more a sample has a 5-membered ring, the less pronounced the third neighbor peak in the RDF will be.

The size of the rings and their chemical character (rings with or without homopolar bonds) are not enough to understand the spatial distribution of the rings across the networks. So, following [RJ10], we present other quantities useful for understanding the connectivity in the amorphous network. We first show the results for $PN(n)$, the total number of nodes that satisfy the primitive ring criterion divided by the total number of nodes in the amorphous network. A high value of $Rc(n)$ and a low value of $PN(n)$ will indicate local network defects [RJ10] since all nodes are not necessarily in rings of that size. A local network defect represents a localized irregularity that alters the overall topology or bonding pattern of the material.

Tables 4.4, 4.5, and 4.6 show the ring statistics and the connectivity profile of a-$Ge_{0.5}Se_{0.5}$, a-$Ge_{0.4}Se_{0.6}$, and a-$Ge_{0.6}Se_{0.4}$, as plotted in Figure 4.5. For a-$Ge_{0.5}Se_{0.5}$, we observe no local network defects for 3- and 6-membered rings, as seen in Table 4.4, where for $n = 3$ and $n = 6$, PN(n) is greater than Rc(n). For a-$Ge_{0.4}Se_{0.6}$, local network defects are only found in 5- and 6-membered rings, as seen in Table 4.5, where for $n = 5$ and $n = 6$, Rc(n) is greater than PN(n). For a-$Ge_{0.6}Se_{0.4}$, no local network defects are found for any ring size distribution from 3 to 10, as seen in Table 4.6, where PN(n) is always greater than Rc(n).

Size of the ring (n)	Number	Rc(n)	PN(n)	Pmin(n)
3.0	8	0.024	0.060	1.000
4.0	62	0.185	0.571	0.938
5.0	35	0.104	0.372	0.520
6.0	75	0.223	0.688	0.273
7.0	18	0.054	0.268	0.044
8.0	19	0.057	0.280	0.000
9.0	16	0.048	0.271	0.000
10.0	28	0.083	0.423	0.021

Table 4.4: Rings statistics and the connectivity profile of the a-$Ge_{0.5}Se_{0.5}$. No local network defects for 3- and 6-membered rings.

Size of the ring	Number	Rc(n)	PN(n)	Pmin(n)
3.0	12	0.036	0.101	1.000
4.0	55	0.164	0.509	0.906
5.0	42	0.125	0.449	0.530
6.0	37	0.110	0.372	0.256
7.0	8	0.024	0.128	0.140
8.0	8	0.024	0.173	0.190
9.0	10	0.030	0.158	0.113
10.0	13	0.039	0.214	0.028

Table 4.5: Rings statistics and the connectivity profile of the a-$Ge_{0.4}Se_{0.6}$. Local network defects are only found in 5- and 6-membered rings

We also evaluate $Pmin(n)$, the proportion of nodes for which the rings with n nodes are the shortest closed paths found using these nodes to initiate the search. $Pmin(n)$ is not defined with respect to all nodes but rather with respect to all atoms that are at the origin of rings of size 'n'

Size of the ring	Number	Rc(n)	PN(n)	Pmin(n)
3.0	17	0.051	0.131	1.000
4.0	57	0.170	0.476	0.869
5.0	92	0.274	0.723	0.523
6.0	54	0.161	0.586	0.096
7.0	43	0.128	0.506	0.018
8.0	19	0.057	0.312	0.019
9.0	47	0.140	0.583	0.005
10.0	30	0.089	0.363	0.000

Table 4.6: Rings statistics and the connectivity profile of the a-$Ge_{0.6}Se_{0.4}$. No local network defect was found in any of the ring size distributions.

For $n \leq 4$, Pmin is approximatively equal to 1; therefore, rings with size n less than or equal to 4 are always the shortest path for the node at the origin of the search. Therefore, in a-Ge_xSe_{1-x}, there is no common node between rings of 3 and 4 nodes.

The structural analysis of a-Ge_xSe_{1-x} shows that all our generated samples are primarily Ge(3):Se(3) coordinated. For all three stoichiometries, the Ge-Se bond is favored and has a similar bond length to that in the crystal structure of orthorhombic GeSe. However, Ge-Ge and Se-Se homopolar bonds become significant as the concentration of Ge or Se is increased by 10% relative to the quasi-stoichiometric sample, respectively. Ring statistics further confirm the existence of homopolar bonds, contributing to chemical defects in the amorphous network and local network defects.

4.2 Electronic properties

We now analyze the electronic properties of our a-Ge_xSe_{1-x} models. We start by showing, in Figure 4.6, the density of states (DOS) of crystalline orthorhombic GeSe and the three stoichiometries of a-Ge_xSe_{1-x}. The electronic DOS for both c-GeSe and a-Ge_xSe_{1-x} exhibit very similar overall profiles, with four distinct regions in the energy interval considered: three in the valence band (VB) and one in the conduction band (CB). The two lowest groups of states, in the ranges [-15 eV, -10 eV] and [-10 eV, -5 eV], have mainly Se(4s) and Ge(4s) characters, respectively. In contrast, the topmost valence band, in the [-5 eV, 0 eV] range, and the lowest conduction band, in the interval [0 eV, 5 eV]. are primarily composed of Se(4p) and Ge(4p) states, with predominance of Se(4p) states in the valence band and Ge(4p) in

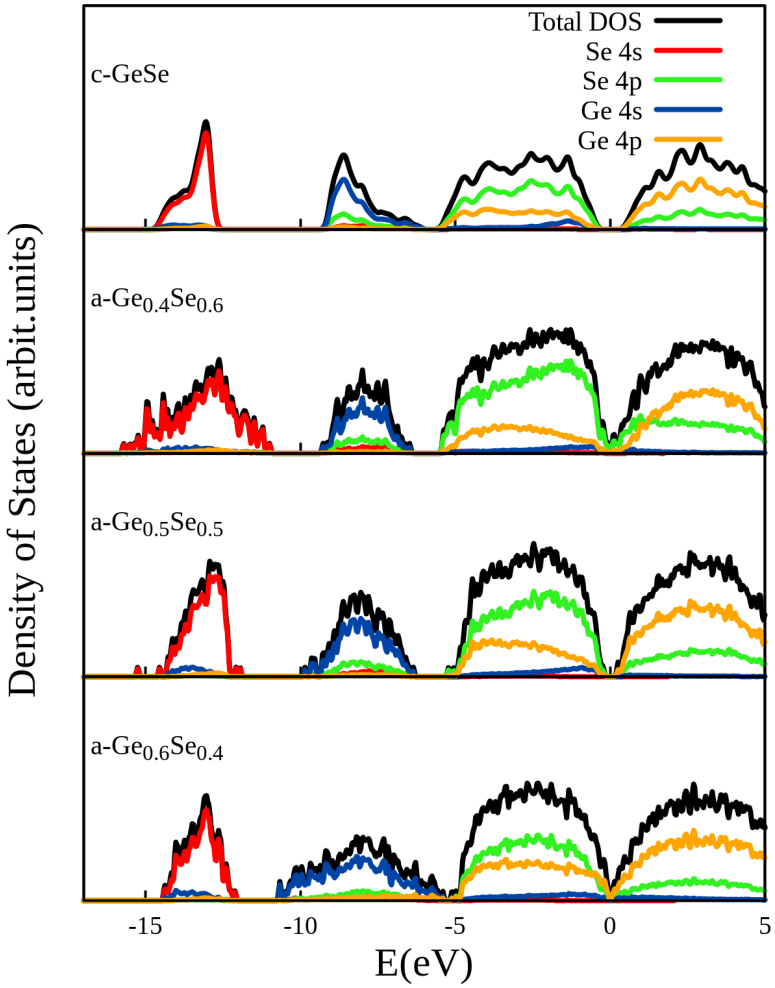

Figure 4.6: The density of states and projected DOS (pDOS) of each orbital of different atom species of the crystal GeSe and a-Ge_xSe_{1-x} at different Ge/Se ratios: c-GeSe, a-$Ge_{0.4}Se_{0.6}$, a-$Ge_{0.5}Se_{0.5}$, and a-$Ge_{0.6}Se_{0.4}$. The energies are Fermi level corrected.

the conduction band. The similarity in the DOS of all compounds is not surprising, as the bonding structure of the amorphous materials, as explained in the previous section, is close to that of the crystalline compound, with a coordination close to 3:3, and predominance of heteropolar bonds between the two species Ge and Se. The main covalent nature of these bonds then leads to very similar DOS and contributions of each species and atomic orbital in the same energy region. It is worth noticing that while the overall contribution of Se(4p) states to the DOS in the top valence and lower conduction bands increases with Se content (as would be expected), the ratio of the weight of the partial DOS of these orbitals in the valence and conduction band remains quite similar. The same consideration holds for the Ge(4p) states, which, of course, decrease their weight as the Se content increases. It is also interesting to notice that, in the Se-rich sample, the Se(4p) contribution is larger than that of the Ge(4p) orbitals in the low-energy edge of the conduction band. A similar effect can be observed in the Ge-rich sample, where the Ge(4p) weight is predominant at the highest energies of the top of the valence band. This is due to the increase in Se content in the Se-rich sample and the increase in Ge content in the Ge-rich sample, which result in Se-Se bonds and Se lone pairs at the origin of localized states in the Se-rich sample, as well as Ge-Ge bonds in the Ge-rich sample, which give rise to a broad tail of the conduction in energies range close to the Fermi level. As we shall see later, Ge-Ge bonding configurations create conduction band tail states in agreement with [LR19].

The energy difference between the mobility edges defines the mobility gap (E_g), while the spectral band gap is defined as the energy range with no states whatsoever. When a charge carrier falls into localized states, it gets trapped. A charge carrier (electron or hole) in a trap state typically has an exponentially decaying wavefunction localized in a spatially restricted region.

4.2.1 DFT+U

Herein, we check if improving the treatment of electron correlations by considering the on-site Coulomb term, U, the electronic structure, and then the structural motif responsible for the localized states may differ from the standard density functional theory. Using the same value of U as found in the crystal in section 2.2, we computed the electronic density of states of the undoped a-Ge_xSe_{1-x} with and without the U correction (see figure 4.7). From figure 4.7, we notice that the DFT+U method modifies the DOS profiles compared to standard DFT. The green DFT+U lines show slight deviations from the black DFT lines. The DFT+U correction widens the spectral band gap in the Se-rich and stoichiometric samples, indicating a better approximation of electronic correlation effects that DFT alone might not capture.

However, these differences are minor, and after testing, those slight variations have no impact on the structural motif at the origin of the localized states in the mobility gap. [4].

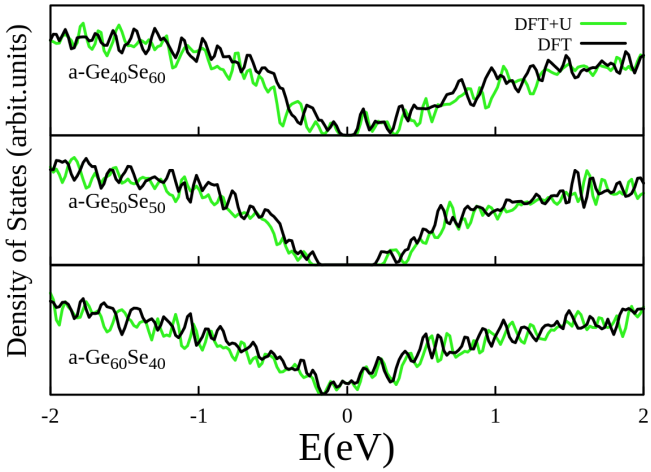

Figure 4.7: Density of states of amorphous GeSe with (green curve) and without (black curve) the Hubbard correction, with U_{Ge} = 0.14 eV and U_{Se} = 1.995 eV.

Figure 4.8 represents the DOS and the inverse participation ratio of all three stoichiometries. Some states clearly appear localized within the mobility edges, with higher IPR.

a-$Ge_{0.5}Se_{0.5}$ has very few localized states, and all of them are located close to the mobility edge, leading to a clean and large spectral band gap. For this stoichiometric amorphous sample, E_g is similar to that of crystalline GeSe. The Fermi energy lies between two resonant states, defined as states that are symmetric with respect to the Fermi level at energies of -0.235 eV and 0.237 eV. This amorphous sample is similar to the Marshall-Owen model [MO71], wherein the defect states lead to localized energy states in the form of electron and hole traps in the band gap.

The a-$Ge_{0.4}Se_{0.6}$ has many localized states within the mobility band gap, although mobility edges both in the valence and the conduction band can be clearly identified by looking at the localization of the states through the IPR. Actually, the mobility

4 Even though it is not shown or discussed in any of the chapters of this thesis, the DFT+U has also been tested when adding various dopants against the standard DFT calculation. Adding the Hubbard correction does not significantly modify the electronic density of states nor the structural motifs at the origin of localized states in the mobility gap.

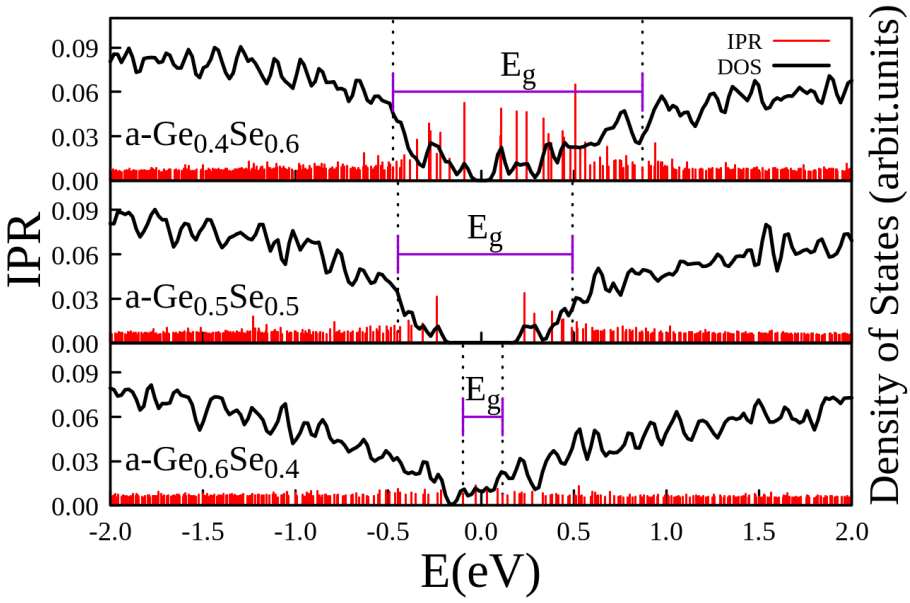

Figure 4.8: Density of states (black curve) and inverse participation ratio (red spikes) of the three stoichiometries in the range of energies near the Fermi energy.

gap for this sample is larger than for the stoichiometric a-$Ge_{0.5}Se_{0.5}$ compound. The Fermi energy lies between two localized states at -0.09 eV and 0.09 eV. The tail of the localized state extends a few tenths of eV into the mobility gap. This sample is similar to the Davis-Mott model of an ideal amorphous semiconductor with defects near the center of the mobility gap [DM70].

The Ge-rich sample shows no spectral band gap, with a quite continuum spectrum of states around the Fermi level. The conduction and the valence band tail overlap in the midgap, leading to an appreciable density of states across the mobility gap. Actually, for this concentration, it is difficult to define a mobility gap, as all the states have a considerably small IPR, being, therefore, quite delocalized. As a result of band overlapping, redistribution of electrons must occur, which forms filled states in the conduction band tail, which are negatively charged, and empty states in the valence band, which are positively charged. This sample is similar to the model proposed by Cohen-Fritzsche-Ovshinsky (CFO) [CFP67].

In summary, the mobility gap, E_g, increases with the decrease in the Ge content, as seen in Table 4.7. To evaluate the E_g, we compute the average value of the IPR, far from the Fermi energy, and the standard deviation of these data. Then, we define a localized state as a state whose IPR is greater than 1 time the standard deviation and 2 times the standard deviation. These two definitions of the localized states allow us to estimate the error.

Sample	E_g (eV)
a-$Ge_{0.4}Se_{0.6}$	1.3947/1.0971
a-$Ge_{0.5}Se_{0.5}$	1.1822/1.0602
a-$Ge_{0.6}Se_{0.4}$	0.6577/0.2134

Table 4.7: The mobility gap E_g for different samples. The first value of E_g is computed by considering the localized as those greater than one time the standard deviation, and the second value represents those obtained by defining the localized as those greater than 2 times the standard deviation.

4.3 Linking the electronic properties to the structural features

In this section, we aim to analyze the structures of the amorphous samples which lead to localized states within the mobility gap. To do that, we establish the link between the IPR for each state localized within the mobility gap and the structural

local environment of the atoms involved. These are identified by looking at the electron occupation of that state on each atom in the supercell. Once the atoms with the highest weight of the electron occupation are found, their local environments are investigated and visualized by plotting the wave function together with the bonding network.

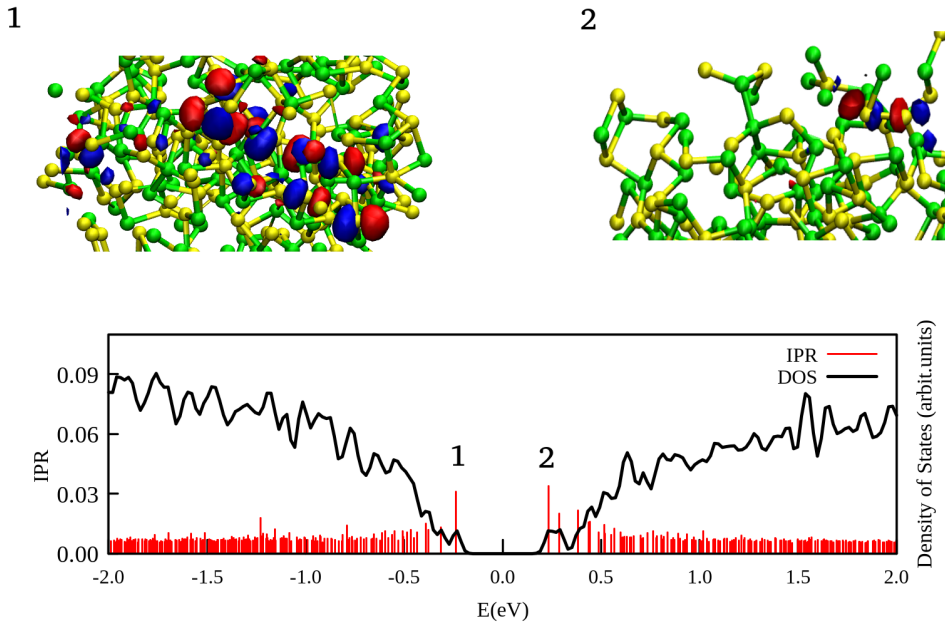

Figure 4.9: Top: Single-particle wave functions of selected defect states in the mobility gap of the a-$Ge_{0.5}Se_{0.5}$ sample. The red and blue isosurfaces indicate the positive and the negative sign of the wavefunction, respectively. Bottom: DOS (black curve) and the IPR (red spike) of the model. States shown at the top are numbered according to the labels in the bottom graph. The localized states shown are due to 1) Se lone pair and 2) Se-Se σ^*

4.3.1 a-$Ge_{0.5}Se_{0.5}$

Figure 4.9 shows the wave function and the structural environments that give rise to localized states in our a-$Ge_{0.5}Se_{0.5}$ model. The top panel shows three wave functions and the structural environments associated with the localized states numbered in the bottom panel.

We first analyze the localized states in the a-$Ge_{50}Se_{50}$ model, which shows the cleanest spectral gap and a few localized states within the mobility gap.

For state "1" in Figure 4.9, the localized state is due to the Se lone pairs (LP) of Se atoms not forming a bond. The first Se atom, which has the highest electron occupation, belongs to a 5-membered ring, while the second Se atom, with half the electron occupation of the first, belongs to the 4-membered ring.

The Se atoms at the origin of the localized state belong to 4 and 5-membered rings. This is not surprising because previously, from the ring statistics analysis, we showed that in the a-$Ge_{0.5}Se_{0.5}$ sample, local network defects were found on the 4 and 5-membered rings. A local network defect represents a localized irregularity that alters the material's overall topology or bonding pattern.

For state "2", the two Se atoms involved in the formation of the localized state are separated by a distance of 2.42 Å, which corresponds to the shortest of the two first-neighbour Se-Se bonds that appear as a little hump in the RDF see figure 4.2. The remaining Se-Se bond of length Se-Se =2.49 Å does not belong to a 4- or 5-membered ring. Thus, it is not at the origin of any localized state. As shown in the ring statistics analysis, local network defects are found in the 4 and 5-membered rings.

The angle formed by the three atoms with the highest electron occupation in creating the localized state is Se-Se-Ge = 98.40°. Two distorted Ge tetrahedra, which share a common Ge corner, form a 5-membered ring with the 2 Se atoms involved in the formation of the localized state. The homopolar bond lengths forming the 5-membered ring are Se-Se = 2.42 Å and Ge-Ge = 2.64 Å. Se LPs and the homopolar Se-Se σ^* bond give rise to states resonant with the valence and conduction bands. In general, for the a-$Ge_{0.5}Se_{0.5}$ case, the localized states are predominately formed by Se-Se σ^* bonds in the conduction band, and a small fraction of localized state is due to the p orbitals in the Se LP. No valence alternation pair is found. From the ring statistics analysis, we found local network defects in 4- and 5-membered rings.

4.3.2 a-$Ge_{0.4}Se_{0.4}$

Figure 4.10 shows wave functions of the a-$Ge_{0.4}Se_{0.6}$ for three different cases of localized states originating from different structural motifs. State "1" shows a wave function in the valence band due to the Se-Se π^* chain. In state "2", the localized state is due to the Se LP. From the ring statistics analysis, local network defects which represent localized irregularities that alter the overall topology or bonding pattern of the materialare found only in 5- and 6-membered rings, which is the case here. In state "3", the localized state is due to the Ge tetrahedron found on 6- and 5-membered conjoined rings.

The predominant structural environments that give rise to localized states in a-$Ge_{0.4}Se_{0.6}$ are the Se-Se bonds and a minor contribution of Se LP and tetrahedra.

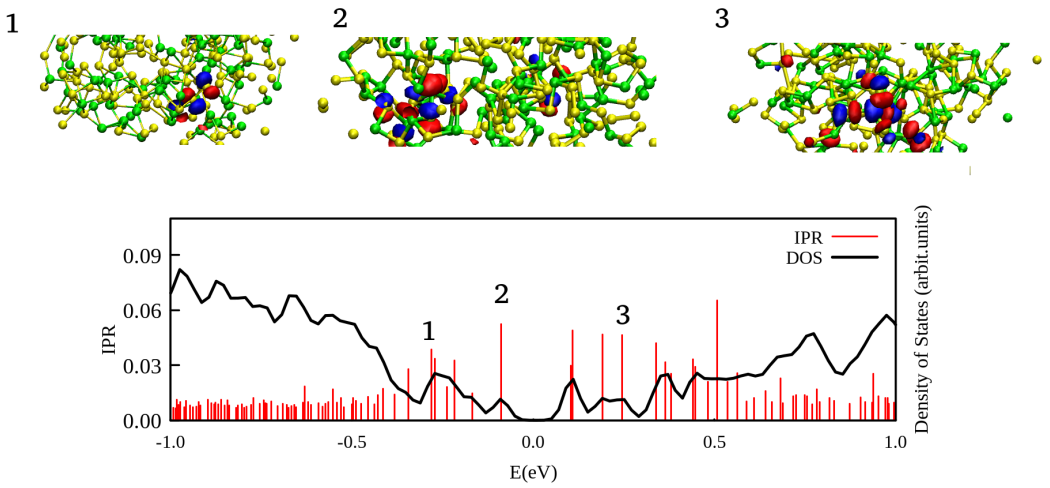

Figure 4.10: Plot of the wave functions plot of selected defect states 1, 2, 3 in the mobility gap of a-$Ge_{0.4}Se_{0.6}$ sample. The red and blue isosurfaces indicate the positive and the negative sign of the wavefunction, respectively. 1) the localized state is due to the Se-Se π^* chain, 2) the localized state is due to Se LP, and 3) the localized state is due to a tetrahedron (q = 0.94).

The Se-Se bond is of the π^* type when the defect state is located in the valence band and the σ^* type when the defect state is located in the conduction band.

4.3.3 a-$Ge_{0.6}Se_{0.4}$

Figure 4.11 top panel shows the isosurface representation of the most localized state in the Ge-rich sample. The localized states near the Fermi level in the $Ge_{0.6}Se_{0.4}$ sample are weaker than in the Se-rich and the quasi-stochiometric sample, with small values of the IPR for all the states. For the most localized state of the a-$Ge_{0.6}Se_{0.4}$ model seen in figure 4.11, the two Ge atoms with the highest electron occupation are positioned at the centroid of slightly distorted tetrahedra (Ge(q=0.89) and Ge(q=0.95), where q represents the orientational order parameter for the tetrahedral structural motif as defined in [ED01]). Thus, the two Ge atoms involved in forming the most localized state in the Ge-rich sample obey the 8-N rule. They form a bond and are part of a five-membered (pentagonal) ring with four other Ge atoms. . As with the previous sample, the existence of a local network defect in the ring statics results in a localized state near the band edge. In Figure 4.11, the wave function is extended all over the cell. The non-localization of the wave function

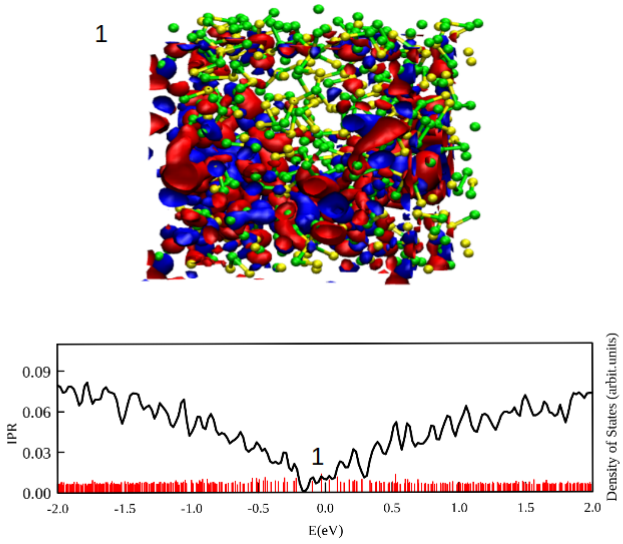

Figure 4.11: Isosurface representation of the most localized state in amorphous a-$Ge_{0.6}Se_{0.4}$. The red and blue isosurfaces indicate the positive and the negative sign of the wavefunction, respectively. The bottom panel shows the DOS (black curve) and the IPR (red spikes).

agrees with the results of the ring statistics analysis. Whereby no local network defects were found in any of the rings from 3 to 10.

Consequently, in the a-$Ge_{0.6}Se_{0.4}$ model we generated, all the states are extended, indicating that the sample is defect-free as it satisfies all the conditions stated in [Zac32] for a sample to be considered as such. In addition to satisfying the 8-N rule, the two Ge atoms are each the centroid of a tetrahedron, meaning the bond lengths and ∠(Se-Ge-Se) bond angles are constant, with no dangling bonds.

4.4 Conclusions

We have developed realistic density functional theory-based structural models of amorphous GeSe without resorting to experimental information or adjusted interatomic potentials. We constructed various supercell models, for three compositions of a-$Ge_{0.6}Se_{0.4}$ (with x=0.4, 0.5, 0.6). The networks are disordered by density functional molecular dynamics in a melt-and-quench protocol. The structural features of these samples, including the radial distribution function, the angle distribution function and the coordination number have been calculated. Our results show that the a-Ge_xSe_{1-x} is Ge(3): Se(3) coordinated. Well-defined Ge-Se first-neighbor shells

are found, similar to the Ge-Se bond in the GeSe crystal structure. We observe Ge and Se clustering in Ge-rich and Se-rich structures, respectively; the Ge-rich structure tends to have larger coordination numbers than the Se-rich structure. The a-$Ge_{0.5}Se_{0.5}$ sample we generated has a very small number of Ge-Ge and Se-Se bonds. The electronic properties features, including the inverse partition ratio and the density of states, have been calculated. The stochiometry sample has a clean spectral band gap, and some localized states within the mobility gap. We show the structural motifs at the origin of localized states in the mobility gap. Localized states are predominantly due to the Se-Se bonds in the Se-rich sample and a minor contribution to Se LP and tetrahedra. In a-$Ge_{0.5}Se_{0.5}$, defect states are due to the Se-Se, σ^* bond type in the conduction band. For the a-$Ge_{0.6}Se_{0.4}$ stochiometry, we find no spectral gap, and very delocalized states throughout the energy range, with no significantly localized states.

5 Doped a-GeSe

5.1 Introduction

In 1967, Mott [Mot67] introduced the 8-N rule to account for the absence of topological constraints in covalently bonded tetrahedral amorphous structures, resulting in the absence of doping. This rule states that each element has a natural coordination determined by its valence electrons (N)[Str82]. For example, Se has $N = 6$ valence electrons, resulting in a coordination of 2, while Ge, with 4 valence electrons, has a coordination of 4. This rule suggests that substitutional doping, a process in which the dopant becomes electrically active in a 4-fold bonded configuration, providing the material with charge carriers, could not occur in amorphous semiconductors. However, doping was demonstrated by Spear et al. [SL75] in hydrogenated amorphous silicon. They have shown that the electrical conductivity of a tetrahedral amorphous semiconductor can be controlled over many orders of magnitude by doping with substitutional dopants.

However, experiments show that most excess carriers introduced by dopants do not occupy shallow tail states, as expected in intrinsic semiconductors, but rather form mid-gap states [SBS87]. In addition, the properties of tetrahedrally bonded amorphous materials such as a-Si, differ from those of chalcogenide glasses in the sense that the former can generally be prepared so that the Fermi level is unpinned from the center of the band gap [Adl81; AY77; MD71]. Consequently, the electrical conductivity can be modulated, e.g., by chemical doping or the field effect. The pinning of the Fermi level at the center of the gap in amorphous chalcogenides, characterized by charged defects D^+ and D^-, is responsible for p-type conduction in chalcogenides [Bha+86]. However, dopants induced structural changes that can modify the electronic conductivity by balancing the charged defects D^+ and D^-, thus moving the Fermi level toward the conduction band or the valence band. Kastner et al. [KAF76] proposed a specific type of defect, called a bond alternation pair, responsible for pinning the Fermi level. This defect creates over- and under-coordinated atoms, known as valence alternation pairs (VAPs), with an effective interaction pair of electrons in a nonbonding level (U). The negative U effect, coined by Anderson [And75], ensures strong Fermi level pinning with no measurable unpaired spin density. VAPs, in which the total number of bonds is preserved, are formed by the lone pair electrons in chains of chalcogen atoms (S, Se, Te) and have

been identified as responsible for traps associated with Ovonic Threshold Switching (OTS) [Ava+17; IZ07]. The creation energy of VAPs is lower than the total energy of the neutral defects in amorphous chalcogenides.

It was generally admitted that most chalcogenide glasses exhibit p-type conduction and that their electrical conductivity is slightly affected by doping. This insensitivity to dopants is due to charged defects pinning the Fermi level near the mid-band gap [KAF76; NS75]. Tohge et al. [TMT80; Toh+80] were the first to highlight the role of Bi, which belongs to the pnictogen family (along with P and As), in the emergence of n-type conduction in chalcogenide glasses. In 1986, Bhatia et al. [Bha+86] found that bismuth dopants induced structural modifications in $(GeSe_{3.5})_{1-x}Bi_x$ glasses that are responsible for n-type doping using IR and Raman spectra. The mechanism behind this is still controversial: what is the charge of the pnictogen atom, and what is its local environment? Several answers have appeared in the literature since the 1980s.

This n-type conduction was also found by Nagels et al. [NRV81] in $(GeSe_{3.5})_{1-x}Bi_x$ and $(GeSe_3Te_{0.5})_{1-x}Bi_x$ and attributed to negatively charged, 2-fold coordinated Bi atoms. Tohge et al. [TMT80] and Vautier and co-workers [VSD88] proposed that in the $Ge_{0.2}Bi_xSe_{0.8}$ alloys ($0 < x < 0.13$), the Bi atoms were 6-fold coordinated and negatively charged. In 2014, Seo et al. [Seo+14] showed that increasing the Bi content reduces the optical energy gap and the depth of trap states, resulting in a drastic reduction of the threshold voltage (V_{th}) by more than 50%. Additionally, a smaller E_g is expected to result in a lower V_{th}, according to a model recently proposed by Ielmini [Iel08; IZ07].

The pnictogen-doped amorphous chalcogenides and the Te-based chalcogenides have recently attracted significant research interest. In 2014, Yu et al. [YR14] raised uncertainty about whether the VAP model should apply to Te-based chalcogenide glasses, such as GeSbTe, especially since tellurides exhibit more metallic bonding than selenides, with a much smaller band gap and more back bonding in their crystalline phase. It is yet to be determined if the VAP model applies to amorphous GeSe under doping conditions. However, in equiatomic compositions of a-GeSe, very few homopolar Se-Se bonds are expected.

Significant progress has been made in experimental studies of doped chalcogenide glasses. Modulating Ge concentration and layer thickness can affect switching characteristics. Dopants like N [Ahn+13], Sb [Shi+14], and Bi [Seo+14] have also been studied for different values of x (ranging from 0.4 to 0.7) to modulate the threshold voltage. Additionally, the thermal and electrical performance of doped a-Ge_xSe_{1-x}, for $x = 0.4, 0.5, 0.6$, were studied upon adding C and N to the amorphous network. N doping was found to decrease off-state leakage and increase

the threshold voltage (V_{th}), while C doping led to increased leakage and reduced V_{th} [Ava+22].

This chapter focuses on the theoretical effect of dopants-induced n-type and p-type defects on the electronic and structural properties of amorphous GeSe. It explores the link between localized states and the presence of dopants. We use *ab initio* calculations based on DFT to study the effect of adding Si, P, As, S, and Te dopants to a-Ge_xSe_{1-x} for different values of x (ranging from 0.4 to 0.6). Using the structures with dopants generated from the melt-and-quench method with DFT as discussed in chapter 3, we get structures closely resembling the experimental ones. We will investigate the local structure, the effect of the dopants on the band gap, the density of states and the inverse participation ratio. Si, P, and As dopants are of interest due to their high connectivity and strong network-forming ability, which stem from their coordination numbers (As and P = 3, Si = 4), thus strengthening the structure. In contrast, S and Te, with 2-fold coordination, increase the network's flexibility [Ava+17].

The chapter is divided into three main sections: the first discusses Si-doped a-Ge_xSe_{1-x}; the second covers pnictogen-doped a-Ge_xSe_{1-x}, with the inclusion of As and P; and the third addresses chalcogenide-doped a-Ge_xSe_{1-x}, where S and Te are incorporated into the network. From a DFT perspective, our results reveal the importance of dopant-induced modifications in the amorphous GeSe network and electronic structure. Our approach provides a rigorous method for studying each localized state and mapping it to the electronic structure that gives rise to the defective states.

5.2 Silicon-doped a-Ge_xSe_{1-x}

This section aims to study the structural and electronic properties of the Si-doped a-Ge_xSe_{1-x}. In the structural section, we will show the radial distribution function, the angle distribution function, and the coordination analysis. In the electronic part, we will show the density of states, the inverse participation ratio, and the link between the localized states and the electronic structure.

5.2.1 Structural properties

To understand the structural properties of a-Ge_xSe_{1-x}:Si, the RDF, the ADF and the coordination analysis are shown. The RDF measures the probability of finding an atom at a specific distance r from a reference atom. The ADF represents the probability of atoms forming a certain bond angle with neighboring atoms in the

amorphous structure. The coordination analysis tells us about the local order in the amorphous network.

To study the effect of the dopant atoms on the amorphous structures, we compare their local structural features to those of Ge and Se atoms to determine whether they behave like one of them or exhibit different characteristics. This gives us some insights into the mechanism of the doping effect.

RDF

The partial RDFs of the Si-doped a-$Ge_{0.5}Se_{0.5}$, a-$Ge_{0.4}Se_{0.6}$, and a-$Ge_{0.6}Se_{0.4}$ are shown in figures 5.1, 5.2, and 5.3, respectively. Panel a) shows $g_{\text{Ge-Ge}}(r)$, b) $g_{\text{Se-Se}}(r)$, c) $g_{\text{Ge-Se}}(r)$, d) $g_{\text{Si-Ge}}(r)$, e) $g_{\text{Si-Se}}(r)$, and f) $g_{\text{Si-Si}}(r)$ as the concentration of Si increases.
In the stoichiometric and Ge-rich samples, the Ge-Ge partial RDF shows a first neighbor shell and a medium-range order (MRO); however, in the Se-rich samples, as the Si concentration increases, we notice an increase in the number of the Ge-Ge bonds.
No Se-Se first neighbor shell is found in the stoichiometric and the Ge-rich samples. In contrast, in the a-$Ge_{0.4}Se_{0.6}$ stoichiometry, as the Si concentration increases, we notice a decrease in the number of Se-Se first coordination shells and an increase in the number of Si-Se bonds. The latter indicates that Si is replacing Se. The absence of Se-Se bonds in the stoichiometric and Ge-rich samples indicates that Se atoms are not clustering together and are instead bonded to Ge or Si.
The Ge-Se first neighbor shell is well-defined in all the samples; however, the MRO is lost in the stoichiometric and Se-rich samples. Conversely, a medium-range order is observed in the Ge-rich sample. This is because Ge atoms prefer to bond with each other, as well as with Si and Se, creating a structurally ordered network at both the local and medium ranges.
In the stoichiometric sample, Si-Ge and Si-Se bonds are formed at all dopant concentrations. The Si-Ge first neighbor peak is around 2.5 Å, similar to the Ge-Ge clustering, indicating that Si behaves similarly to Ge when bonding to Se. In the Se-rich sample, Si prefers to bond with Se, while in the stoichiometric and Ge-rich samples, it tends to bond with both Se and Ge. The tendency of Si to bond with both Se and Ge in stoichiometric and Ge-rich samples shows the adaptability of Si in forming bonds depending on the local composition.
In the Se-rich sample, unlike the probability of finding a Si-Si bond, which exists only at higher concentrations of Si dopants, the proportion of Se-Se bonds diminished as the Si content increased—as mentioned earlier, suggesting that Si is replacing Se in the local bonding environment.
Homonuclear Si-Si bonds exist in the Ge-rich sample at most Si concentrations,

except 1%. The Si-Ge and Si-Se bonds are favored, and their corresponding RDF resembles each other, implying that Si bonds with both Ge and Se.
Si-Si bonds form at higher dopant concentrations in the stoichiometric sample. A first neighbor shell peak is observed at 2.35 ± 0.05 Å for 5%, and 15% of Si, and at 2.45 ± 0.05 Å for 10% Si. The 2.35 Å bond length is commonly reported for diamond cubic silicon, the most stable form of elemental silicon at room temperature and pressure. The error was calculated by dividing the bin width we used to compute the RDF by 2.

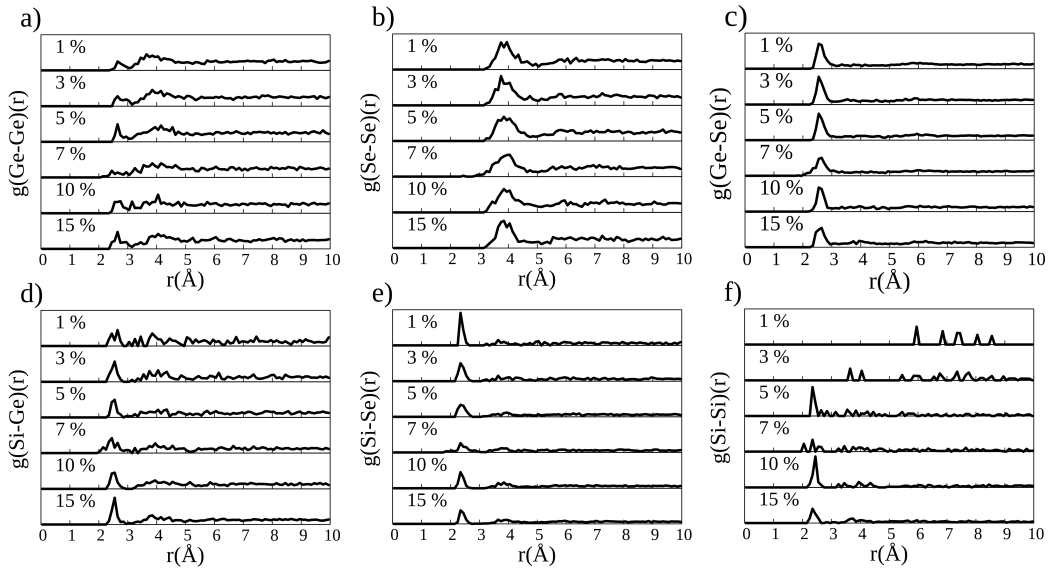

Figure 5.1: Partial radial distribution functions of the Si-doped a-$Ge_{0.5}Se_{0.5}$ for the pairs of a) Ge-Ge, b) Se-Se, c) Ge-Se, d) Si-Ge, e) Si-Se, and f) Si-Si.

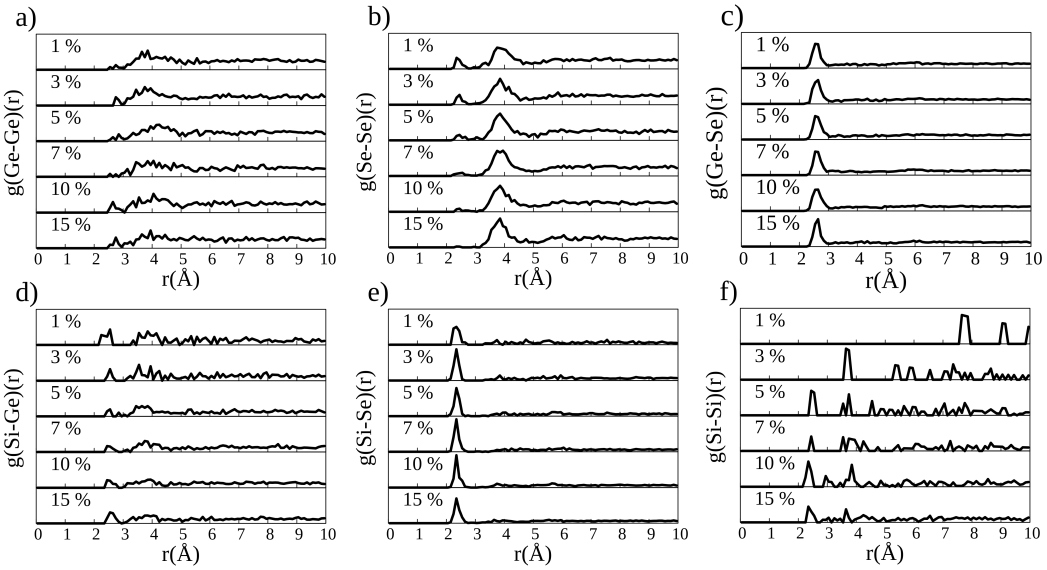

Figure 5.2: Partial radial distribution functions of the Si-doped a-$Ge_{0.4}Se_{0.6}$ for the pairs of a) Ge-Ge, b) Se-Se, c) Ge-Se, d) Si-Ge, e) Si-Se, and f) Si-Si.

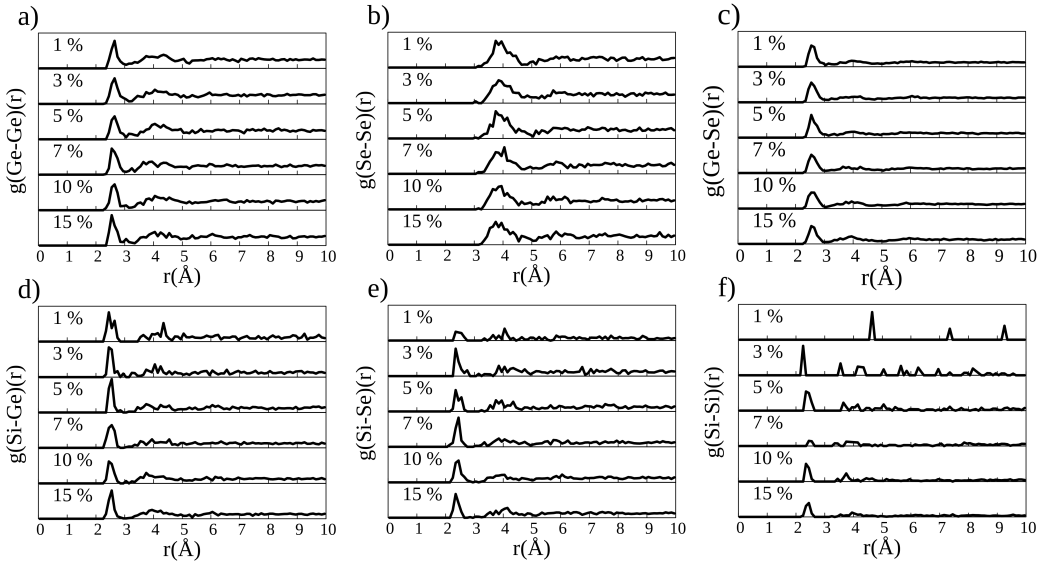

Figure 5.3: Partial radial distribution functions of the Si-doped a-$Ge_{0.6}Se_{0.4}$ for the pairs of a) Ge-Ge, b) Se-Se, c) Ge-Se, d) Si-Ge, e) Si-Se, and f) Si-Si.

ADF

Herein, we present the angle distribution function of the Si-doped a-$Ge_{0.5}Se_{0.5}$, a-$Ge_{0.4}Se_{0.6}$, and a-$Ge_{0.6}Se_{0.4}$. The angle distribution function gives us insight into the shape of the local cluster present in the amorphous structure. For example, a clearly defined peak at about 90°indicates the presence of octahedra, where 6 neighboring atoms surround each central atom. A peak around 109.5°indicates a predominance in the amorphous structure of tetrahedra where 4 neighboring atoms surround the central atom. Angles between $90° < \theta < 109.5°$ indicate trigonal pyramidal structural motifs in the amorphous network. A trigonal pyramidal structural motif is a molecular shape where a central atom is positioned at the apex of a pyramid, with three other atoms occupying the corners of a triangular base. This creates a structure with four atoms in total, where three are arranged in a plane, and one is above it.

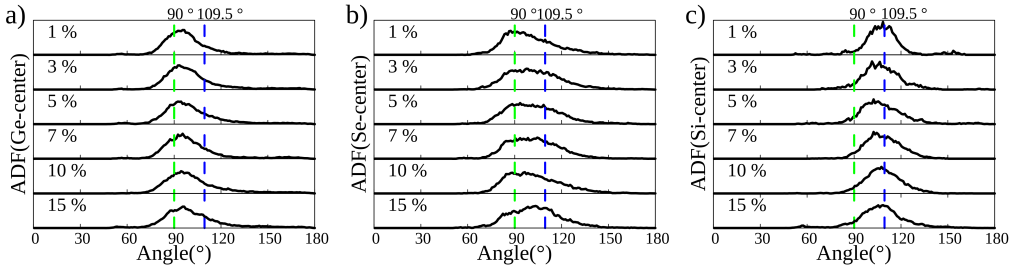

Figure 5.4: The angle distribution function of the Si-doped a-$Ge_{0.5}Se_{0.5}$: a) Ge-centered, b) Se-centered, and c) Si-centered. The vertical lines represent the well-known structural angles for the compounds, such as the octahedra, trigonal pyramidal, trigonal bipyramidal at 90°green dashed lines, and the tetrahedra at 109.5 °dashed blue lines.

Figures 5.4, 5.5, and 5.6 show the angle distribution functions of Si-doped a-Ge_xSe_{1-x}. Ge-centered ADF forms a more symmetrical bell shape at about 95° in both the stoichiometric and Se-rich samples. Coordination analysis of Ge atoms (see figures 5.8 and 5.7) reveals that Ge is primarily 3-fold coordinated in the Se-rich sample. Ge is 3- or 4-fold coordinated in the stoichiometric sample depending on the composition, suggesting an amorphous network defined by trigonal pyramidal structures with Ge atoms at the pyramid's apex. In the Ge-rich samples, the Ge-centered angle distribution function is broader compared to the a-$Ge_{0.5}Se_{0.5}$ and a-$Ge_{0.4}Se_{0.6}$ stoichiometries. It extends toward 109.5°, indicating a 4-fold tetrahedral geometry, as shown in the Ge coordination analysis in figure 5.9.

In the stoichiometric and Se-rich samples, the Se-centered ADF is broader than

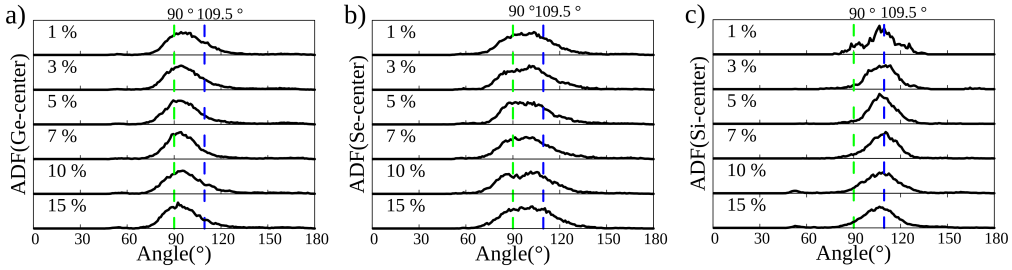

Figure 5.5: The angle distribution function of the Si-doped a-$Ge_{0.4}Se_{0.6}$: a) Ge-centered, b) Se-centered, and c) Si-centered.

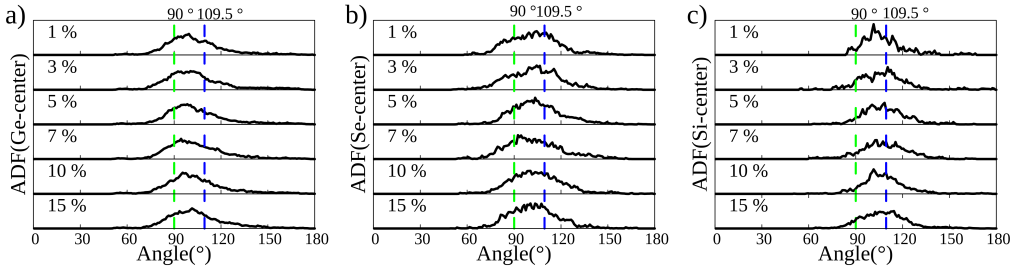

Figure 5.6: The angle distribution function of the Si-doped a-$Ge_{0.6}Se_{0.4}$: a) Ge-centered, b) Se-centered, and c) Si-centered.

the Ge- and the Si-centered ADFs, with a main peak at about 90 °at 1% of Si and shifting toward bigger angles as the Si content increases for the stoichiometric sample. In the stoichiometric and Se-rich samples, the Se-centered ADF is broader than the Ge—and Si-centered ADFs. Its main peak is around 90°at 1% Si, shifting toward larger angles as the Si content increases in the stoichiometric sample.

In the stoichiometric sample, the Si-centered ADF is at about 109.5°, indicating a tetrahedral structure with Si at the center. In the Se-rich sample, at 1% of Si, the Si-centered ADF shows two bumps: one near 90° and another around 109.5°, indicating an amorphous network predominantly composed of trigonal pyramidal and tetrahedral structural motifs, respectively, as suggested by the coordination analysis 5.7. As the Si concentration increases, we notice a shift in the ADF toward larger angles centered around 109.5°, indicative of a predominance of the 4-fold structural motif. This can be seen in the histogram in figure 5.8, where Si is mostly 4-fold coordinated. In Se-rich sample, at high Si concentrations, the Si-centered ADF shows highly strained angles between 40° and 60°.

As the Ge content increases, the Se- and Si- ADFs become broader. The Se-

centered ADF shows a larger distribution due to its high electronegativity. As we see in the coordination analysis (figure 5.9), Se is mainly 3-fold coordinated, with a high probability of finding an angle between $90° < \theta < 109.5°$ indicating an amorphous network where the Se atoms have predominantly trigonal pyramidal structural motifs. For the Si-ADF, the broadness is because more Se is being replaced by Si, which has a lower electronegativity, so the angle distribution tends to be broader. The Si-centered ADF has a peak at around 109.5°, indicative of a network made of Si-centered tetrahedral motifs as seen from the coordination analysis of Si in figure 5.9.

Coordination analysis

Figures 5.8, 5.7, and 5.9 show the coordination analysis of the Si-doped a-Ge_xSe_{1-x}. In the stoichiometric sample, Ge is predominantly 3- and 4-fold coordinated, with the relative proportions changing with the composition. As the Ge content increases, Ge becomes primarily 4-fold coordinated, whereas higher Se content favors 3-fold coordination. However, we notice a 2-fold coordinated Ge in all the stoichiometries, and there is almost no 3-fold coordinated Si. This is due to the inert pair effect whereby the s pair shell remains uninvolved in atomic bonding, leading to a divalent Ge. As we shall see, this divalent Ge caused localized states within the mobility band gap. In all the stoichiometry and samples, Se is mainly 3-fold coordinated, and Si is 4-fold coordinated. The more dopants adopt their normal lattice configurations, the more they act as defect compensators and tend to open the band gap. They are unfavored for glass formation. This can be seen from the 5.10 where Ge and Si have more of a 4-fold configuration, and the band gap tends to be close. This is crucial because the opening of the band gap is related to the value of the threshold voltage at which the resistance drops in the OTS material.

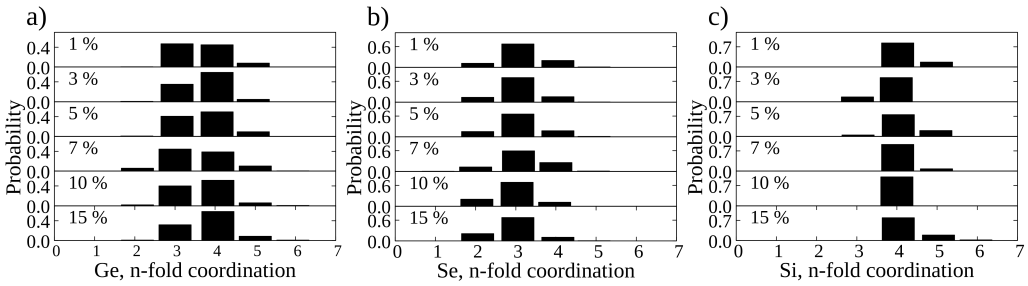

Figure 5.7: Coordination analysis of the Si-doped a-$Ge_{0.5}Se_{0.5}$: a) Ge coordination, b) Se coordination, and c) Si coordination.

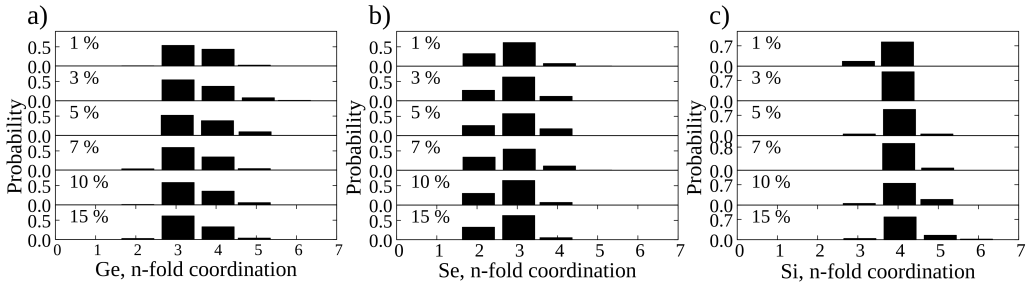

Figure 5.8: Coordination analysis of the Si-doped a-$Ge_{0.4}Se_{0.6}$: a) Ge coordination, b) Se coordination, and c) Si coordination.

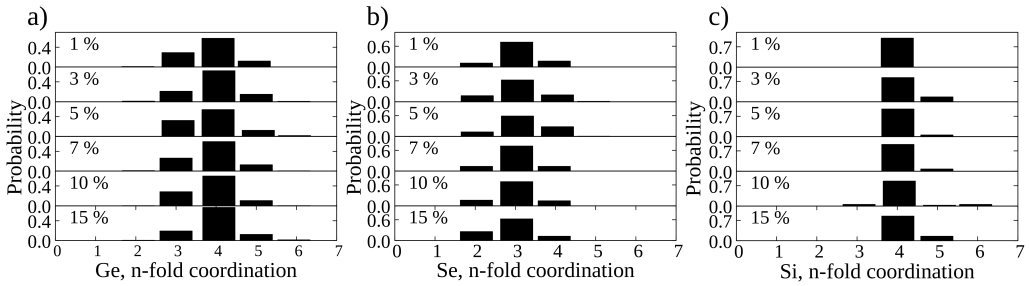

Figure 5.9: Coordination analysis of the Si-doped a-$Ge_{0.6}Se_{0.4}$: a) Ge coordination, b) Se coordination, and c) Si coordination.

5.2.2 Electronic properties

In this section, we discuss the electronic structures of the Si-doped a-Ge_xSe_{1-x}. We show the densities of states, which provide insights into how electrons are distributed across different energy levels, focusing on the energy range from $[-2\,\text{eV}, 2\,\text{eV}]$ relevant to this study and the conductivity. We also show the inverse participation ratio, which helps to quantify the degree of the localization of an electronic state, and we link the localized state to the structural environment.

In the previous chapter (4), the states within the energy range $[-2\,\text{eV}, 2\,\text{eV}]$ were analyzed to identify the structural motifs responsible for localized states. In undoped a-Ge_xSe_{1-x}, we found that Se-Se bonds, Se lone pairs (Se-LP), and Ge-centered tetrahedra gave rise to localized states. This remains true for doped amorphous chalcogenides; therefore, in this section, we focus on the localized states induced by the dopants or not found in the pristine a-Ge_xSe_{1-x}.

Figure 5.10 shows the electronic density of states (black curves) and the inverse participation ratio (red spikes) of the Si-doped panels a) a-$Ge_{0.4}Se_{0.6}$, b) a-$Ge_{0.5}Se_{0.5}$

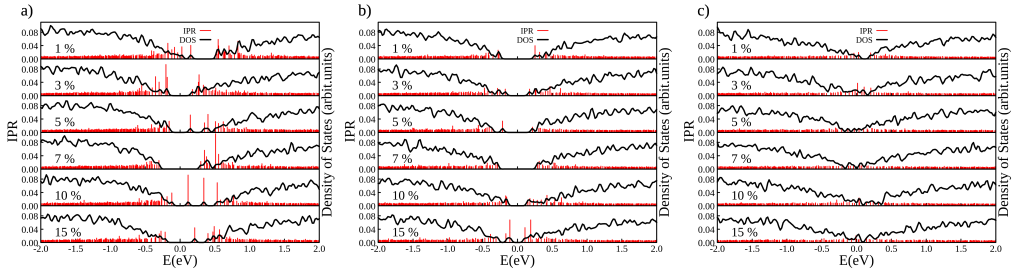

Figure 5.10: Density of states (black curve) and inverse participation ratio (red spikes) of the silicon-doped at 1, 3, 5, 7, 10 and 15 % a) a-$Ge_{0.4}Se_{0.6}$, a-$Ge_{0.5}Se_{0.5}$ and a-$Ge_{0.6}Se_{0.4}$

and c) a-$Ge_{0.6}Se_{0.4}$. For the a-$Ge_{0.4}Se_{0.6}$ sample doped at 1%, p-type conduction is observed, with the Fermi level lying in the valence band. However, the other samples of the same stoichiometry, as well as the a-$Ge_{0.5}Se_{0.5}$, display a mobility gap with a distinct spectral band gap. For the Ge-rich sample, no band gap is observed and all the samples show a metallic character.

Linking it to the coordination analysis, we can infer that the more the dopant atoms and Ge are 4-fold coordinated, the smaller the band gap will be. This is seen at 15% of Si-doped a-$Ge_{0.5}$ $Se_{0.5}$ and a-$Ge_{0.6}Se_{0.4}$, where the Si is up to 6-fold coordinated and has the highest probability of Ge being 4-fold coordinated. The band gap also appeared smaller at 3 % of doped a-$Ge_{0.5}Se_{0.5}$ and 10 % of Si, whose coordination analysis shows a higher fraction of Ge and/or Si being 4-fold coordinated. On the contrary, at 7 % of silicon, the spectral band gap is wider, and the percentage of the 4-fold coordinated structure is slightly smaller than that of the 3-fold coordinated. The same conclusion can be drawn for the a-$Ge_{0.4}Se_{0.6}$.

Figures 5.11, 5.12, and 5.13 show the structural motifs responsible for localized states within the band gap in Si-doped a-Ge_xSe_{1-x}. We observe defect states arising from the Si-Si bond (see figure 5.11) and the Si-Ge bond (figure 5.12). Figure 5.12 illustrates a localized state due to divalent Ge, which is prone to electron capture, a phenomenon also noted in amorphous germanium oxide by [BBP10]. Moreover, tetrahedrally-coordinated Si atoms (see figure 5.12) also give rise to a defect state.

Figure 5.13 illustrates a case of substitutional doping, where Si adopts a tetrahedral configuration. This dopant is positively charged, as revealed by the Bader analysis [HAJ06; San+07; TSH09], and the resulting localized state is located a few kT from the Fermi energy at 0.299 eV. Our results align with the work of Spear and co-workers [SL75], who found through dc conductivity measurements that, in case of substitutional doping, the Fermi level does not approach closer than 0.2–0.3 eV to the mobility edge. Since the Fermi level remains near the center of the band gap,

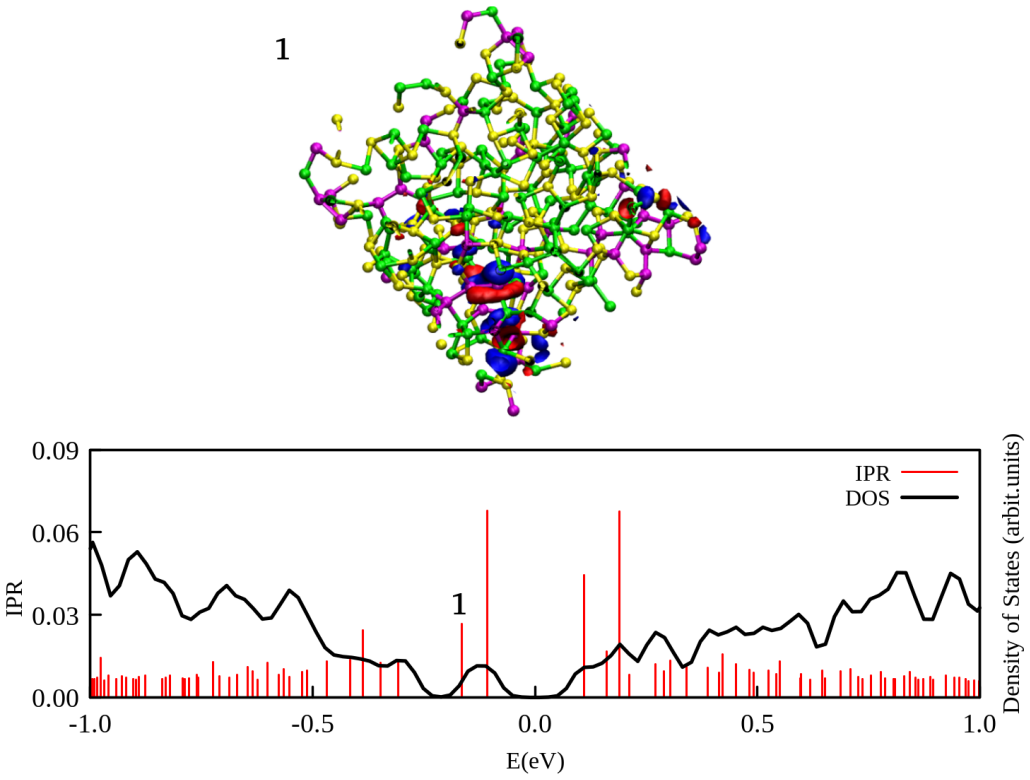

Figure 5.11: Top graph: single-particle wave function of the selected defect state in the mobility gap of the Si-doped a-$Ge_{0.5}Se_{0.5}$ at 15 %. The red and blue isosurfaces indicate the positive and the negative sign of the wave function, respectively. The green color represents the Ge atom, the yellow is the Se atom, and the purple is the Si atom. Bottom plot: DOS (black curve) and the IPR (red spike) of the sample. The localized state shown 1) is due to the Si-Si π bond.

similar to its intrinsic position in undoped materials, and is pinned between the valence band at -0.304 eV and the conduction band at 0.299 eV, we can infer that the positive charge on the donor state $|e|N_D^+$ is balanced by a negative charge in the acceptor state N_A, leading to a compensation ratio $K = 1$ $\left(K = \frac{N_A}{N_D}\right)$.

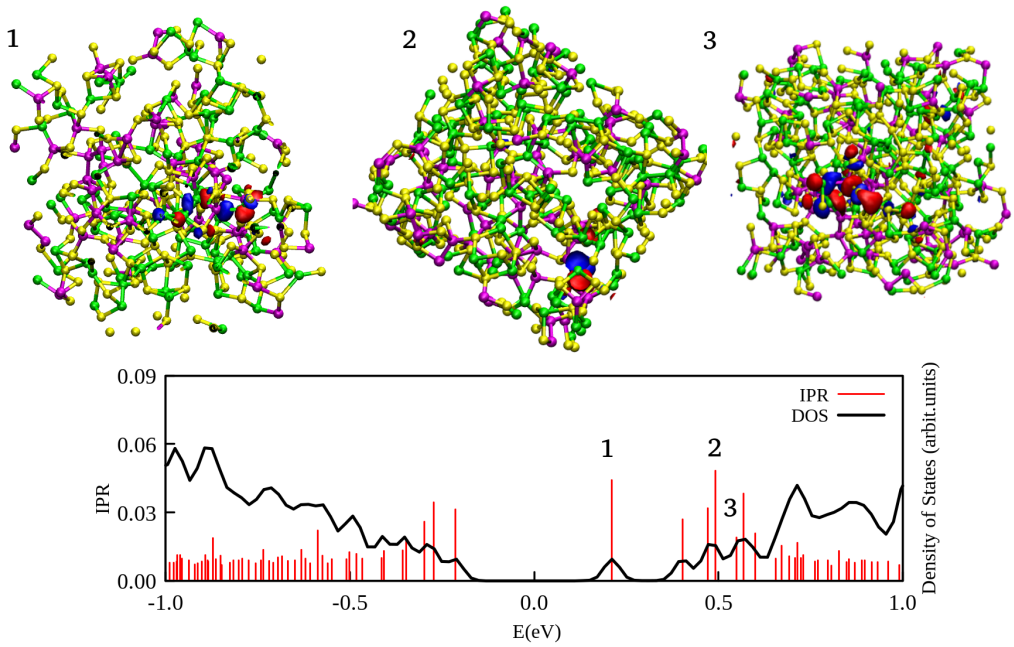

Figure 5.12: Top graph: single-particle wave functions of the selected defect states in the mobility gap of the Si-doped a-$Ge_{0.4}Se_{0.6}$ at 15 % of silicon. The red and blue isosurfaces indicate the positive and the negative sign of the wave function, respectively. Bottom plots: DOS (black curve) and the IPR (red spike) of the sample. The localized state is due to: 1) Si-Ge bond, 2) 2-fold Ge, 3) Si-centered tetrahedron.

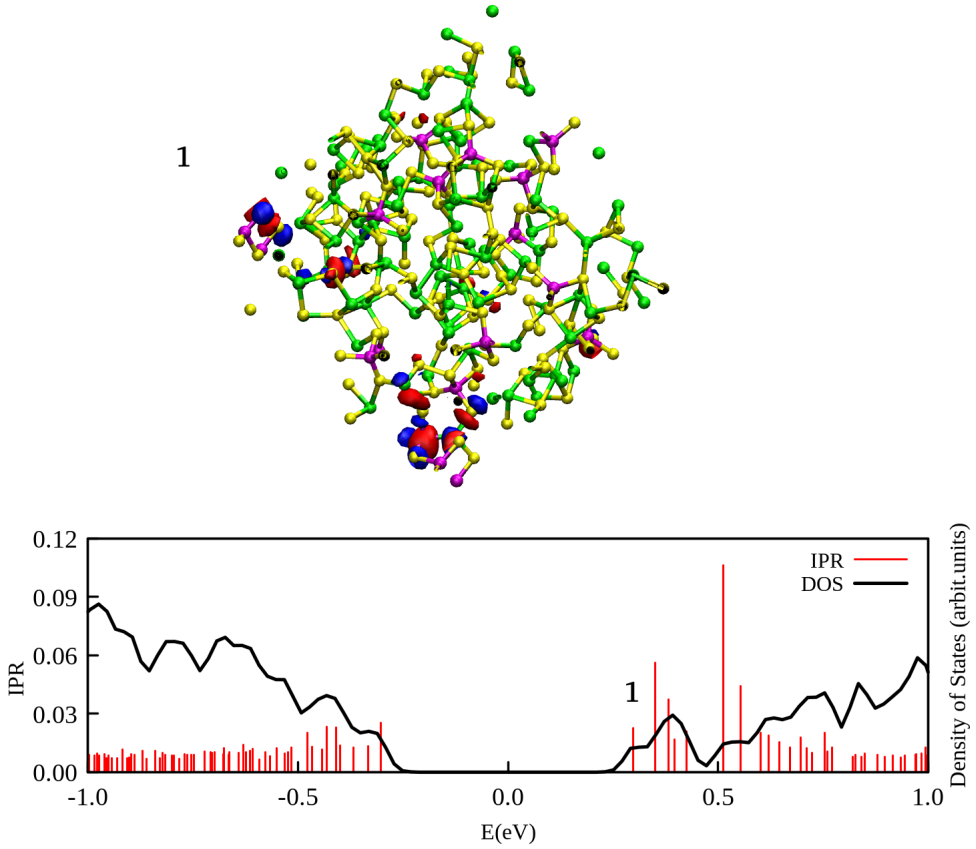

Figure 5.13: Top graph: single-particle wave functions of the selected defect state in the mobility gap of the Si-doped a-$Ge_{0.4}Se_{0.6}$ at 15 % of silicon. The red and blue isosurfaces indicate the positive and the negative sign of the wave function, respectively. Bottom plots: DOS (black curve) and the IPR (red spikes) of the sample. The localized state is due to: 1) Substitutional doping. The Si-centered tetrahedron is positively charged, as revealed by Bader charge analysis.

Summary

The RDF, ADF, and coordination analysis show the local order of the Si-doped a-Ge_xSe_{1-x} for different compositions.
The Ge-Se RDF has a well-defined first neighbor shell for all three stoichiometries. Additionally, a MRO can be seen in the Ge-rich sample. In the stoichiometric and Ge-rich samples, we observe distinct first-neighbor peaks and medium-range ordering in the Ge-Ge RDF. In contrast, the Se-rich samples show a trend of decreasing Se-Se bonding as Si concentration rises, replaced by Si-Se bonding. The Si-Si bonds appear only at higher concentrations in three stoichiometries aligning with a structural role similar to that of Ge.

The Ge-centered ADF results indicate the presence of tetrahedral and trigonal pyramidal configurations. In Ge-rich samples, tetrahedral structural motif increases due to increased Ge-Ge bonding. In contrast, Se-rich samples show more trigonal pyramidal structures for Ge and a more symmetric, narrow distribution of angles around 109.5°for the Si-centered ADF. This trend is likely influenced by the replacement of Se by Si, resulting in a broader angle distribution for Si-centered bonds in the Ge-rich samples.

The coordination analysis further highlights the impact of Si incorporation into the amorphous network. Se is predominantly 3-fold coordinated for all concentrations. Si preference for 4-fold coordination is consistent across all stoichiometries, while Ge is predominately 3-fold and 4-fold coordinated in all the compositions. Divalent Ge contributes to localized states within the mobility gap, which may affect electronic properties. Ultimately, the dopant configurations and network connectivity play a critical role in tuning the structural and electronic properties of Si-doped a-Ge_xSe_{1-x} amorphous materials, influencing their suitability for applications like Ovonic threshold switching (OTS), where band gap modulation is essential for device performance.

5.3 Pnictogen-doped a-Ge_xSe_{1-x}

5.3.1 Structural properties

RDF

Figures 5.14, 5.15, and 5.16 show the partial RDF for the pairs a) Ge-Ge, b) Se-Se, c) Ge-Se, d) P-Ge, e) P-Se, and f) P-P as the concentration of P increases. In the stoichiometric and Se-rich samples, the Ge-Ge homonuclear distances are mainly of the second neighbor shell with few Ge-Ge bonds formed. Increasing the Ge content leads to a well-defined Ge-Ge first neighbor shell in the a-$Ge_{0.6}Se_{0.4}$, and an MRO order that extends after 3 Å. Upon increasing the P content, the number of Ge-Ge bonds decreases. This indicates a network where Ge atoms are indirectly connected, with Se or P atoms likely serving as intermediaries.
In a-$Ge_{0.5}Se_{0.5}$ and a-$Ge_{0.6}Se_{0.4}$, the g(Se-Se)(r) shows no Se-Se bonds in all the P-doped concentrations. In contrast, in a-$Ge_{0.4}Se_{0.6}$, As seen in chapter 4, the Se-Se bonds are present in the undoped structure, indicating that the higher Se concentration allows Se atoms to bond directly. However, as P is added, the number of Se-Se bonds decreases. The decreasing proportion of Se-Se bonds with increasing P content implies that P integrates into the network by breaking Se-Se first coordination shell and forming P-Se, Ge-P or P-P bonds instead.

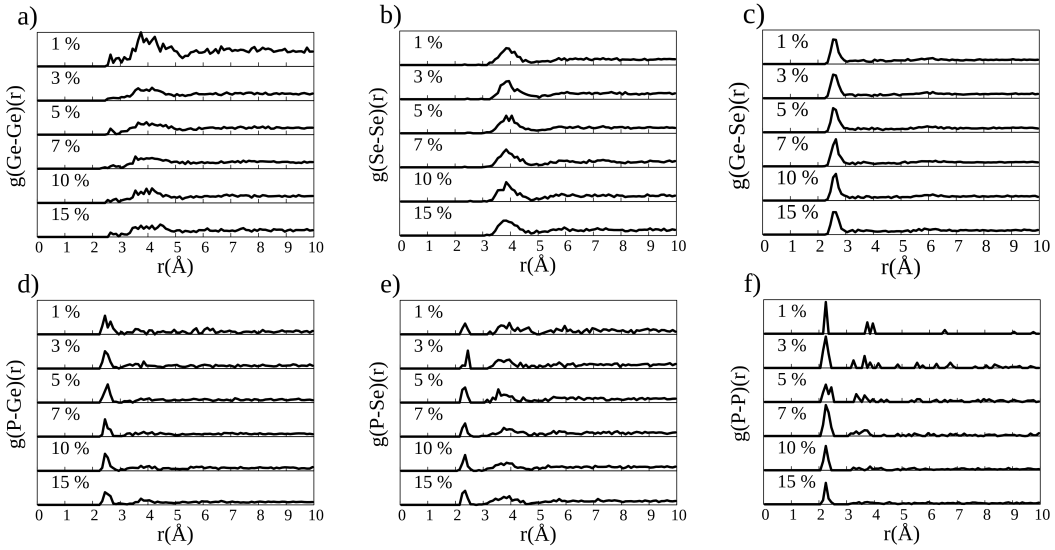

Figure 5.14: Partial pair correlation function of the P-doped a-$Ge_{0.5}Se_{0.5}$ for the pairs of a) Ge-Ge, b) Se-Se, c) Ge-Se, d) P-Se, e) P-Ge, f) P-P

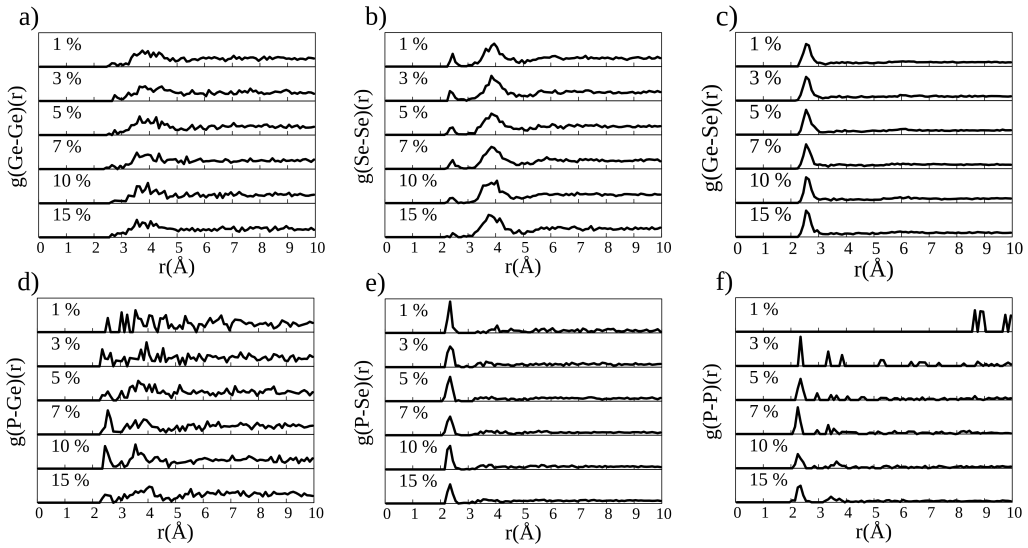

Figure 5.15: Partial radial distribution function of the P-doped a-$Ge_{0.4}Se_{0.6}$ for the pairs of a) Ge-Ge, b) Se-Se, c) Ge-Se, d) P-Se, e) P-Ge, f) P-P

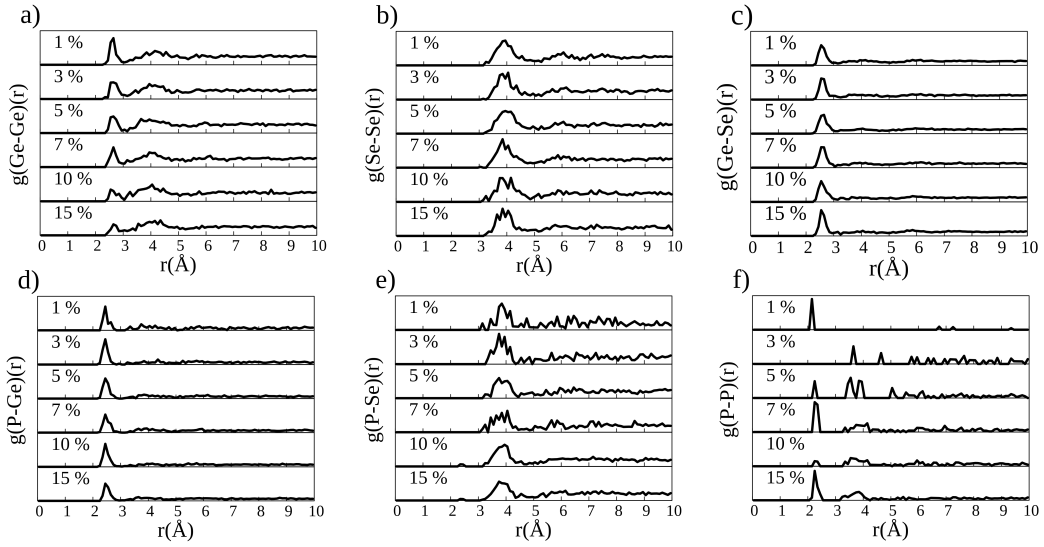

Figure 5.16: Partial radial distribution function of the P-doped a-$Ge_{0.6}Se_{0.4}$ for the pairs of a) Ge-Ge, b) Se-Se, c) Ge-Se, d) P-Se, e) P-Ge, f) P-P

We observe the first neighbor shells in the Ge-P RDFs for all the dopant concentrations in all three stoichiometries. In the stoichiometric sample, the g(P-Se)(r)

distinctively exhibits the first and second neighbor shells. This suggests that in the stoichiometric composition, P atoms are well-coordinated with Se atoms, with clear and distinguishable distances to the nearest (first shell) and next-nearest (second shell) Se neighbors. As the Se content increases, the second neighbor shell becomes less defined. This suggests that the distances between P and the second nearest Se atoms become more diffuse in the Se-rich sample, implying that the distances involving P and Se vary considerably across the structure. Meanwhile, the second neighbor shell is the primary distance in the Ge-rich sample; however, at a higher concentration of P, few P-Se bonds are formed.
In all the stoichiometries, adding P atoms to the amorphous network does not significantly change the Ge-Ge, Ge-Se, and Se-Se partial RDF. Therefore, P interacts similarly with Se and Ge. The P-P bond length is 2.25 ± 0.05 Å in all the stoichiometries, close to the value of 2.24 Å P-P bond length in elemental P, [Sin+17]. However, there is no P-P bond in the Ge-rich at 3 % of P and at 1 % of P in the Se-rich.

Figures 5.17, 5.18, and 5.19 show the partial RDFs of As-doped a-Ge_xSe_{1-x}. In the stoichiometric and the Se-rich samples, the Ge-Ge distance is of the second neighbor shell, with few Ge-Ge bonds forming. In contrast, in the Ge-rich samples, the Ge-Ge RDFs exhibit Ge-Ge bonds as the primary distance at lower dopant concentrations. This trend is similar to what we observe in the case of the P-doped a-Ge_xSe_{1-x}.

For all three stoichiometries, the Se-Se RDF remained relatively unchanged for all the dopant concentrations, with its main peak around 4 Å. However, in a-$Ge_{0.4}Se_{0.6}$, the proportion of Se-Se bonds diminishes as the As concentration increases. This observation is also consistent with what we see in the case of the P-doped a-Ge_xSe_{1-x}

The Ge-Se RDF exhibited well-defined first neighbor shells in all stoichiometries, with a peak at about 2.5 Å.

As in the case of the P-doped a-Ge_xSe_{1-x}, introducing As into the network does not significantly alter the Ge-Ge, Se-Se, and Ge-Se RDFs for the stoichiometric and the Se-rich samples. In the Ge-rich sample, the introduction of As dopants changes the first-neighbor shell in the Ge-Ge RDFs, while the Se-Se and Ge-Se remain almost unaltered. The latter implies that As does not interact significantly with Se or disrupt the Ge-Se network as much as it does with the Ge-Ge network. The Se atoms may be more stable in their coordination environment, unaffected by the dopant.

In the stoichiometric sample, the g(As-Ge)(r), g(As-Se)(r), and g(As-As)(r) show a clear separation between the first and second neighbor shells. This suggests that in the stoichiometric sample, the atomic distances (As-Ge, As-Se, As-As) are relatively well-defined. Only the As-Se RDFs remain well-defined across all dopant concentrations as the Se content increases, indicating a clear preference for As to bond with Se rather than with itself or Ge. Conversely, increasing Ge content makes As-Ge distance the primary bond among the three.

The typical As-As bond length in bulk gray As is 2.55 Å [Liu+16], which aligns with the 2.55 ± 0.05 Å As-As bond length we found in the stoichiometric compound, as well as in samples with 10% As in the Ge-rich and 5 and 10% As in the Se-rich compositions. The typical As-As bond length in elemental As crystal in the cubic $P_{m\bar{3}m}$ space group is 2.70 Å, closely matching the 2.75 ± 0.05 Å bond length found at 7 and 15% As in the Ge-rich samples and the Se-rich sample with 15% As.

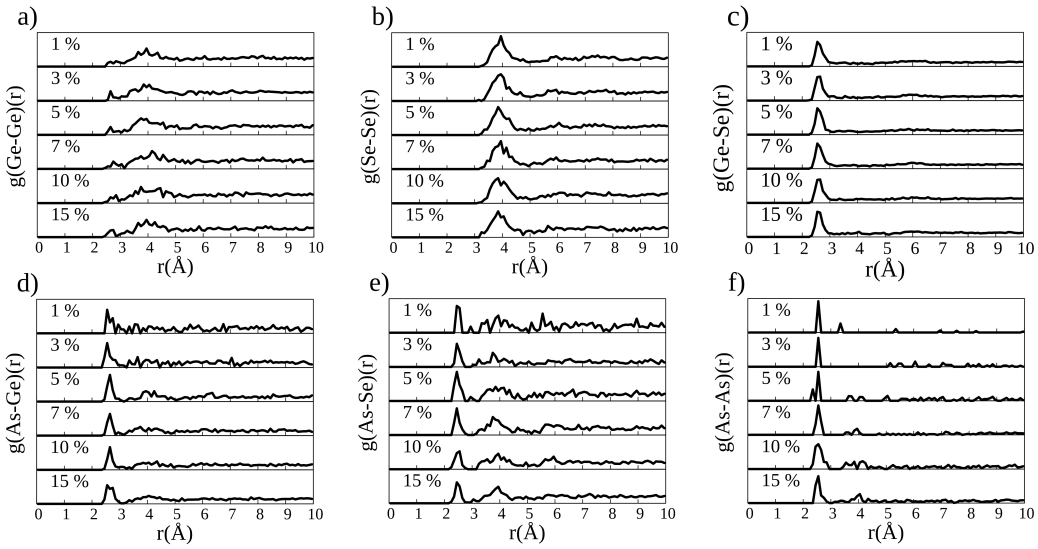

Figure 5.17: RDF of the As-doped a-$Ge_{0.5}Se_{0.5}$ for the pairs of a) Ge-Ge, b) Se-Se, c Ge-Se, d) As-Se, e) As-Ge, f) As-As

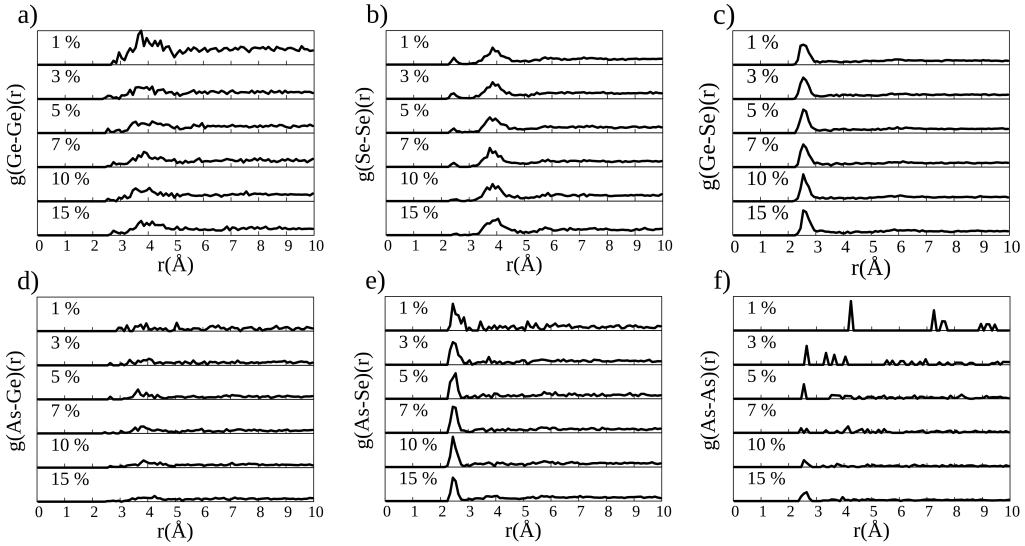

Figure 5.18: RDF of the As-doped a-$Ge_{0.4}Se_{0.6}$ for the pairs of a) Ge-Ge, b) Se-Se, c Ge-Se, d) As-Se, e) As-Ge, f) As-As

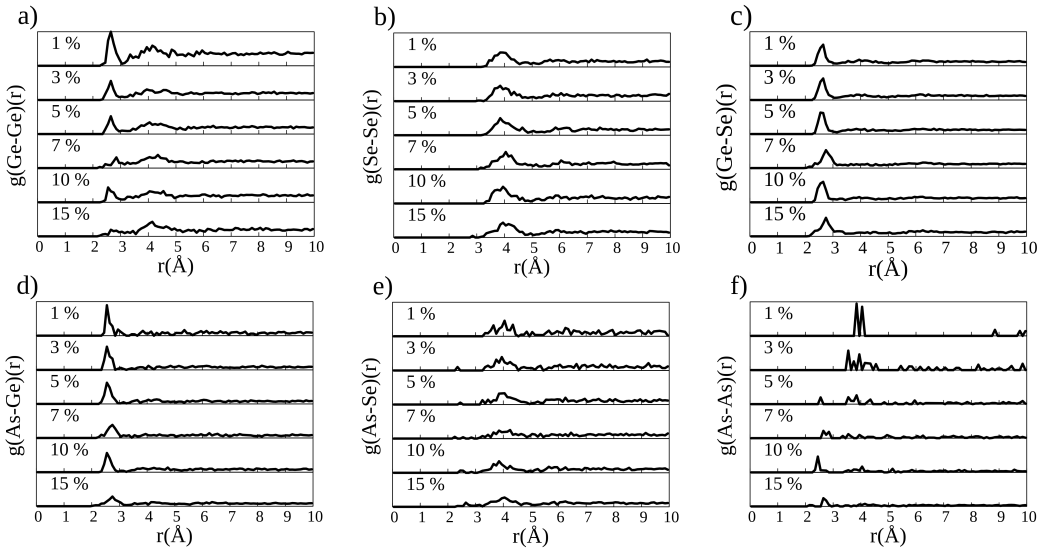

Figure 5.19: RDF of the As-doped a-$Ge_{0.6}Se_{0.4}$ for the pairs of a) Ge-Ge, b) Se-Se, c Ge-Se, d) As-Se, e) As-Ge, f) As-As

ADF

Figures 5.20, 5.21 , and 5.22 show the bond angles distribution of P-doped a-Ge_xSe_{1-x}. The Ge-centered ADF shows a more symmetric bell-shaped center at about an angle comprised [90°, 95°] indicative of a trigonal pyramidal structure in the three stoichiometries. The Se-centered ADF shows a broader distribution. It forms a plateau from 90 and 109 °, indicative of the trigonal pyramidal structure with the angle at about 90°and the presence of tetrahedral Se, respectively. In the a-$Ge_{0.4}Se_{0.6}$ for the Se-centered ADF, two main angles or a plateau can be observed depending on the P concentrations 90°and 104.5 °.

For the a-$Ge_{0.5}Se_{0.5}$ and a-$Ge_{0.6}Se_{0.4}$, the P-centered ADF shows a distribution more centered at about 104 -109 °, as expected for a tetrahedral network with a minimal number of coordination defects, which reflects the predominance of a 4-fold environment as confirmed by figures 5.26 and 5.28. In the a-$Ge_{0.4}Se_{0.6}$, the P-centered ADF is symmetrical about [104°,107°], slightly shifted to the left in comparison to the a-$Ge_{0.5}Se_{0.5}$ or a-$Ge_{0.6}Se_{0.4}$ stoichiometries. In the Se-rich sample, adding Se, a more electronegative element, results in a smaller P bond angle. The less electronegative the central atom is compared to the ligand atom, Se, the smaller the ADF. This is in contrast to cases where Se is the central atom, whose electronegativity is higher than that of the ligand atoms, Ge and P.

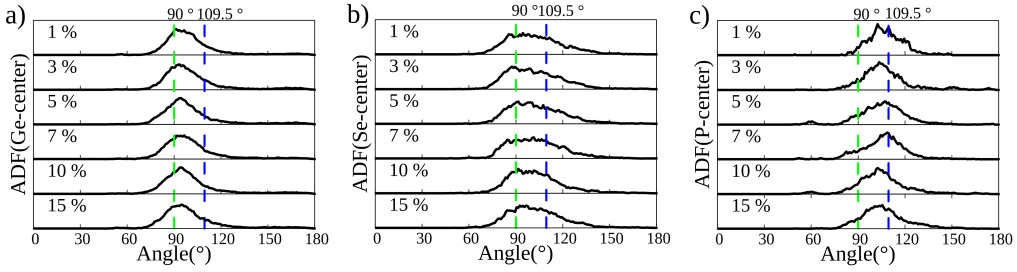

Figure 5.20: ADF for P-doped a-$Ge_{0.5}Se_{0.5}$: a) Ge-center, b) Se-center, c) P-center. The vertical lines represent the well-known structural angles for the compounds, such as the octahedra, trigonal pyramidal, trigonal bipyramidal at 90°green dashed lines, and the tetrahedra at 109.5 °dashed blue lines.

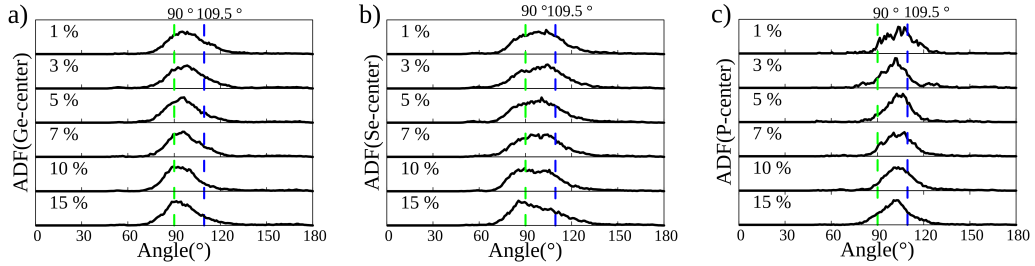

Figure 5.21: Angle distribution function for P-doped a-$Ge_{0.4}Se_{0.6}$: a) Ge-center, b) Se-center, c) P-center. The vertical lines represent the well-known angles for structural motifs, such as the octahedra, trigonal pyramidal, trigonal bipyramidal at 90°green dashed line, and the tetrahedra at 109.5 °dashed blue line.

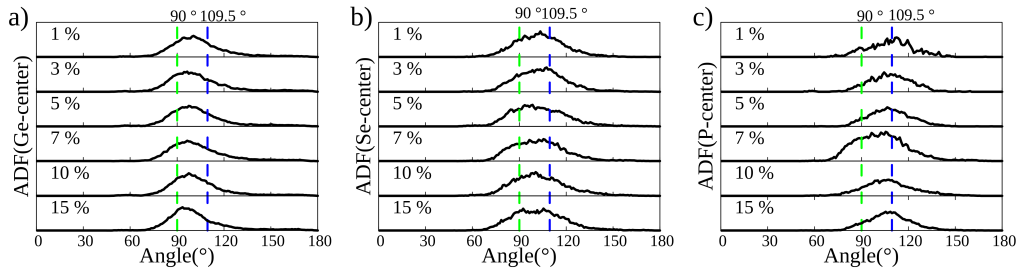

Figure 5.22: ADF for P-doped a-$Ge_{0.6}Se_{0.4}$: a) Ge-center, b) Se-center, c) P-center. The vertical lines represent the well-known angles for structural motifs, such as the octahedra, trigonal pyramidal, trigonal bipyramidal at 90°(green dashed line), and the tetrahedra at 109.5 °(dashed blue line).

Figures 5.23, 5.24, and 5.25 show the ADF for a-$Ge_{0.5}Se_{0.5}$, a-$Ge_{0.4}Se_{0.6}$, and a-$Ge_{0.6}Se_{0.4}$ respectively. The Ge-centered ADF exhibits a symmetrical bell shape around 97 °, consistent with [Gu+22], across all three stoichiometries. Similar to the P-doped a-Ge_xSe_{1-x}, the Ge-centered ADF in the a-$Ge_{0.6}Se_{0.4}$ stoichiometry is broader compared to the stoichiometric and Se-rich samples. This broadening is attributed to As (with an electronegativity of 2.0) replacing the more electronegative Se (electronegativity 2.4).

For the a-$Ge_{0.5}Se_{0.5}$, the Se-centered ADFs at low As content are centered around 90°, with a shoulder at approximately 109°, indicating the predominance of trigonal pyramidal and tetrahedral structural motifs in the amorphous network. As the Ge content increases, the Se-centered ADFs reveal two distinct peaks: one around 90° and another around 109.5° depending on the As content.

Generally, the As-centered ADFs have prominent peaks at about 97° in both a-$Ge_{0.5}Se_{0.5}$ and a-$Ge_{0.4}Se_{0.6}$. However, at 10% of As, the main is shifted toward 109.5°. As the Ge content increases, the As-centered ADF becomes broader, spreading over several angles, with a notable bump at approximately 170° at 1%, suggesting a flat angle characteristic of a trigonal bipyramidal structure for pentacoordinated As (see Figure 5.31). As the Arsenic concentration increases, the As-centered ADFs shift toward larger angles and tend to be symmetric around angles within the range of [104°, 109.5°].

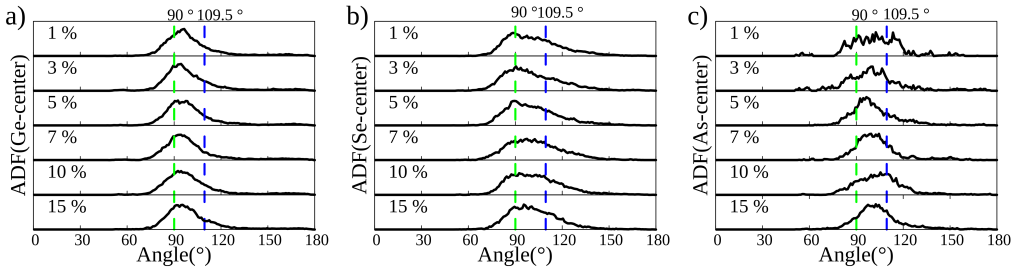

Figure 5.23: ADF for As-doped a-$Ge_{0.5}Se_{0.5}$. The vertical lines represent the well-known angles for structural motifs, such as the octahedra, trigonal pyramidal, trigonal bipyramidal at 90°(green dashed line), and the tetrahedra at 109.5 °(dashed blue line).

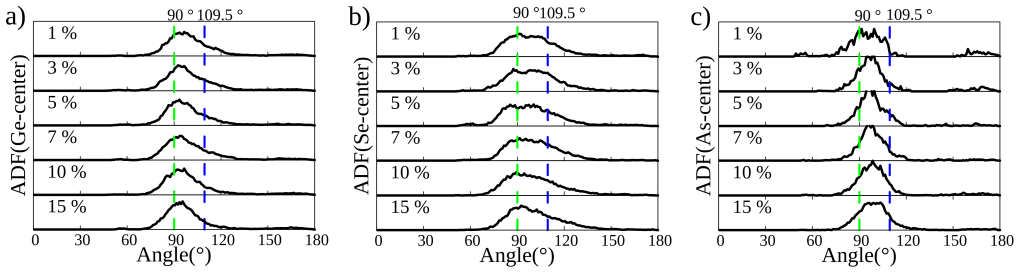

Figure 5.24: ADF for As-doped a-$Ge_{0.4}Se_{0.6}$. The vertical lines represent the well-known angles for structural motifs, such as the octahedra, trigonal pyramidal, trigonal bipyramidal at 90°(green dashed line), and the tetrahedra at 109.5 °(dashed blue line).

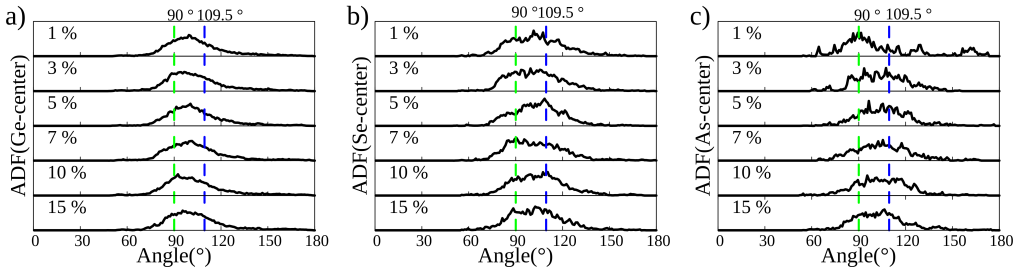

Figure 5.25: ADF for As-doped a-$Ge_{0.6}Se_{0.4}$: the vertical lines represent the well-known angles for structural motifs, such as the octahedral, trigonal pyramidal, and trigonal bipyramidal structures at 90°(green dashed line), and the tetrahedral structure at 109.5°(blue dashed line).

Coordination analysis

Figures 5.26, 5.27, and 5.28 show Ge, Se, and P coordination analysis. In the a-$Ge_{0.5}Se_{0.5}$ stoichiometry, Ge is primarily 3-fold coordinated. However, we observe an increase in Ge's coordination number, reaching up to 6-fold, starting at 7% and up to 15%. Specifically, one atom is hexacoordinated at 7% and 15%, and two at 10%.

In a-$Ge_{0.4}Se_{0.6}$, Ge is also mostly 3-fold coordinated, with one Ge atom hexacoordinated at 15%. This high coordination number is thought to strengthen the amorphous network, delaying crystallization [Gu+22; LE11]. In contrast, in the a-$Ge_{0.6}Se_{0.4}$ stoichiometry, Ge is primarily 4-fold coordinated, with hexacoordination occurring at low concentrations (3% and 5%).

In all stoichiometries, Se is predominantly 3-fold coordinated. In the stoichiometric and Ge-rich samples, P is mostly 4-fold coordinated, reaching 6-fold only at 15% in a-$Ge_{0.5}Se_{0.5}$. The higher proportion of 4-fold coordinated P in the stoichiometric and Ge-rich samples suggests substitutional doping, unlike in the Se-rich sample, where P is mostly 3-fold coordinated and no hexacoordinated P atoms are observed. This behavior can be understood from the RDF analysis (see figure 5.15), as P tends to bond more with Se in a-$Ge_{0.4}Se_{0.6}$ than with Ge.

In the Se-rich sample, P, being predominantly 3-fold coordinated, may act as a defect compensator within the amorphous network, widening the band gap and accelerating crystallization.

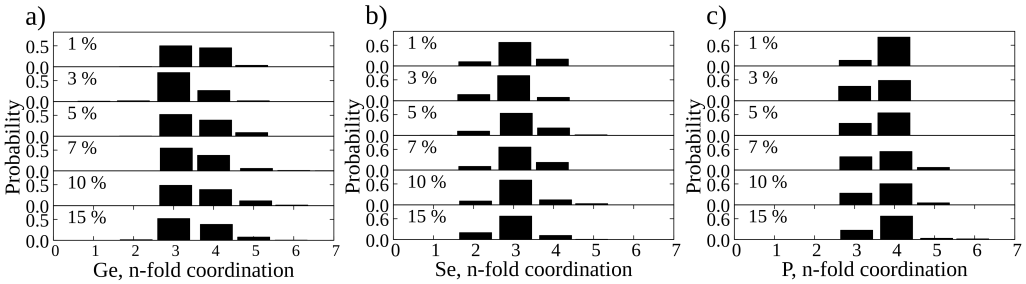

Figure 5.26: Coordination analysis for P-doped a-$Ge_{0.5}Se_{0.5}$: the histograms report the number of atoms of a specific species in a given coordination.

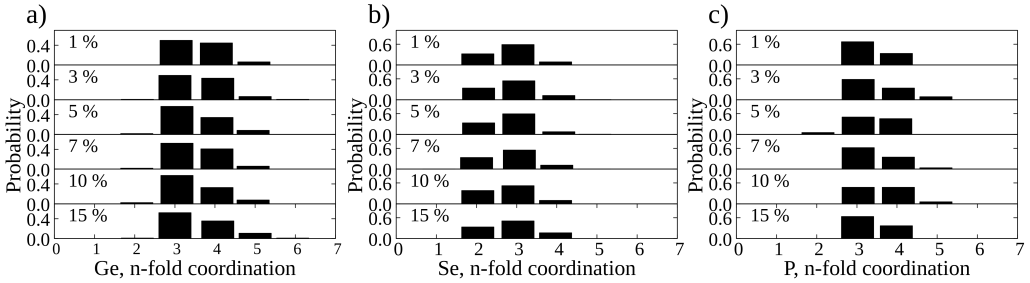

Figure 5.27: Coordination analysis for P-doped a-$Ge_{0.4}Se_{0.6}$: the histograms report the number of atoms of a specific species in a given coordination.

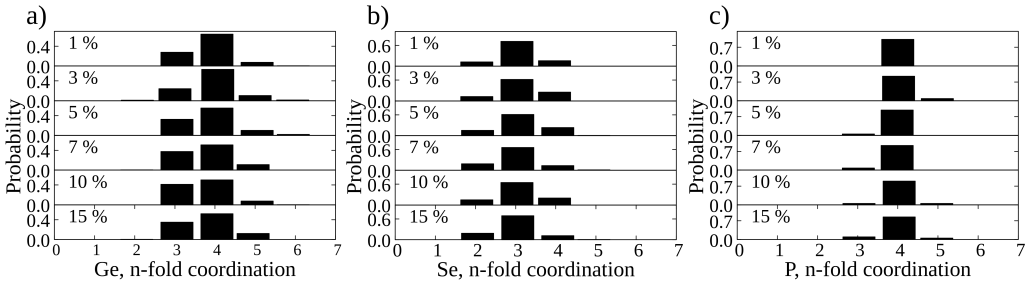

Figure 5.28: Coordination analysis for P-doped a-$Ge_{0.6}Se_{0.4}$: the histograms report the number of atoms of a specific species in a given coordination.

Figures 5.29, 5.30, and 5.31 show Ge, Se, and As coordination analysis as the As concentration increases. In both the a-$Ge_{0.5}Se_{0.5}$ and Se-rich stoichiometries, Ge is primarily 3-fold and 4-fold coordinated, while in the a-$Ge_{0.6}Se_{0.4}$ stoichiometry, Ge is predominantly 4-fold coordinated. Se, across all concentrations, remains mostly 3-fold coordinated.

In a-$Ge_{0.5}Se_{0.5}$, As is primarily 3-fold and 4-fold coordinated. In the Se-rich sample, As is mainly 3-fold coordinated, whereas in the Ge-rich sample, As is predominantly 4-fold coordinated except at 1% As concentration, where it is primarily 5-fold coordinated.

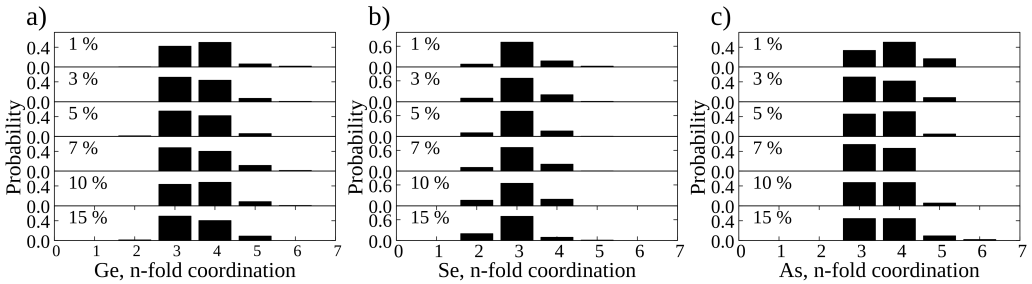

Figure 5.29: Coordination analysis for As-doped a-$Ge_{0.5}Se_{0.5}$: the histograms report the number of atoms of a specific species in a given coordination.

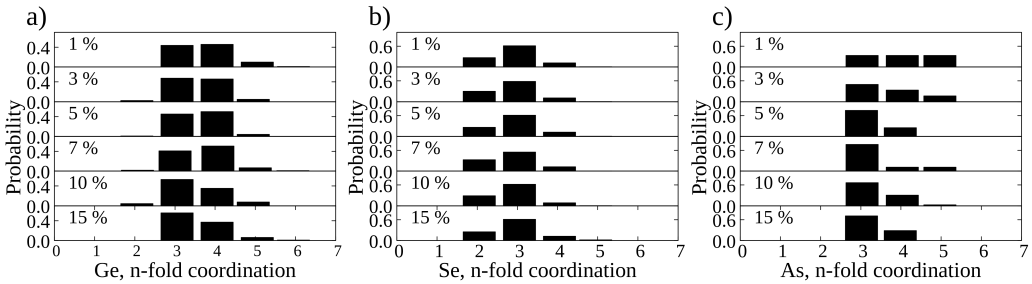

Figure 5.30: Coordination analysis for for As-doped a-$Ge_{0.4}Se_{0.6}$: the histograms report the number of atoms of a specific species in a given coordination.

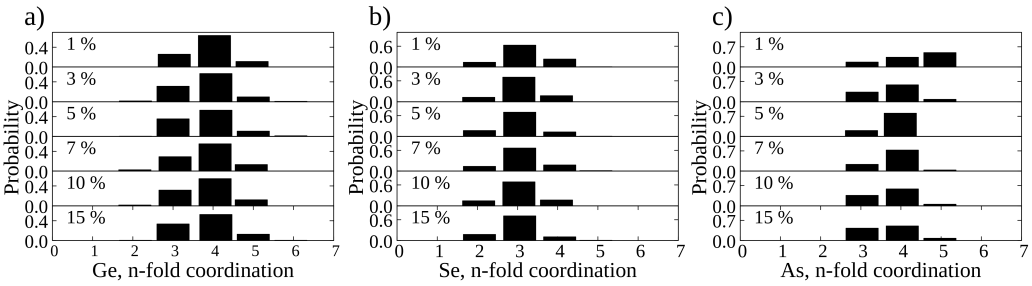

Figure 5.31: Coordination analysis for As-doped a-$Ge_{0.6}Se_{0.4}$: the histograms report the number of atoms of a specific species in a given coordination.

5.3.2 Electronic properties

In this section, we will show the DOS and IPRs of each P- and As-doped a-Ge_xSe_{1-x}, respectively. Adding pnictogen atoms in the amorphous network at different concentrations can lead to various electronic properties. In its normal lattice configuration, a pnictogen atom uses its 3 p-orbitals (P_3^0 configuration) for bonding. Since P and As atoms are common n-type dopeants for a-Ge and p-type dopeants for a-Se, we analyze the possible structural origin localized state arising from their

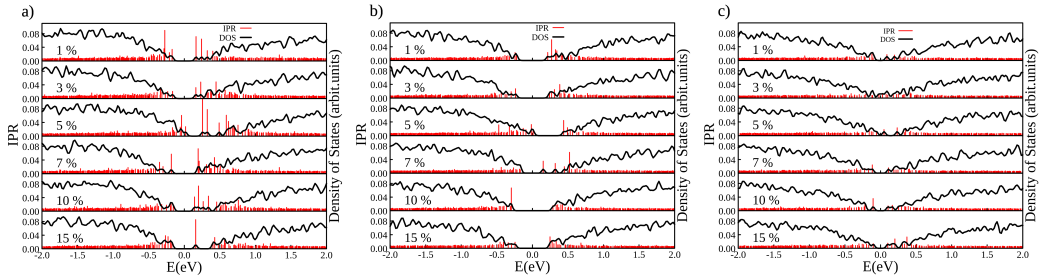

Figure 5.32: Density of states and inverse participation ratio of the P-doped at 1, 3, 5, 7, 10, and 15 % a) a-$Ge_{0.4}Se_{0.6}$, a-$Ge_{0.5}Se_{0.5}$ and a-$Ge_{0.6}Se_{0.4}$

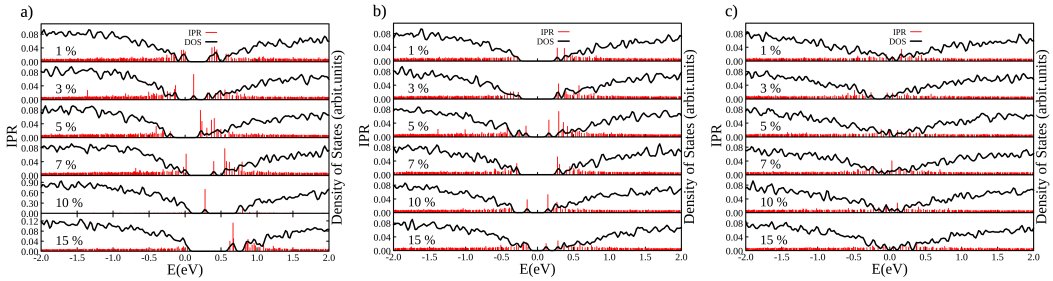

Figure 5.33: Density of states and inverse participation ratio of the As-doped at 1, 3, 5, 7, 10, and 15 % a) a-$Ge_{0.4}Se_{0.6}$, a-$Ge_{0.5}Se_{0.5}$ and a-$Ge_{0.6}Se_{0.4}$

Figures 5.32 and 5.33 show the DOS (black curves) and the inverse participation ratios (red spikes) of the P- and As-doped a-Ge_xSe_{1-x}. Panels a) represent the pnictogen doped a-$Ge_{0.4}Se_{0.6}$, b) the pnictogen doped a-$Ge_{0.5}Se_{0.5}$ and c) the pnictogen doped a-$Ge_{0.6}Se_{0.4}$.

Incorporating pnictogen atoms appear to produce larger densities of localized states at the edge of the conduction band rather than the valence band see figure 5.32 panel a) for the P-doped a-$Ge_{0.4}Se_{0.6}$ at 3, 5, 7 %, and panel b) for the P-doped a-$Ge_{0.5}Se_{0.5}$ at 5 and 7 % to name only those. The addition of the pnictogen atoms to the amorphous network could also result in the creation of donor states below

the conduction band see figure 5.33 panel b) for the As-doped a-$Ge_{0.5}Se_{0.5}$ at 10 % and panel c) As-doped a-$Ge_{0.6}Se_{0.4}$ at 3 % and some acceptor states responsible for the hole conduction just above the valence band see figures 5.32 panel a) for the P-doped a-$Ge_{0.4}Se_{0.6}$ at 5 %, panel b) for the P-doped a-$Ge_{0.5}Se_{0.5}$ at 5 %, figure 5.33 panel a) for the As-doped a-$Ge_{0.4}Se_{0.6}$ at 1, 7, 10 and 15 %.

At 5 % of P in the a-$Ge_{0.4}Se_{0.6}$ sample, the acceptor state is due to Se LP. Whereas for 7 % of the As-doped Se-rich sample, the acceptor state is due to tetrahedra. When As or P replaces more Ge, we observe an n-type semiconduction. This is seen at 3 % of As in the Ge-rich stoichiometry and in the As-doped a-$Ge_{0.5}Se_{0.5}$ stoichiometry at 10 %.

Besides the aforementioned shallow-level traps (near the band edge), we noticed deep-level traps (farther from the band edge) for P-doped a-$Ge_{0.4}Se_{0.6}$ at 15 % see figure 5.32 panel a) and As-doped a-$Ge_{0.5}Se_{0.5}$ at 15 % see figure 5.33 panel b.

As in the undoped cases, in some pnictogen-doped samples, the Fermi level remains at its intrinsic position in the middle of the band gap. This is observed at 1, 3, and 7 % of the P-doped a-$Ge_{0.4}Se_{0.6}$, at 1, 3, 10 % a-$Ge_{0.5}Se_{0.5}$ P, at 5 % of As-doped a-$Ge_{0.4}Se_{0.6}$, and at 1, 3, 5 and 7 % of the As-doped a-$Ge_{0.5}Se_{0.5}$. This implies that the concentration of the donor is equal to the concentration of the acceptor.

In the P-doped a-$Ge_{0.5}Se_{0.5}$, 2-fold coordinated Ge atoms, as shown in Figure 5.26, give rise to localized states in the valence and conduction bands. For instance, at 1% P doping, two states at the edges of the conduction band are due to 2-fold Ge. Similarly, at 3% and 15%, two localized states in the conduction band also originate from 2-fold Ge atoms.

In the As-doped sample, 2-fold Ge atoms also contribute to localized states in the conduction band. For example, at 1% As , 2-fold Ge creates states in the conduction band, with a similar effect observed at 5% and 15% As doping. Divalent Ge, which is prone to electron capture, has been observed in both this work and in amorphous germanium oxide [BBP10].

In the As and P-doped Se-rich samples, the pnictogen atoms are primarily 3-fold coordinated, which implies that they primarily entered the amorphous network in their normal lattice configuration P_3^0 and will not act as a dopant but as a network relaxer and defect compensator to passivate dangling bond and tend to open up the band gap, which is the case for 1, 3, 7 and 15 % of the P for the Se-rich samples in agreement with the result found by [SN91] in the case of the P-doped a-Si:H. For the other 2 stoichiometries, the P entered the amorphous network primarily as being 4-fold coordinated. Since P exhibits higher 4-fold coordination compared to As—where the 3- and 4-fold coordination are more balanced in the stoichiometric sample—the band gap of P-doped a-$Ge_{0.5}Se_{0.5}$ is smaller than that of As-doped

a-$Ge_{0.5}Se_{0.5}$. The proportion of 4-fold P and 3-fold P are adjusted to achieve overall charge neutrality; this has been checked by computing the Bader charges.

At 5% of P in the stoichiometric sample, the Fermi level is located in the valence band, indicating a significant population of holes. The position of the Fermi level is controlled by the dopant, suggesting p-type conduction (see figure 5.39). The state at the Fermi level originates from a P-Ge bond, where the P atom involved in forming the bond is 3-fold coordinated (bonded to two Se atoms and one Ge atom). This observation is noteworthy because P is typically regarded as a donor dopant in semiconductors when it replaces Ge, which has four valence electrons. Phosphorus has five electrons in its outer shell, one of which is available for conduction. However, in our case, the P remains in a normal lattice configuration, creating excess holes and transforming the material into a p-type semiconductor due to the abundance of charged holes. P acts as a dopant within the Se network in this scenario, clarifying the p-type behavior. Phosphorus has five valence electrons, while selenium (Se) has six. This discrepancy means that P has one fewer electron than Se, creating excess holes.

The key to the p-type conduction in Se doped with phosphorus lies in introducing an energy level (the acceptor level) within the band gap of Se. This acceptor level is closer to the valence band, where electrons can occupy energy states. If a significant quantity of defects were present, the Fermi level would not be easily shifted by doping.

At 10% As dopant in the stoichiometric sample (see figure 5.34), the localized states arise from the As-Ge bond in the valence band, while a tetrahedral configuration is observed in the conduction band. This leads to n-type semiconductor behavior, characterized by a built-in auto-compensation defect. The excess electrons introduced by the dopant condense above the Fermi level (case 2), raising it to a new position and effectively unpinning it toward the CB. The negative charge in the gap (case 1) compensates for the positive charge, maintaining charge neutrality in the system.

At 15% of P-doped a-$Ge_{0.5}Se_{0.5}$, the Fermi level is pinned in the middle of the mobility band gap, positioned at its intrinsic value equivalent to that of a crystal. The localized state arises from the substitutional doping of 4-fold positively charged P in the conduction band (see figure 5.35). The corresponding resonant state is attributed to the 4-fold negatively charged P in the valence band (not shown).

In this case, the compensation factor $K = 1$ represents the ratio of N_D (the donor concentration per unit volume) to N_A (the acceptor concentration per unit volume). This implies that the positively ionized donor state $|e|N_D^+$ is balanced by a negatively charged state in the acceptor states N_D^-. Conduction occurs when donor electrons transition into N_A, resulting in $N_D - N_A$ electrons remaining at the donor site.

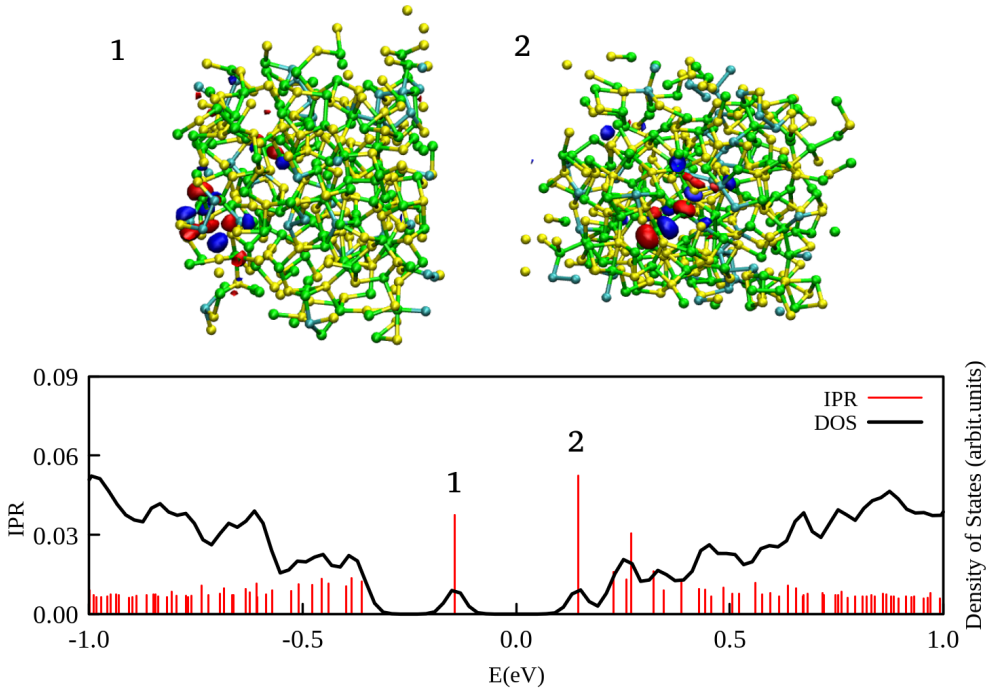

Figure 5.34: Single-particle wave function plots of selected defect states in the mobility gap of the As-doped a-$Ge_{0.5}Se_{0.5}$ at 10 %. Red (blue) isosurfaces indicate the single-particle wave function's positive (negative) sign. The cyan color represent the arsenic atom. The bottom curves are the density of states (black) and the inverse participation ratio (red spikes) of the a-$Ge_{0.5}Se_{0.5}$ at 10 % of As. The localized states are due to: 1) As-Ge bond, and 2) Ge-centered tetrahedron.

Substitutional dopings are also observed in figures 5.36 and 5.37. The dopant atoms, As and P, at the centroid of the tetrahedron, create a singly occupied state in the conduction band gap.

Figures 5.38, 5.39, 5.40, and 5.41 show the origin of localized states in pnictogen-doped a-Ge_xSe_{1-x}. Figure 5.38 illustrates a localized state arising from As-As and Se-Se homopolar bonds. Figure 5.39 shows a localized state due to the P-Ge bond. Figure 5.40 presents cases where the localized state is due to the As-Ge bond. Lastly, Figure 5.41 shows a localized state associated with Se lone pairs and P-Se bond.

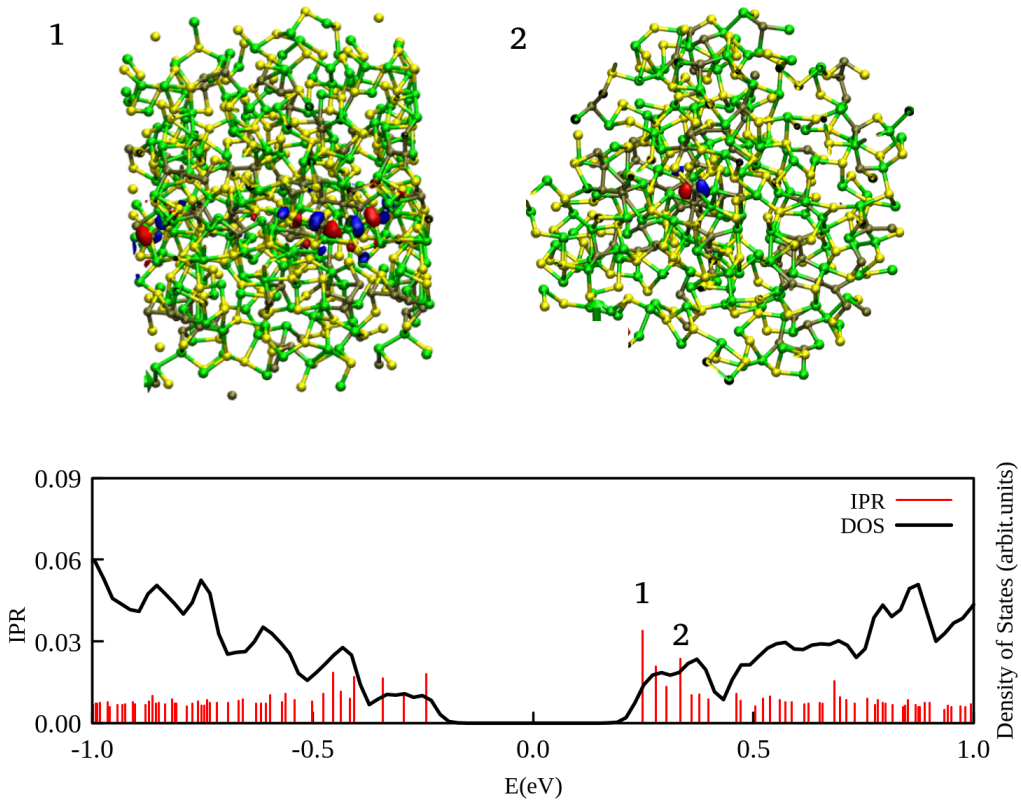

Figure 5.35: Single-particle wave function plots of selected defect states in the mobility gap of the P-doped a-$Ge_{0.5}Se_{0.5}$ at 15%. Red (blue) isosurfaces indicate the positive (negative) sign of the single-particle wave function. The brown color represents the P atom. The bottom curves show the density of states (black) and the inverse participation ratio (red spikes). The localized states are due to substitutional doping: 1) The P atom has a see-saw configuration (the equatorial angle is 163.72° and the tetrahedrality order parameter q = 0.74) and has a positive Bader charge. P has the highest electron occupation, followed by the Ge atom. The ratio of the electron occupation of P to that of Ge is 1.06, while the ratio of the electron occupation of P to that of Se, which has the third highest electron occupation, is 1.75. 2) The P atom (with a positive Bader charge) has an electron occupation four times greater than that of Ge, which has the next highest electron occupation.

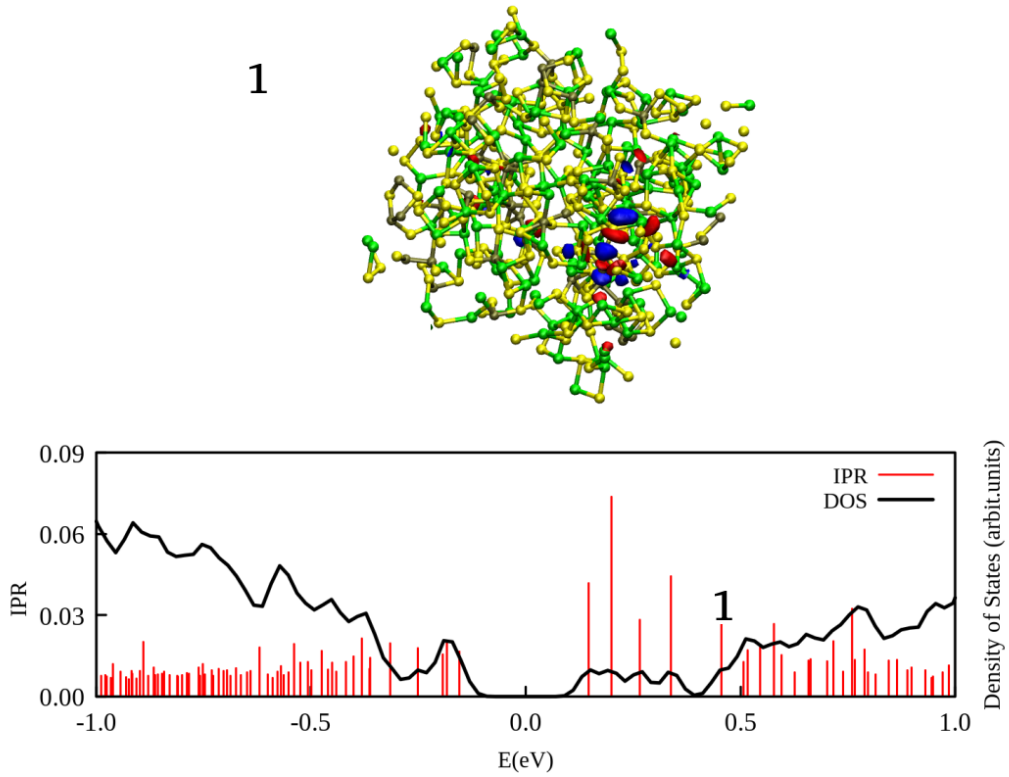

Figure 5.36: Top graph: single-particle wave function plots of selected defect state in the mobility gap of the As-doped a-$Ge_{0.4}Se_{0.6}$ at 10 % . Red (blue) isosurfaces indicate the single-particle wave function's positive (negative) sign. Bottom graph: density of states and inverse participation ratio of the As-doped a-$Ge_{0.4}Se_{0.6}$ at 10 % of As. The localized state is due to : 1) substitutional doping, positive Bader charge.

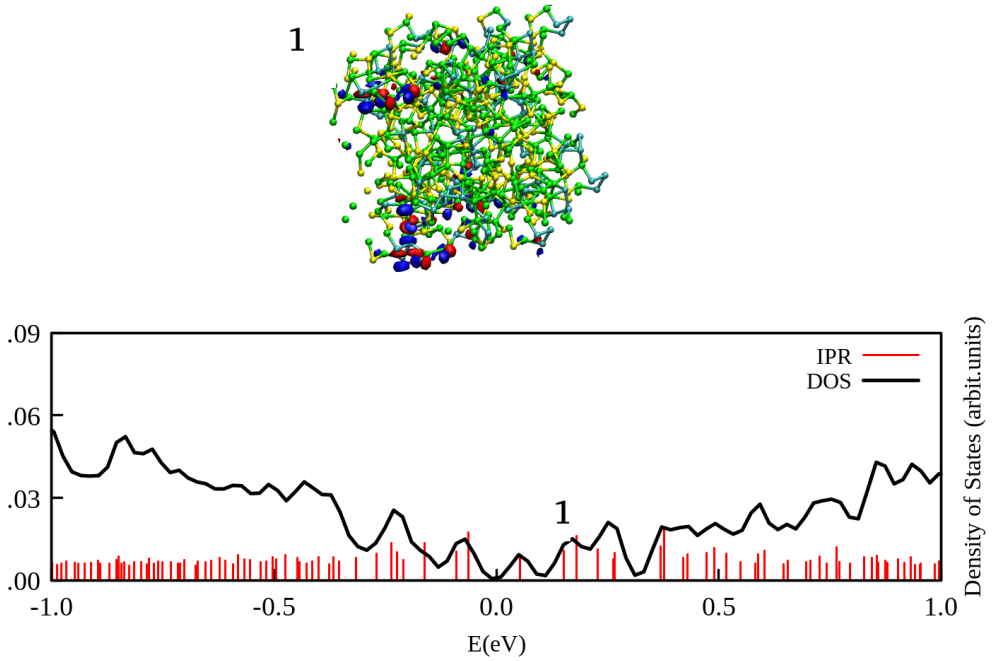

Figure 5.37: Top graph: single-particle wave function plots of selected defect state in the mobility gap of the As-doped a-$Ge_{0.6}Se_{0.4}$ at 15 %. Red (blue) isosurfaces indicate the single-particle wave function's positive (negative) sign. Bottom curves: density of states (black) and inverse participation ratio (red) of the As-doped a-$Ge_{0.6}Se_{0.4}$ at 15 %, 1) substitutional doping, positive Bader charge.

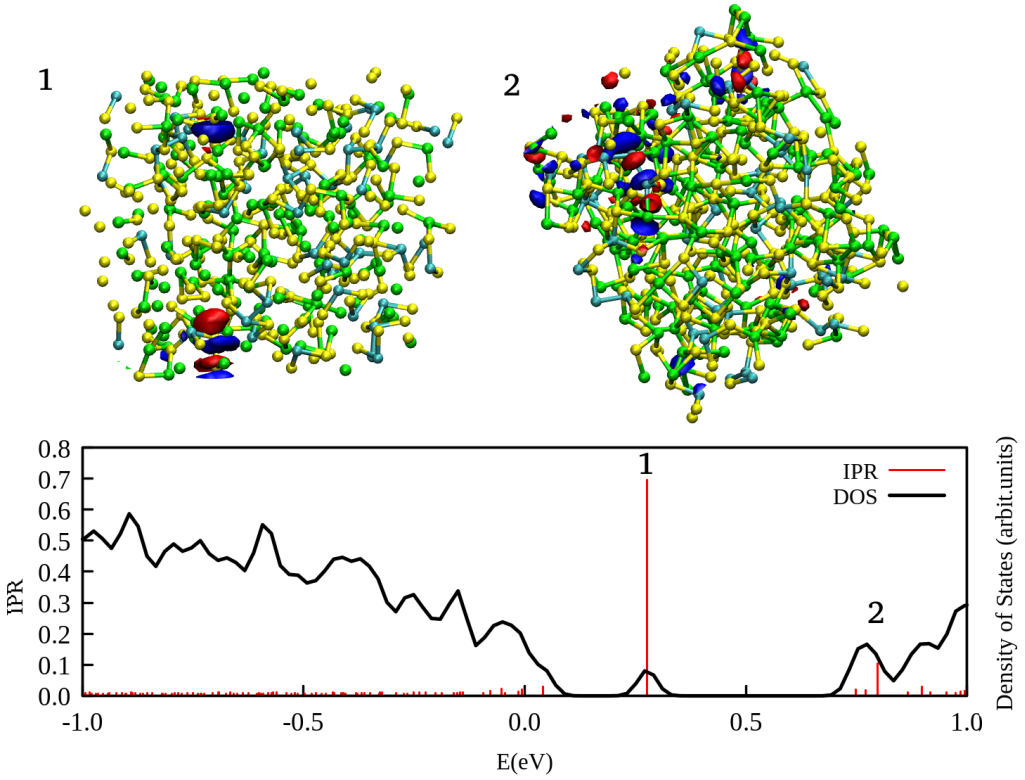

Figure 5.38: Top graph: electronic wave function plots of selected defect states in the mobility gap of As-doped a-$Ge_{0.4}Se_{0.6}$ at 10 %. Red (blue) isosurfaces indicate the single-particle wave function's positive (negative) sign. The bottom curves are the density of states (black) and the inverse participation ratio (red spikes) of the a-$Ge_{0.4}Se_{0.6}$ at 10 % of As. The localized states are due to: 1) the Se-Se bond, 2) the As-As and As-Ge chains.

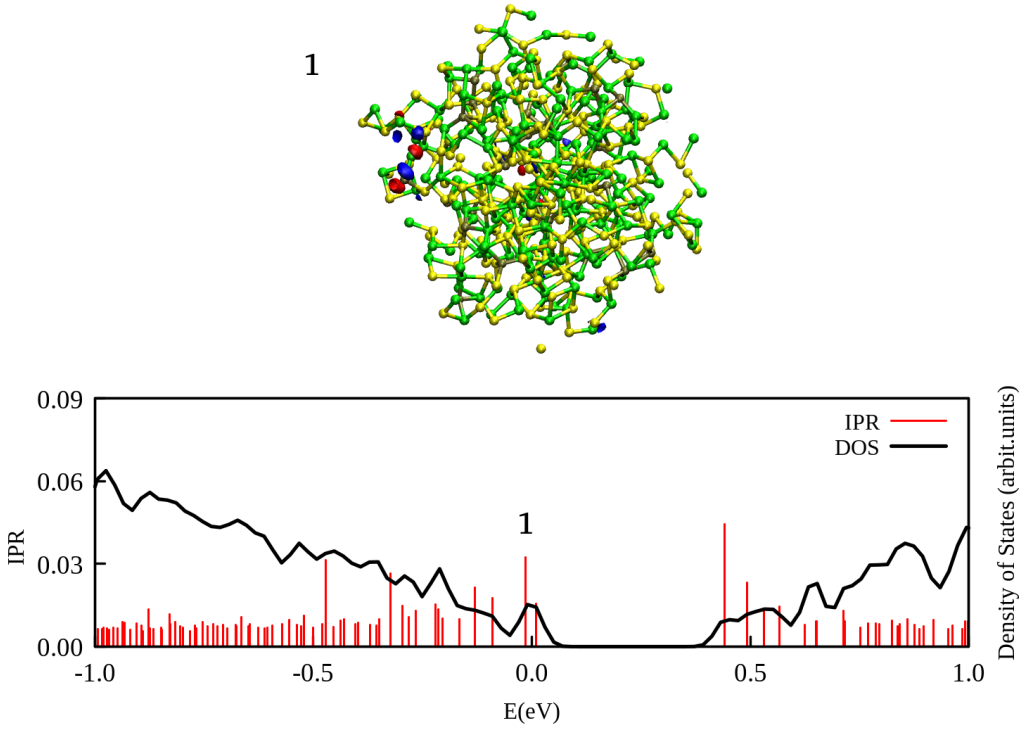

Figure 5.39: Top graph: electronic wave function plot of selected defect state in the mobility gap of P-doped a-$Ge_{0.5}Se_{0.5}$ at 5 %. Red (blue) isosurfaces indicate the single-particle wave function's positive (negative) sign. The bottom curves are the density of states (black) and the inverse participation ratio (red spikes) of the a-$Ge_{0.5}Se_{0.5}$ at 5 % of P. The localized state is due to 1) P-Ge bond.

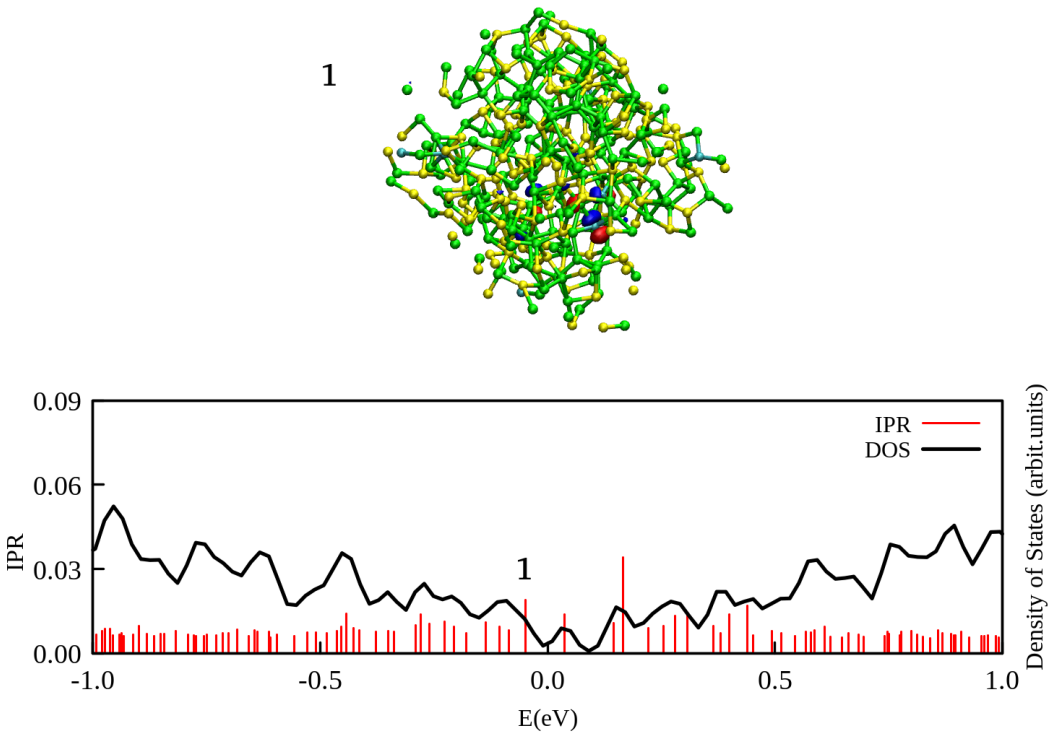

Figure 5.40: Top graph: electronic wave function plots of selected defect state in the mobility gap of As-doped a-$Ge_{0.6}Se_{0.4}$ at 1 %. Red (blue) isosurfaces indicate the single-particle wave function's positive (negative) sign. The bottom curves are the density of states (black) and the inverse participation ratio (red spikes) of the As-doped a-$Ge_{0.6}Se_{0.4}$ at 1 % of As. The localized state is due to 1)As-Ge bond.

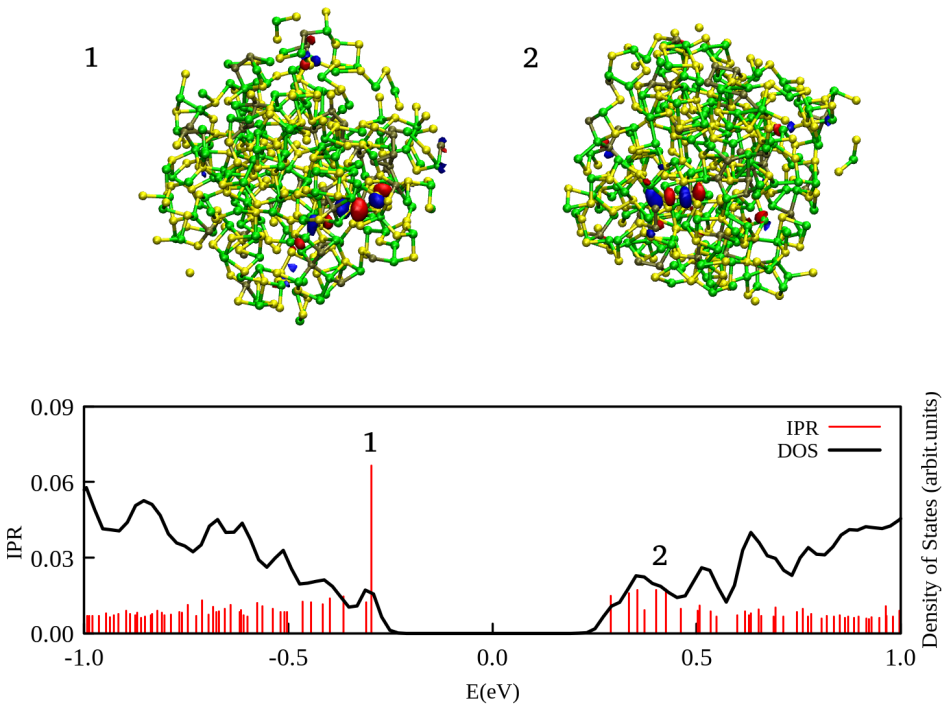

Figure 5.41: Top graphs: electronic wave function plots of selected defect states in the mobility gap of P-doped a-$Ge_{0.5}Se_{0.5}$ at 10 %. Red (blue) isosurfaces indicate the single-particle wave function's positive (negative) sign. The bottom curves are the density of states (black) and the inverse participation ratio (red) of the a-$Ge_{0.5}Se_{0.5}$ at 10 %. The localized states are due to: 1) Se-LP and 2) P-Se bond.

Summary

The partial RDFs of pnictogen-doped a-Ge_xSe_{1-x} reveal distinct trends across stoichiometries.

In stoichiometric and Ge-rich samples, P-Ge RDFs show a distinct first neighbor shell at all concentrations. P dopants interact similarly with Se and Ge in stoichiometric samples and do not significantly alter Ge-Ge, Ge-Se, or Se-Se RDFs. The P-P bond length is 2.25 Å, aligning closely with the P-P bond length in elemental P, though no P-P bonds are observed at low concentrations of P in certain samples.

In stoichiometric and Se-rich As-doped samples, Ge-Ge distances are part of the second neighbor shell, with few Ge-Ge bonds, whereas Ge-rich samples exhibit Ge-Ge RDF as a first neighbor shell. Across all stoichiometries, Se-Se RDF shows consistency with a peak around 4 Å. Increasing As concentration in a-$Ge_{0.4}Se_{0.6}$ reduces Se-Se bonds. The Ge-Se RDF shows a clear first neighbor peak at 2.5 Å, with As doping having minimal effect on the Ge-Ge, Se-Se, and Ge-Se RDFs in stoichiometric and Se-rich samples but modifying the Ge-Ge first-neighbor shell in Ge-rich samples.

For stoichiometric samples, As-Ge, As-Se, and As-As RDFs exhibit distinct first and second shells characteristic of the SRO and the MRO, respectively. In Se-rich samples, As-Se bonds remain prominent, whereas As-Ge RDFs dominate in Ge-rich samples. However, the As form bonds equally with Ge and Se in the stoichiometric sample. Typical As-As bond lengths of 2.55 Å and 2.75 Å align with observed values depending on As content and sample composition.

The bond angle distribution functions (ADFs) for P- and As-doped amorphous a-Ge_xSe_{1-x} show characteristic patterns across different stoichiometries.

P-doped a-Ge_xSe_{1-x}:

- Ge-Centered ADF: A symmetric, bell-shaped peak around 90°–95°, indicating a trigonal pyramidal structure across all stoichiometries.
- Se-Centered ADF: Displays a broader range from 90°to 109°, consistent with both trigonal pyramidal and tetrahedral Se environments.
- P-Centered ADF: Peaks around 104°–109°, reflecting a tetrahedral network. In Se-rich samples, increased Se content narrows the P-centered angle distribution due to Se higher electronegativity.

As-doped a-Ge_xSe_{1-x}:

- Ge-Centered ADF: Maintains a symmetric peak around 97°, broadening in the Ge-rich a-$Ge_{0.6}Se_{0.4}$ due to As substitution for more electronegative Se.

- Se-Centered ADF: Initially centered around 90°with a shoulder at 109°at low As levels, suggesting trigonal pyramidal and tetrahedral motifs. Increased Ge content causes distinct peaks at 90°and 109.5°, depending on As concentration.
- As-Centered ADF: Typically peaks near 97°for a-$Ge_{0.5}Se_{0.5}$ and $Ge_{0.4}Se_{0.6}$. At higher As content (10%), the main peak shifts toward 109.5°in the stoichiometric sample. In Ge-rich samples, the As-centered ADF broadens and includes a notable bump at 170°, indicating a potential trigonal bipyramidal structure with pentacoordinated As atoms. As the As concentration increases, the ADF shifts to a more symmetric range around 104°–109.5°.

The coordination analysis of Ge, Se, P, and As in a-Ge_xSe_{1-x} vary with dopant concentration and composition, revealing distinct coordination behaviors influenced by dopant concentration and composition.

In P-doped a-$Ge_{0.5}Se_{0.5}$, Ge is predominantly 3-fold coordinated, although hexacoordination begins to appear at higher dopant concentrations (7-15%). A similar trend is observed in the Se-rich sample, where Ge remains mostly 3-fold coordinated, with hexacoordination emerging at 15%. In contrast, As-doped samples exhibit more variation in Ge coordination: in the stoichiometric and Se-rich samples, Ge is coordinated in both 3-fold and 4-fold arrangements, with the proportion of each depending on the composition. In the Ge-rich sample, Ge is primarily 4-fold coordinated.

Se coordination remains consistent across all compositions for both P- and As-doped samples, with Se consistently exhibits 3-fold coordination.

The coordination of P differs significantly between samples. In the stoichiometric and Ge-rich P-doped samples, P is predominantly 4-fold coordinated, indicating substitutional doping. However, in the Se-rich sample, P is mostly 3-fold coordinated, with no instances of hexacoordination. This suggests that P in the Se-rich composition mainly acts as a defect compensator, which may lead to a wider band gap and accelerate crystallization.

In the case of As, the coordination varies according to the composition. In the stoichiometric and Se-rich samples, As has both 3-fold and 4-fold coordination. However, in the Ge-rich sample, As is primarily 4-fold coordinated. This coordination variation reflects the impact of composition and dopant concentration on atomic bonding, influencing the material's crystallization behavior and band gap properties.

5.4 Chalcogen-doped a-Ge_xSe_{1-x}

5.4.1 Structural properties

RDF

Figures 5.42, 5.43 and 5.44 show the partial pair correlation functions of the S-doped a-$Ge_{0.5}Se_{0.5}$, a-$Ge_{0.4}Se_{0.6}$ and a-$Ge_{0.6}Se_{0.4}$ respectively.
The Ge-Ge partial RDFs in a-$Ge_{0.5}Se_{0.5}$ and a-$Ge_{0.4}Se_{0.6}$ show predominantly second-neighbor shell distances, with very few Ge-Ge bonds observed. However, in the a-$Ge_{0.6}Se_{0.4}$ stoichiometry, generally, Ge-Ge bonds are more prominent than the Ge-Ge distances of the second neighbor shell except at higher S content. This implies that Ge atoms are primarily bonding with Se or S in these stoichiometries, resulting in a less interconnected Ge network compared to Ge-rich stoichiometry. On the contrary, as the S concentration increases, we observe a rise in the number of Se-Se bonds in the doped a-$Ge_{0.5}Se_{0.5}$ and a-$Ge_{0.4}Se_{0.6}$ samples. Therefore, adding the S dopants favors the formation of the Se network in these stoichiometries. However, in the Ge-rich sample, no Se-Se bond is found.
The Ge-Se RDFs in a-$Ge_{0.5}Se_{0.5}$ and a-$Ge_{0.4}Se_{0.6}$ show no medium-range order, while a-$Ge_{0.6}Se_{0.4}$ stoichiometry does exhibit medium-range order at low S concentrations. However, this MRO order disappears as the S concentration increases. This suggests that the addition of sulfur primarily affects the longer-range structural order rather than the immediate bonding environment.
The Ge-Se and S-Ge RDFs are generally similar in all 3 stoichiometries. Specifically for the S-Ge RDF in the Se-rich samples, at some dopant concentration within the first coordination shell, some short and longer bonds exist. The short bonds in the first coordination shell represent stronger bonds, where S atoms closely interact with Ge atoms. The longer bonds, on the other hand, suggest weaker interactions, possibly due to strained bonding or geometrical distortions in the structure.
At higher S concentrations, a few S-Se bonds start to form in the doped a-$Ge_{0.5}Se_{0.5}$ sample and across various dopant levels in the Se-rich sample, except at 3% S. In contrast, no S-Se bonds are observed in the a-$Ge_{0.6}Se_{0.4}$ stoichiometry. The S-Se RDFs closely resemble the Se-Se RDFs across all three stoichiometries, and no S-S bonds are observed in any composition. This pattern suggests that sulfur behaves similarly to selenium in the amorphous network.

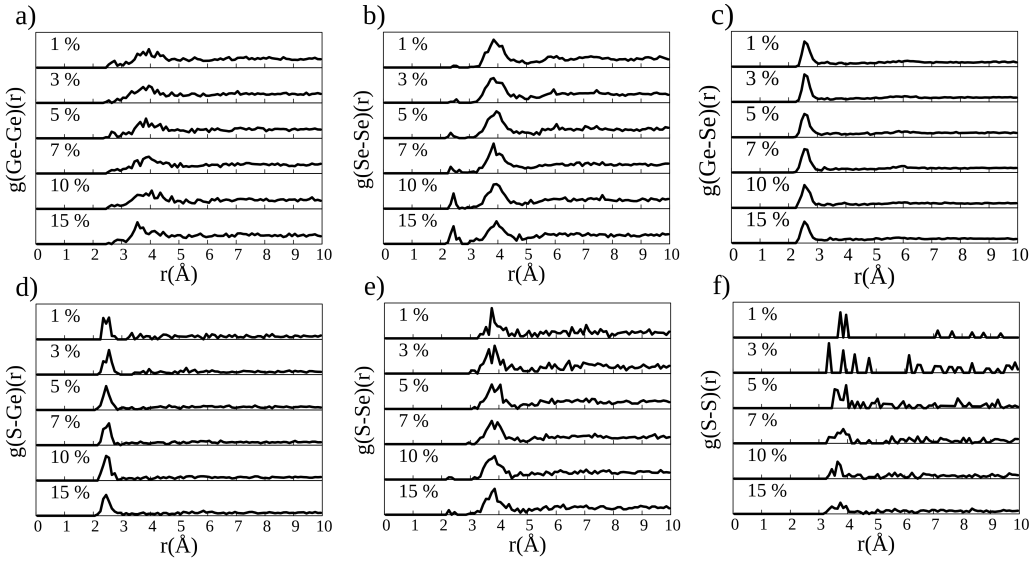

Figure 5.42: RDF of the S-doped a-$Ge_{0.5}Se_{0.5}$ for the pairs of a) Ge-Ge, b) Se-Se, c) Ge-Se, d) S-Se, e) S-Ge, f) S-S

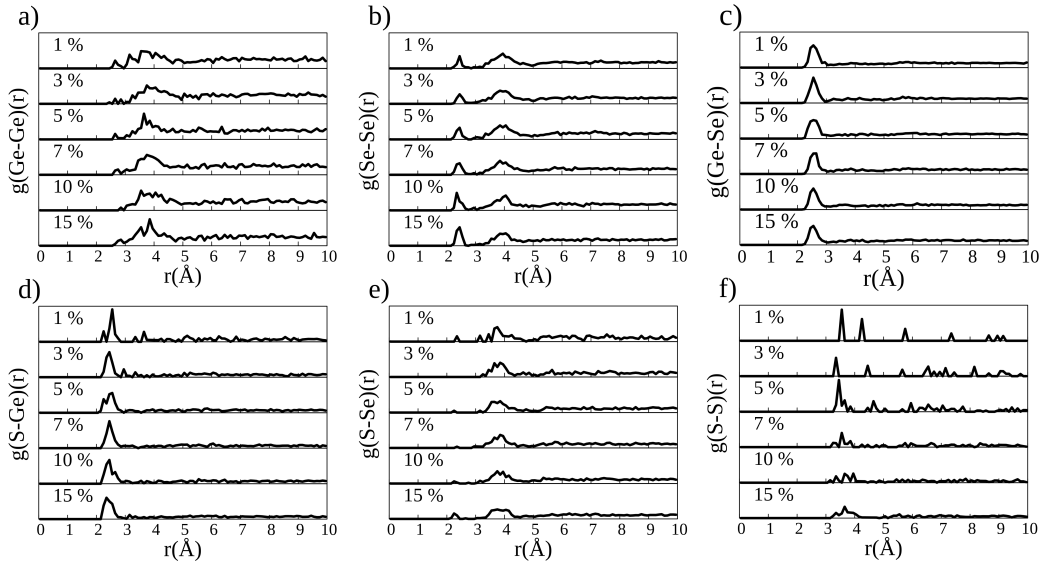

Figure 5.43: RDF of the S-doped a-$Ge_{0.4}Se_{0.6}$ for the pairs of a) Ge-Ge, b) Se-Se, c) Ge-Se, d) S-Se, e) S-Ge, f) S-S

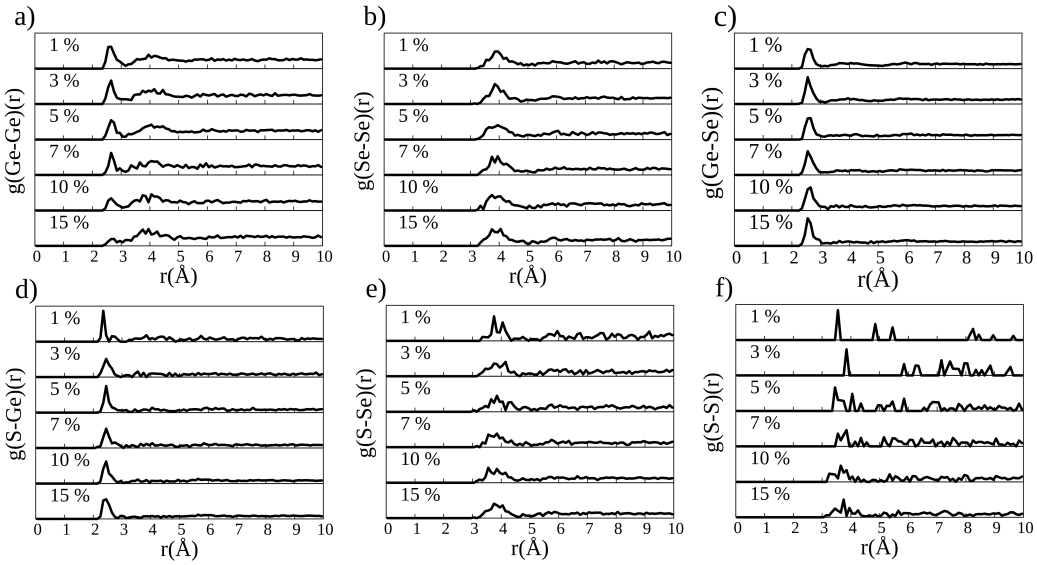

Figure 5.44: RDF of the S-doped a-$Ge_{0.6}Se_{0.4}$ for the pairs of a) Ge-Ge, b) Se-Se, c) Ge-Se, d) S-Se, e) S-Ge, f) S-S

Figures 5.45, 5.46, and 5.47 show the RDF of the Te-doped a-Ge_xSe_{1-x}. In this study, the RDF for the Ge-Ge, Se-Se, Ge-Se, Te-Ge, Te-Se, and Te-Te pairs are analyzed as the concentration of Te increases.
For the Ge-Ge pair correlation functions, in the a-$Ge_{0.5}Se_{0.5}$ and the a-$Ge_{0.4}Se_{0.6}$ stoichiometries, one prominent peak is observed at about 4 Å, with a shoulder at the first neighbor shell at 2.5 Å. Meanwhile, Ge-Ge bonds are the main distance in the Ge-Ge RDFs for the a-$Ge_{0.6}Se_{0.4}$ stoichiometry. Therefore, adding Ge breaks up and cross-links the Se chain and creates $GeSe_4$ units. This trend is also observed in the S-doped a-Ge_xSe_{1-x}.
In the a-$Ge_{0.5}Se_{0.5}$ stoichiometry, at most 3 Se-Se bonds are formed in each sample, whereas in the S-doped a-Ge_xSe_{1-x} additional Se-Se bonds are observed at higher dopant concentration. This suggests that adding S as a dopant, rather than Te, promotes a stronger formation of a Se network. The Se-rich samples in the both chalcogenide-doped a-Ge_xSe_{1-x} samples show the same trend. Meanwhile, the Se-Se distance remains primarily characteristic of the second-neighbor shell in the Ge-rich sample.
The Ge-Se RDFs reveal only subtle differences across all dopant concentrations and all the stoichiometries, with well-defined first-neighbor shells peaking at 2.5 Å. In the stoichiometric and Se-rich samples, no MRO is found in the Ge-Se RDFs. However, the Ge-rich sample exhibits MRO at low concentrations, which diminishes as the Te concentration increases (see figure 5.47). This pattern is similar to what we also observe in the S-doped a-Ge_xSe_{1-x}
The Te-Ge RDFs show first-neighbor shells in all samples.
At 1% of Te In the stoichiometric sample, the g(Te-Se)(r) function shows no Te-Se bonding. Conversely, a-$Ge_{0.4}Se_{0.6}$ exhibits Te-Se bonds at all dopant concentrations, while no Te-Se bonds are observed in the Ge-rich samples. This suggests that Te tends to bond with Ge rather than Se.
In the stoichiometric sample, homonuclear Te-Te bonds form at higher Te content. The typical Te-Te bond length found in the literature is 2.89 Å within the chain of bulk Te ($P3_121$) [Zha+21] and 2.74 Å in elemental Te [Ibe09], which are similar to the Te-Te bond length observed in the stoichiometric sample. At 5% Te, the Te-Te bond length is approximately 2.94 ± 0.05 Å, decreasing to 2.84 ± 0.05 Å at 10% and 15%. In the a-$Ge_{0.4}Se_{0.6}$ stoichiometry, the Te-Te bond length is found to be 2.84 ± 0.05 Å at 5%, 7%, 10%, and 15% Te, which is similar to the value of 2.83 Å found in rhombohedral GeTe (space group R3m) [Fon+10].
The variation in bond length can be attributed to both the stoichiometry of the sample and the specific structural environment.

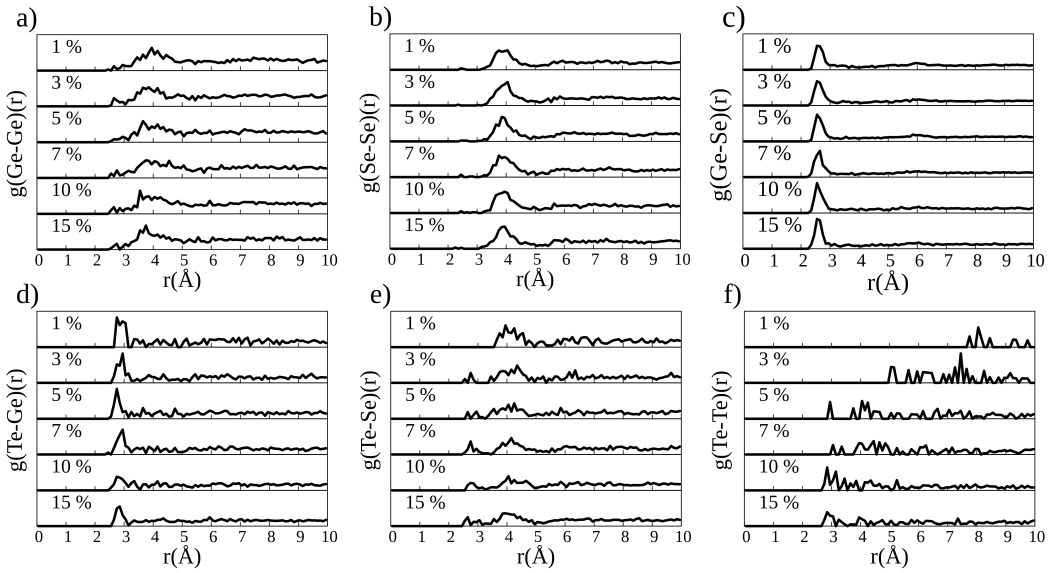

Figure 5.45: RDF of the Te-doped a-$Ge_{0.5}Se_{0.5}$ for the pairs of a) Ge-Ge, b) Se-Se, c) Ge-Se, d) Te-Se, e) Te-Ge, f) Te-Te

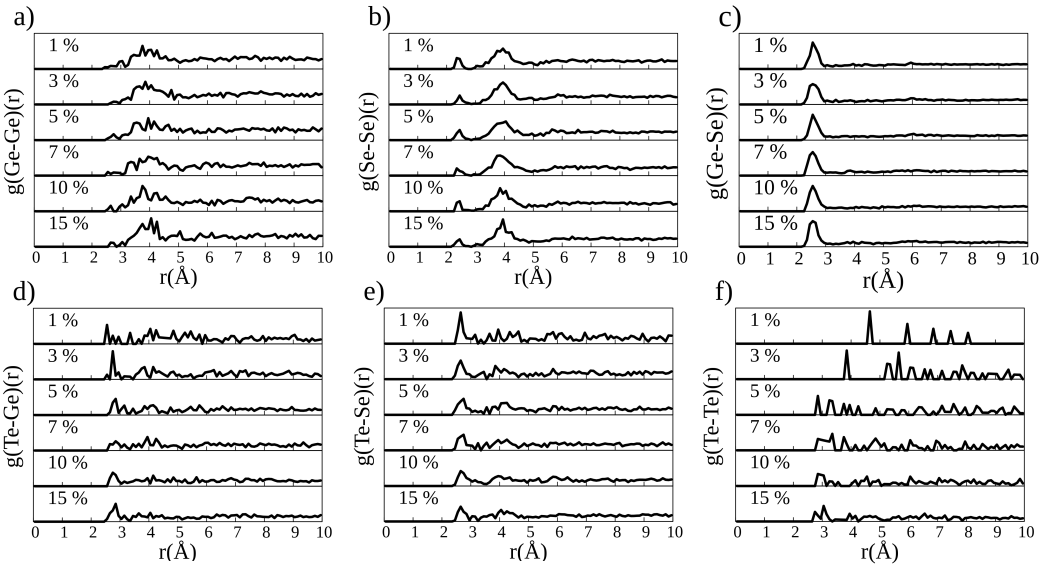

Figure 5.46: RDF of the Te-doped a-$Ge_{0.4}Se_{0.6}$ for the pairs of a) Ge-Ge, b) Se-Se, c) Ge-Se, d) Te-Se, e) Te-Ge, f) Te-Te

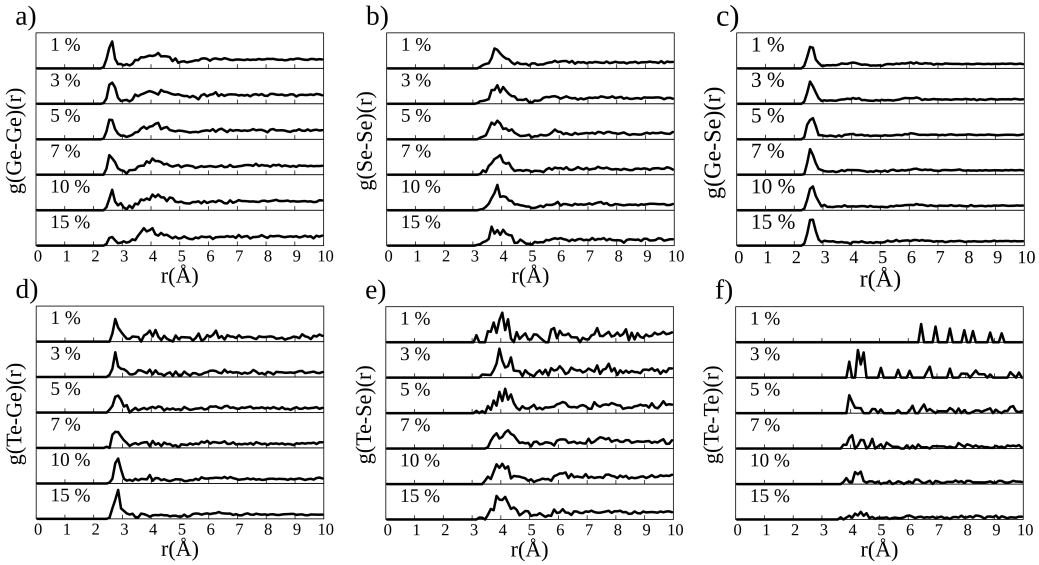

Figure 5.47: RDF of the Te-doped a-$Ge_{0.6}Se_{0.4}$ for the pairs of a) Ge-Ge, b) Se-Se, c) Ge-Se, d) Te-Se, e) Te-Ge, f) Te-Te

ADF

Figures 5.48, 5.49, and 5.50 show the ADFs of the S-doped a-Ge_xSe_{1-x}. Figure 5.48, panel a, shows Ge-centered ADFs, which are more symmetrical and show a higher angle probability in the range [90°, 100 °], indicative of a pyramidal trigonal structure, confirmed by the coordination analysis(see figure 5.54) marked by the presence of a 3-fold coordinated Ge and a small fraction of bipyramidal trigonal structure marked by the presence of pentacoordinated Ge. The Se-centered ADFs (see figure 5.48 panel b) in a-$Ge_{0.5}Se_{0.5}$ at low concentrations (1 and 3 % of S) have more weight around 90°, indicative of amorphous network marked by the predominance of 3-fold structural motifs. As the concentration of S increases, we notice an increase in the probability of having bigger angles as the weight of the tail of the ADFs increases. This is because S has an electronegativity of 2.5. Se, which has an electronegativity of 2.4 repeals each other as seen from the RDF in figure 5.42; however, more Se-Se bonds are formed as S increases. Therefore, Se-centered ADFs primarily comprise bonds formed with Ge and Se atoms, which have lower electronegativity, resulting in larger bond angles. In the Ge-rich sample, the Se-centered ADF displays a broader distribution toward larger angles. This occurs because, in Ge-rich samples, Se bonds exclusively with Ge, which has a much lower electronegativity than Se. As a result, the bond angles around the

central Se atom are larger. At 1 % of S, the S-centered ADF is centered around 90°in the stoichiometric sample. As the S concentration increases, the S-centered ADF becomes broader for the aforementioned reason. The S has an electronegativity of 2.5, making it more electronegative than Se, justifying its wider angle distribution. The bond angle is smaller when the electronegativity of the ligands is higher.

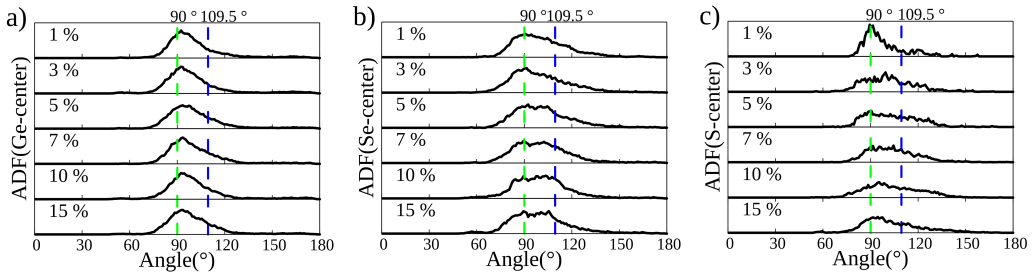

Figure 5.48: Angle distribution functions of the S-doped a-$Ge_{0.5}Se_{0.5}$, a) Ge-center, b) Se-center, c) S-center. The green and blue dashed lines represent the well-known angles for molecular clusters: 90°corresponds to an octahedral or trigonal bipyramidal structure, and 109.5 °corresponds to a tetrahedral molecular cluster.

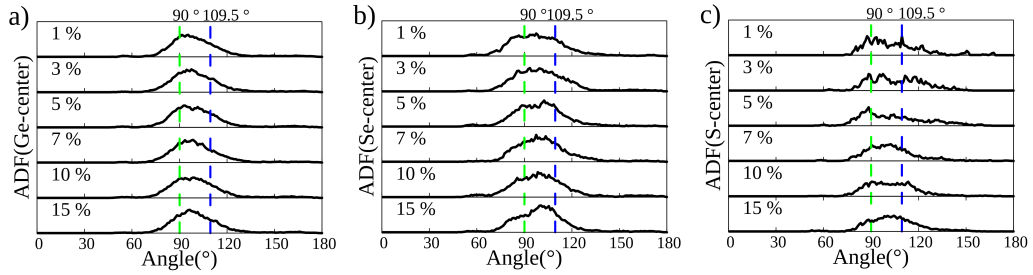

Figure 5.49: Angle distribution functions of the S-doped the S-doped a-$Ge_{0.4}Se_{0.6}$: a) Ge-center, b) Se-center, c) S-center. The green and blue dashed lines represent the well-known angles for molecular clusters: 90°corresponds to an octahedral or trigonal bipyramidal structure, and 109.5 °corresponds to a tetrahedral molecular cluster.

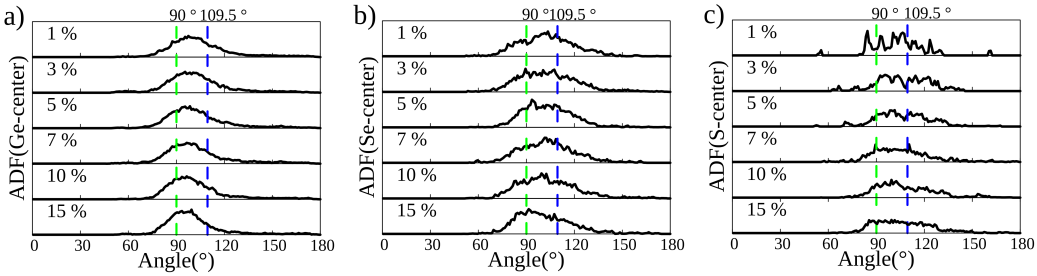

Figure 5.50: Angle distribution functions of the S-doped a-$Ge_{0.6}Se_{0.4}$: a) Ge-center, b) Se-center, c) S-center. The green and blue dashed lines represent the well-known angles for molecular clusters: 90°corresponds to an octahedral or trigonal bipyramidal structure, and 109.5 °corresponds to a tetrahedral molecular cluster.

Figures 5.51, 5.52 and 5.53 and show the ADFs of Te-doped a-Ge_xSe_{1-x}. The green and blue dashed lines represent the perfect octahedral and tetrahedral configurations at 90°and 109 °, respectively. The Ge-centered ADFs exhibit greater symmetry, displaying a bell shape in the stoichiometric sample and a broader angular distribution in the Se-rich and Ge-rich samples. In the stoichiometric sample, Se-centered ADFs show a bump at 90°and a broad tail over big angles. In Te-doped a-Ge_xSe_{1-x}, the Te-centered ADFs are generally broad and spread over several angles across all three stoichiometries, except in the stoichiometric sample at 1% Te, where the Te-centered ADF peak is located at 90°. As the Te concentration increases, the distribution becomes flatter due to the low coordination of Te. This suggests that Te prefers to bond with Ge rather than Se, as seen in the RDF in Figure 5.45. The electronegativity of Te is higher than that of Ge (2.1 versus 1.8), resulting in larger bond angles around the central Te atoms. The Te-centered ADFs in the stoichiometric and Se-rich samples have angles within the range [160 °, 180 °], indicating the presence of a 2-fold Te chain, also known as a bent (V-shaped) molecular structure.

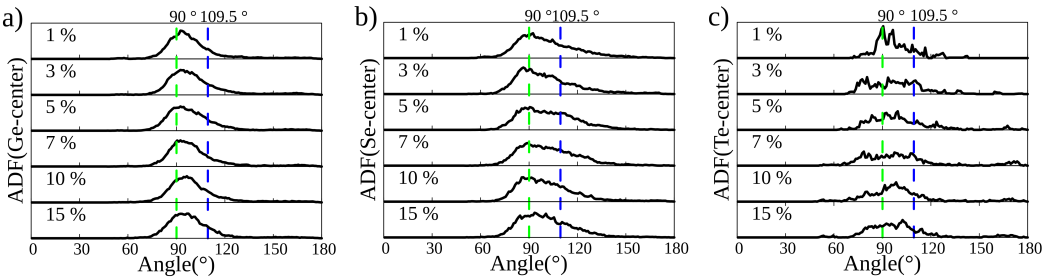

Figure 5.51: Angle distribution functions of the Te-doped a-$Ge_{0.5}Se_{0.5}$: a) Ge-center, b) Se-center, c) Te-center. The green and blue dashed lines represent the well-known angles for molecular clusters: 90°corresponds to octahedral or trigonal bipyramidal structural motifs, and 109.5°is the bond angle in the tetrahedral molecular cluster.

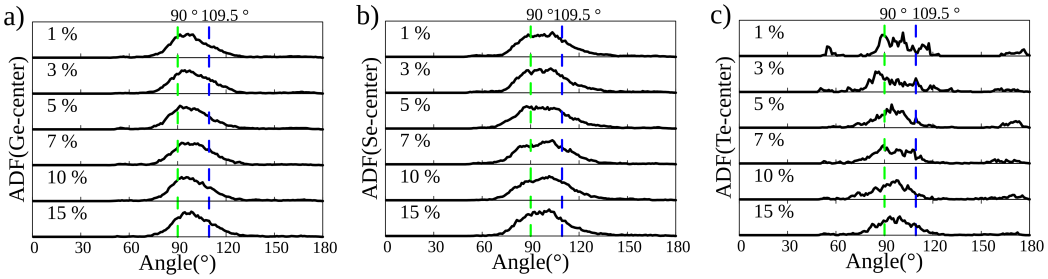

Figure 5.52: Angle distribution functions of the Te-doped a-$Ge_{0.4}Se_{0.6}$, a) Ge-center, b) Se-center, c) Te-center. The green and blue dashed lines represent the well-known angles for molecular clusters: 90°corresponds to octahedral or trigonal bipyramidal structural motifs, and 109.5°is the bond angle in the tetrahedral molecular cluster.

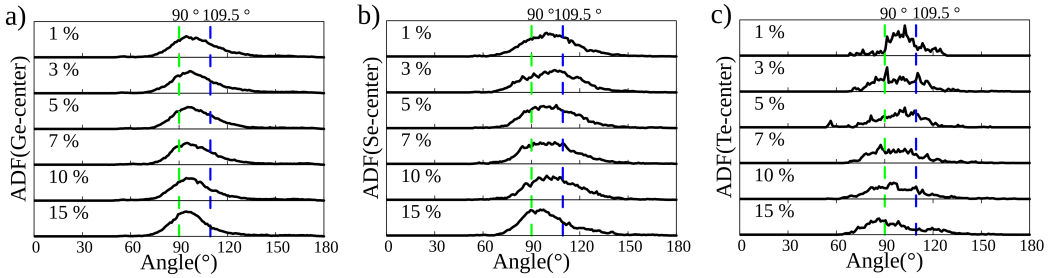

Figure 5.53: Angle distribution function of the Te-doped a-$Ge_{0.6}Se_{0.4}$, a) Ge-center, b) Se-center, c) Te-center. The green and blue dashed lines represent the well-known angles for molecular clusters: 90°corresponds to octahedral or trigonal bipyramidal structural motifs, and 109.5°is the bond angle in the tetrahedral molecular cluster.

Coordination analysis

Figures 5.54, 5.55, and 5.56 show the coordination analysis of the S-doped a-Ge_xSe_{1-x}. In the stoichiometric and Se-rich samples, Ge is primarily 3 and 4-fold coordinated, while in the Ge-rich sample, Ge is mostly 4-fold coordinated, with an exception observed at 15%, where the proportion of 3-fold Ge exceeds that of 4-fold Ge. The coordination analysis of Se reveals primary 3-fold coordination in the stoichiometric and Ge-rich samples, whereas, in the Se-rich samples, Se is mainly 2-and 3-fold coordinated. The S coordination predominantly exhibits 3-fold coordinated structures in the stoichiometric, Se-rich, and Ge-rich samples.

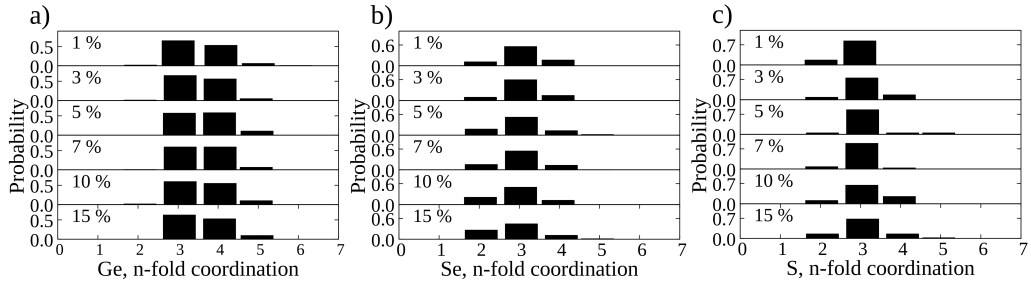

Figure 5.54: Coordination analysis for S-doped a-$Ge_{0.5}Se_{0.5}$. The histograms report the number of atoms of a specific species in a given coordination.

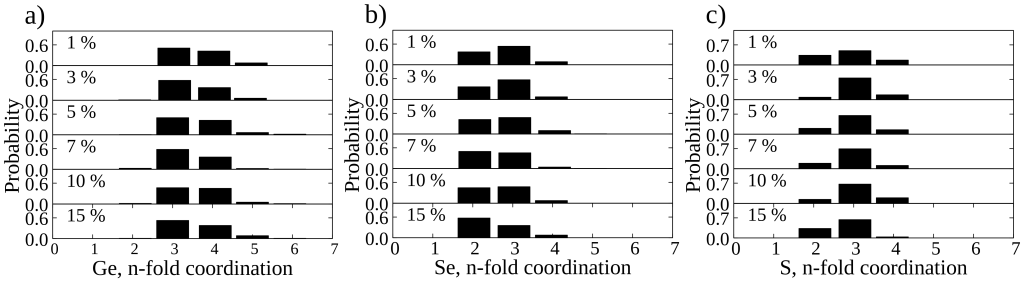

Figure 5.55: Coordination analysis for S-doped a-$Ge_{0.4}Se_{0.6}$. The histograms report the number of atoms of a specific species in a given coordination.

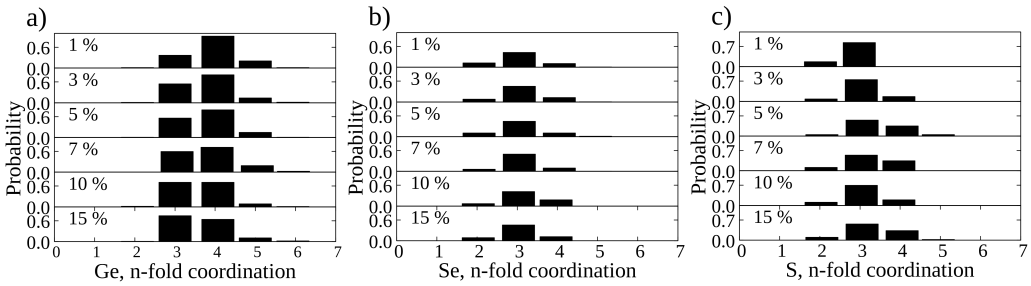

Figure 5.56: Coordination analysis for S-doped a-$Ge_{0.6}Se_{0.4}$. The histograms report the number of atoms of a specific species in a given coordination.

Figure 5.57, 5.58, and 5.59 show the coordination analysis of the Te-doped a-Ge_xSe_{1-x}. In addition to what we observe in the S coordination, the Te atoms entered the amorphous network in 1-fold coordination at 10 and 15 % of the Te-doped a-$Ge_{0.5}Se_{0.5}$ and 3 and 15 % of the a-$Ge_{0.4}Se_{0.6}$. As we shall discuss later, the presence of 1-fold Te may indicate the presence of VAP.

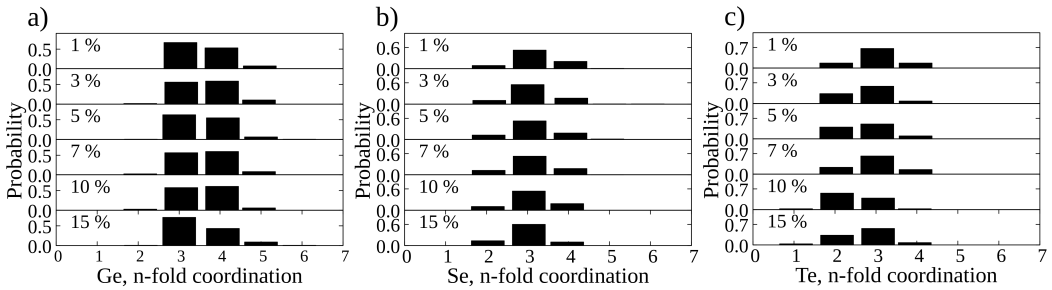

Figure 5.57: Coordination analysis for Te-doped a-$Ge_{0.5}Se_{0.5}$. The histograms report the number of atoms of a specific species in a given coordination.

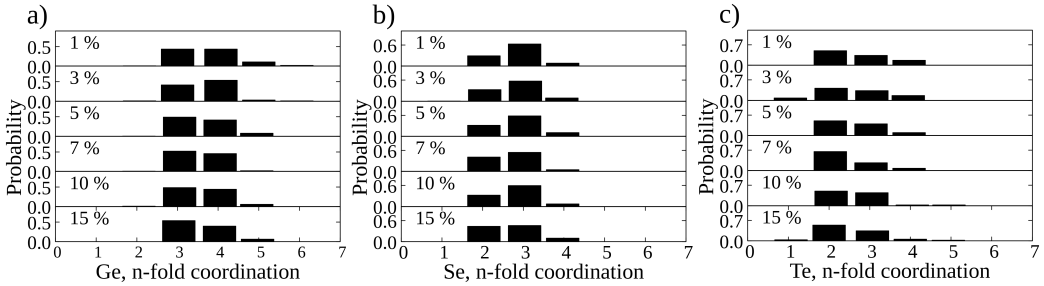

Figure 5.58: Coordination analysis for Te-doped a-$Ge_{0.4}Se_{0.6}$. The histograms report the number of atoms of a specific species in a given coordination.

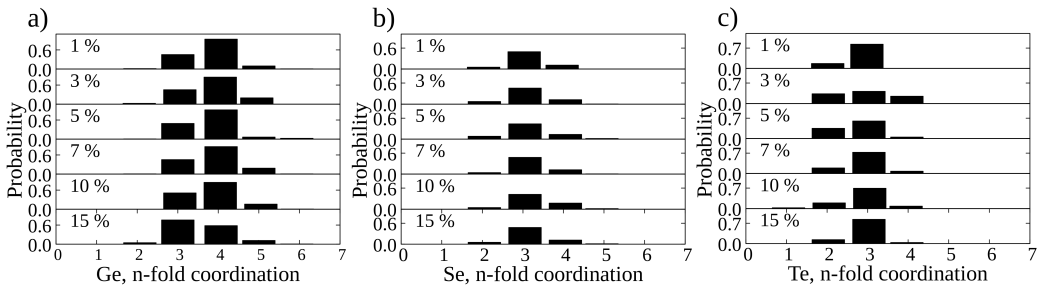

Figure 5.59: Coordination analysis for Te-doped a-$Ge_{0.6}Se_{0.4}$. The histograms report the number of atoms of a specific species in a given coordination.

The germanium chalcogenide cubane

In a-Ge_xSe_{1-x}, several types of molecular assemblies exist: the $Ge(Se_{1/2})_4$ tetrahedra, trigonal bipyramidal, see-saw configurations [LE22], and an ethane-like $Ge_2(Se_{1/2})_6$ structure cluster. Our results are in accordance with the complex model proposed by [Boo+86], based on Raman and Mössbauer spectroscopy, in which the presence of an ethane-like structure is qualitatively incompatible with the chemically ordered random network in which each Ge should be 4-fold coordinated to chalcogen atoms, and the chalcogen is 2-fold.

We find a specific class of structural motif, a double-layered structure (see figure 5.60), in the S- and Te-doped a-Ge_xSe_{1-x}. This structural motif, M_4Ch_4, where M is a metal and Ch is a chalcogen, is called the cubane. This cluster type is typical in biological systems containing iron-sulfur proteins such as Fe_4S_4 [PCR18]. In our case, since the structure contains four chalcogenide atoms and four Ge atoms at the corners, we name it the **germanium chalcogenide cubane**. We report all the cases found in figure 5.60 for the S-doped a-$Ge_{50}Se_{50}$[5]. The germanium chalcogenide cubane structure symbolizes the presence of structurally ordered assemblies in disordered materials: the germanium and the chalcogen atoms alternate on the vertices of a cubic conformation. The germanium chalcogenide cubane (Ge_4Ch_4) clusters we found have all Ge atoms positively charged and all chalcogen atoms negatively charged. On a general note, cubane chalcogenide complexes of Group IV metals are poorly studied [KF03]. From a DFT perspective, this is the first time the cubane structure has been identified in germanium-based amorphous chalcogenide glasses.

5 The germanium chalcogenide cubanes for the Te-doped a-$Ge_{50}Se_{50}$ are not shown because they lie at the boundary of the cell.

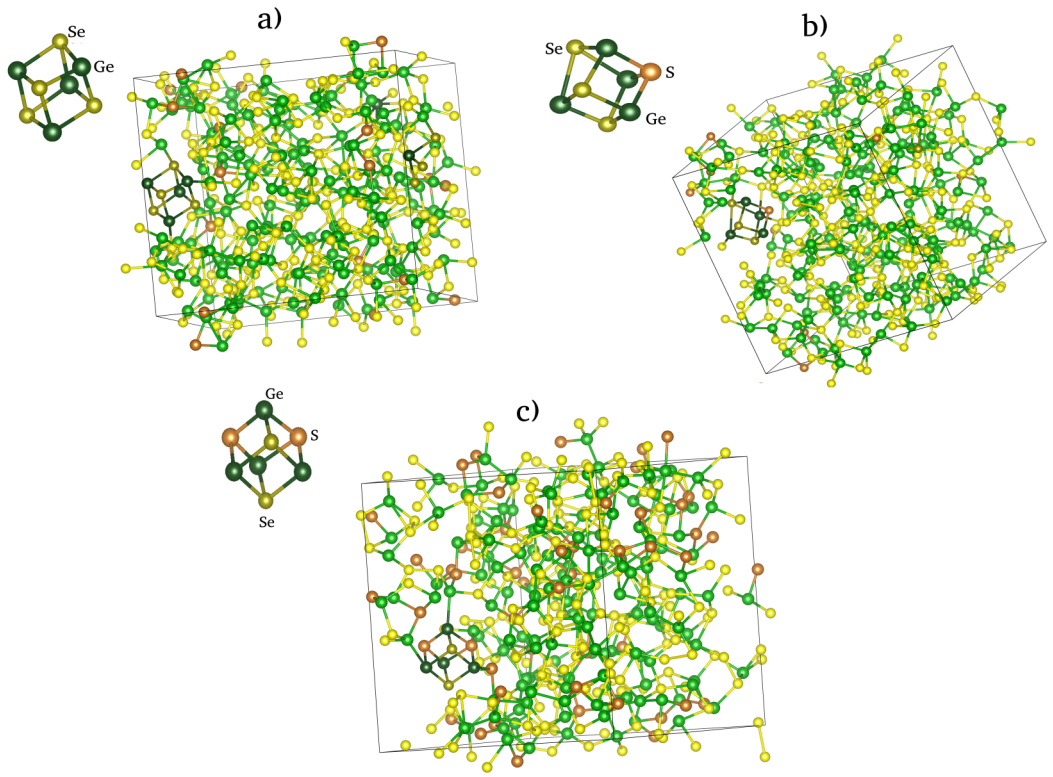

Figure 5.60: The germanium chalcogenide cubane structures: a) 3% S-doped a-$Ge_{50}Se_{50}$, b) 1% S-doped a-$Ge_{50}Se_{50}$ and c) 10% S-doped a-$Ge_{50}Se_{50}$

5.4.2 Electronic properties

In this section, we show the DOS, the IPR of the chalcogenide-doped a-Ge_xSe_{1-x}, and the linking between the electronic and the structural properties. The color orange in the plot is associated with S atoms.

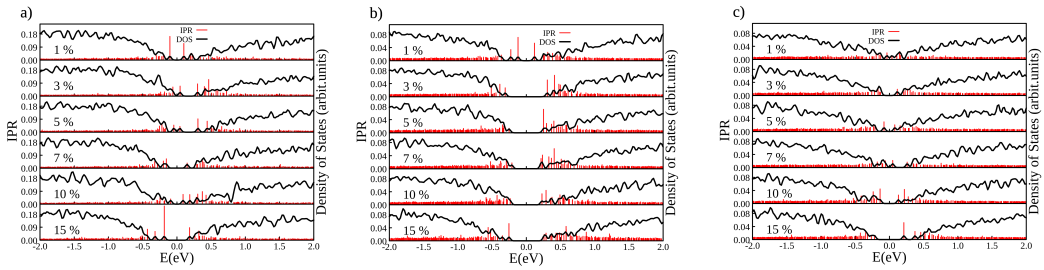

Figure 5.61: Density of states (black curves) and inverse participation ratio (red spikes) of the S-doped samples at 1%, 3%, 5%, 7%, 10%, and 15%: a) a-$Ge_{40}Se_{60}$, b) a-$Ge_{50}Se_{50}$, and c) a-$Ge_{60}Se_{40}$

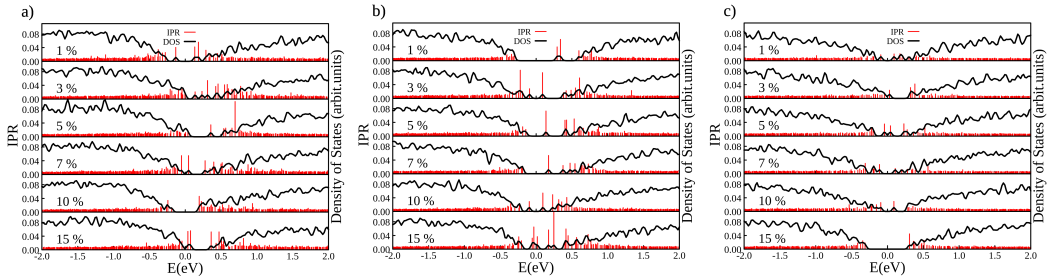

Figure 5.62: Density of states (black curves) and inverse participation ratio (red spike) of the Te-doped samples at 1%, 3%, 5%, 7%, 10%, and 15%: a) a-$Ge_{40}Se_{60}$, b) a-$Ge_{50}Se_{50}$, and c) a-$Ge_{60}Se_{40}$

Figures 5.61 and 5.62 show the electronic DOS and the IPR of the chalcogenide-doped a-Ge_xSe_{1-x}. The trap states can be classified as donor or acceptor depending on their energy level regarding the valence or the conduction band. The donor states are close to the conduction band and can capture electrons, making them less available for conduction. The acceptor level is close to the valence band and can capture holes, making it less available for conduction.

In the Se-rich samples, panels a) of figures 5.61 and 5.62 adding chalcogenides atoms results in some cases in shifting the Fermi level down in the VB resulting in p-type conduction as in 5.61 panel a) 3 and 5 % of the S-doped and in 3, 5, 7

and 15 % of the Te-doped. Specifically, for 15% of Te, the energy between the first and second valence bands is small. Therefore, it is, in principle, easy to achieve a two-band conduction. This situation often occurs due to strong p-type doping, where excess holes shift the Fermi level down.

As mentioned, we also observe p-type conduction at 3% and 5% of S in a-$Ge_{40}Se_{60}$. At 3% of S, the acceptor level is due to the Se-Se bond, and at 5% of S, the acceptor level is due to a tetrahedron see figures 5.63 and 5.64. In the stoichiometric sample, see figure 5.61 (panels b), adding S results in a cleaner spectral band gap at all dopant concentrations. In contrast, adding the Te atoms to stoichiometric samples results in a narrow-gap semiconductor with multiple mid-gap states. This has been observed in the case of GeTe, as confirmed by modulated photocurrent (MPC) experiments [Luc+13] [Lon+12] and DFT results [Che+20].

As more chalcogenides atoms are included in the amorphous network, the a-$Ge_{0.6}Se_{0.4}$ stoichiometry loses its metallic character, and the chalcogenides-doped Ge-rich samples resemble more and more the a-$Ge_{50}Se_{50}$ stoichiometry characterized by a distinctive spectral band gap see figures 5.61 and 5.62 panels c). For example, at 15% of S, the amorphous structure can be chemically written as $Ge_{0.34}Se_{0.51}S_{0.15}$.

Herein, we show the structural origin of localized states within the mobility gap. For the sake of conciseness, as mentioned above, we will focus on the structural motif peculiar to the addition of chalcogenides or those not shown in other dopants, even though all structural motifs that give rise to localized states in undoped a-Ge_xSe_{1-x} were found.

Figure 5.66 shows a localized state originating from a pentavalent Ge in the valence band and Ge-Ge π^* bond in the conduction band. The pentavalent Ge has 3 Se and 2 S neighbors. In figure 5.67, the pentacoordinated Ge has a trigonal bipyramidal structural motif and has strained angles between [70 °, 80 °], creating an in-gap state. In the amorphous Si solar cells, this strained region has been demonstrated to be, by [WG08], as important as dangling bonds to create a trap state.

Figures 5.71, 5.68, 5.69, and 5.70 show the origin of localized states in the Te-doped a-Ge_xSe_{1-x}. Besides the well-established geometrical pattern that leads rise to the localized state in the pristine a-Ge_xSe_{1-x}, such as the Se-Se π^* bond in the valence band and Se-Se σ^* bond in the conduction band (see figures 5.70 and 5.65), the Se-LP and the tetrahedra (see figures 5.69 and 5.71), in the chalcogenide-doped amorphous localized state are due to valence alternation pair (see figures 5.68 and 5.71), the chalcogenide-LP (see figure 5.69), chalcogenide bond (see figure 5.70), the Ge-Ge bond (see figure 5.70). No substitutional doping is observed in chalcogen-doped

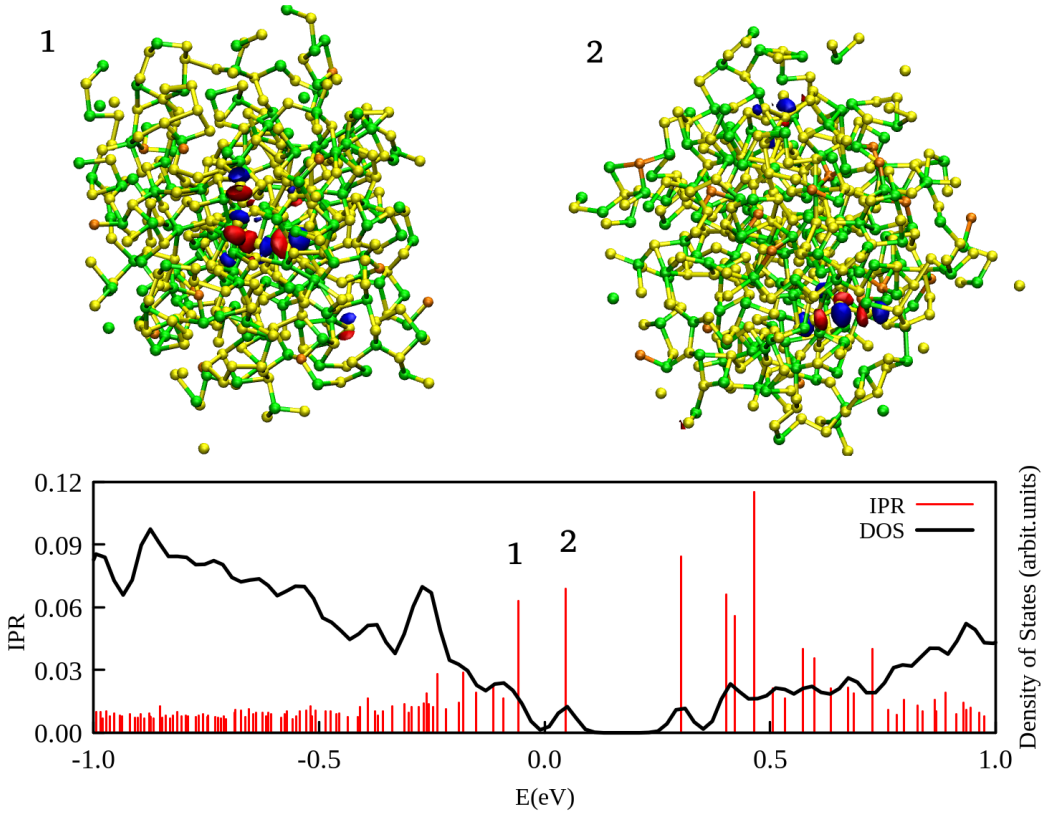

Figure 5.63: Top graphs: single-particle wave functions plots of selected defect states in the mobility gap of Te-doped a-$Ge_{40}Se_{60}$ at 3%. Red (blue) isosurfaces indicate the single-particle wave function's positive (negative) sign. The bottom curves are the density of states (black) and the inverse participation ratio (red) of a-$Ge_{40}Se_{60}$ at 3%, showing p-type conduction. The localized state is due to 1) Se-LP, and 2) the acceptor level is due to Se-Se σ^*.

a-Ge_xSe_{1-x}, in contrast to pnictogen- and crystallogen(Si)-doped samples. The peculiarity of the chalcogenide-doped a-Ge_xSe_{1-x} lies in the formation of VAPs.

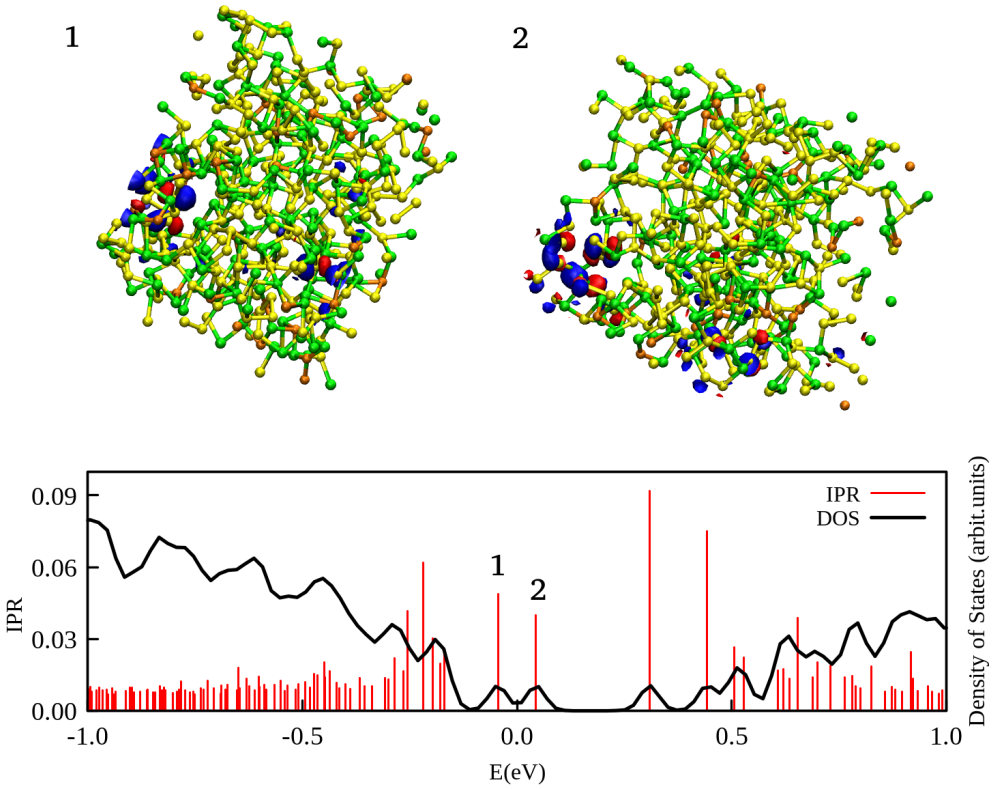

Figure 5.64: Top graphs: single-particle wave functions plots of selected defect states in the mobility gap of Te-doped a-$Ge_{40}Se_{60}$ at 5%. Red (blue) isosurfaces indicate the single-particle wave function's positive (negative) sign. The bottom plots are the density of states (black) and the inverse participation ratio (red) of Te-doped a-$Ge_{40}Se_{60}$ at 5%, showing p-type conduction. The localized state is due to 1) the Se-Se π^* bond and 2) the acceptor level is due to a Ge-centered tetrahedron.

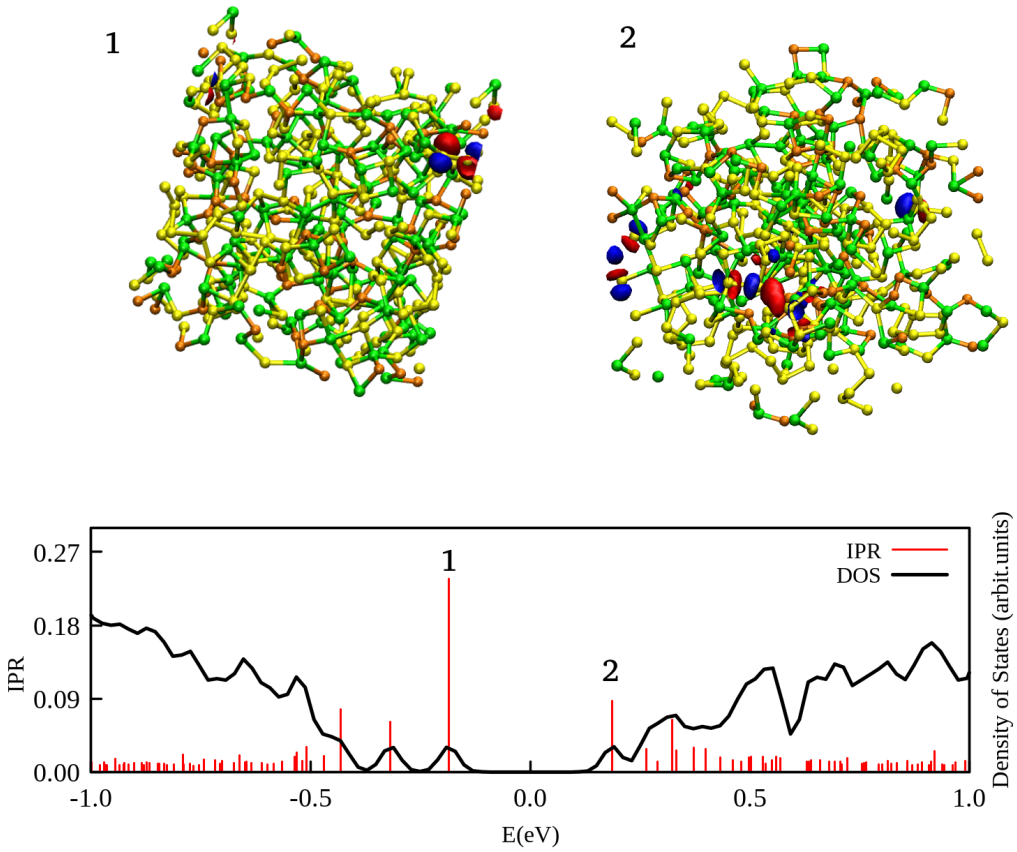

Figure 5.65: The top graphs show single-particle wave function plots of selected defect states in the mobility gap of S-doped a-$Ge_{0.4}Se_{0.6}$ at 15 %. Red (blue) isosurfaces indicate the single-particle wave function's positive (negative) sign. The bottom curves are the density of states (black) and the inverse participation ratio (red) of the a-$Ge_{0.4}Se_{0.6}$ at 15 % of S; the localized states are due to 1) and 2) Se-Se π^* and σ bonds, respectively.

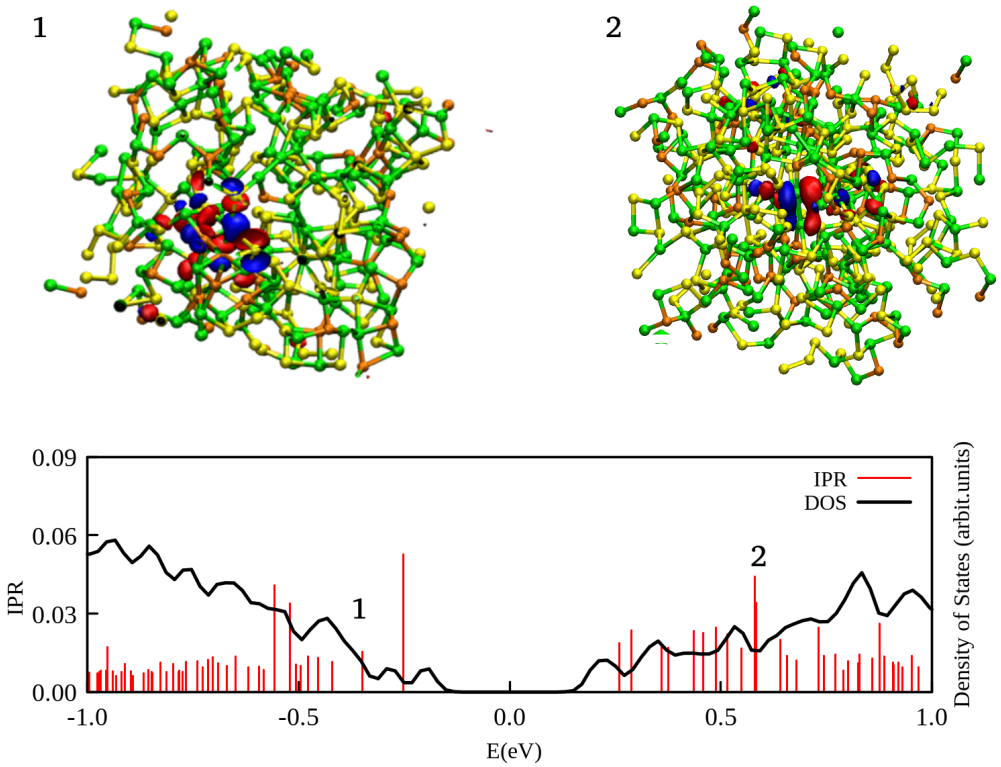

Figure 5.66: The top graphs show single-particle wave function plots of selected defect states in the mobility gap of S-doped a-$Ge_{0.5}Se_{0.5}$ at 15 %. Red (blue) isosurfaces indicate the single-particle wave function's positive (negative) sign. The bottom curves show the density of states (black) and the inverse participation ratio (red spikes) of the a-$Ge_{0.5}Se_{0.5}$ at 15% of S; the localized states are due to: 1) pentavalent Ge with 3 Se and 2 S neighbors and 2) Ge-Ge π bonding.

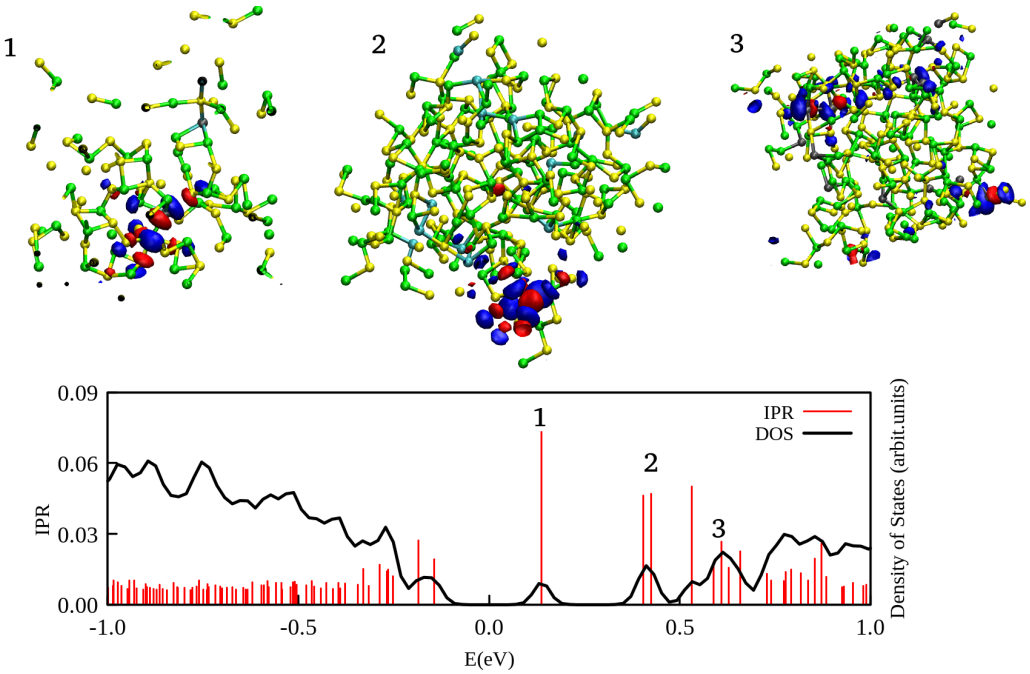

Figure 5.67: The top graphs show single-particle wave function plots of selected defect states in the mobility gap of Te-doped a-$Ge_{0.5}Se_{0.5}$ at 5 %. Red (blue) isosurfaces indicate the single-particle wave function's positive (negative) sign. The bottom curves show the density of states (black) and the inverse participation ratio (red) of the a-$Ge_{0.5}Se_{0.5}$ at 5%; the localized states are due to: 1) pentavalent Ge binding to 4 Se atoms and 1 Te atom. Certain atoms were removed to enhance the visualization of the structural motif responsible for the localized state, 2) Ge-centered tetrahedron, and 3) Te-Te bond

.

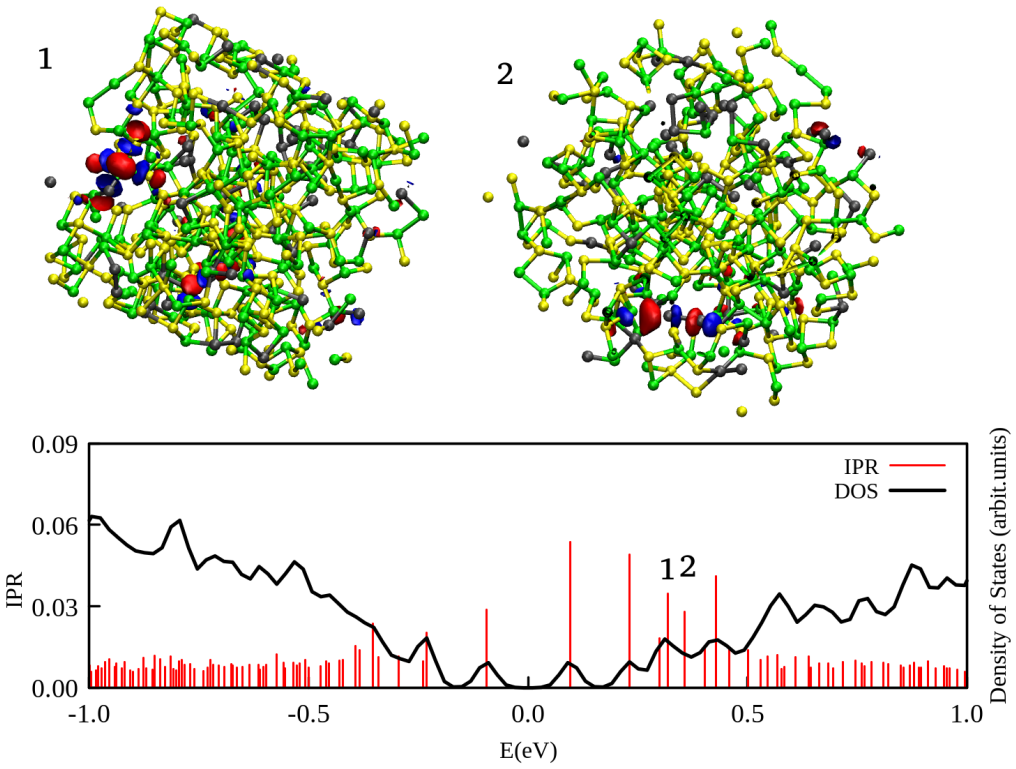

Figure 5.68: The top graphs show single-particle electronic wave function plots of selected defect states in the mobility gap of Te-doped a-$Ge_{0.5}Se_{0.5}$ at 10 %. Red (blue) isosurfaces indicate the single-particle wave function's positive (negative) sign. The bottom curves show density of states (black) and the inverse participation ratio (red spikes) of the a-$Ge_{0.5}Se_{0.5}$ at 10%; the localized states are due to the valence alternation pair: 1) a 3-fold-coordinated Te and 2) a singly coordinated chalcogen.

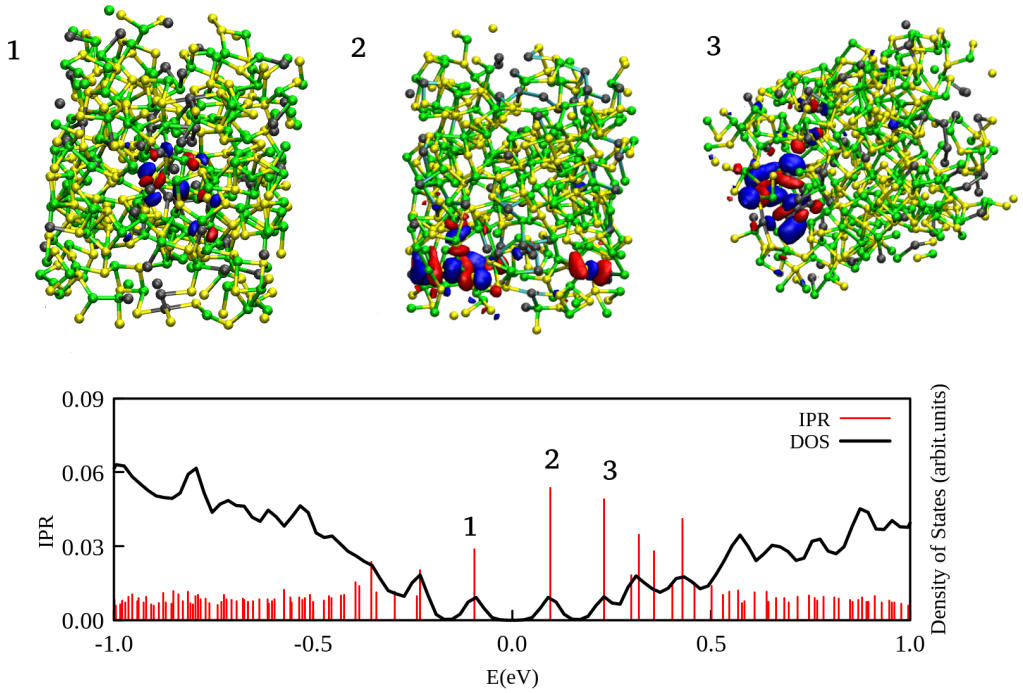

Figure 5.69: The top graphs show electronic wave function plots of selected defect states in the mobility gap of Te-doped a-$Ge_{0.5}Se_{0.5}$ at 10 %. Red (blue) isosurfaces indicate the single-particle wave function's positive (negative) sign. The bottom graph show the density of states (black) and the inverse participation ratio (red) of the a-$Ge_{0.5}Se_{0.5}$ at 10 %; the localized states are due to: 1) Ch-LP, 2) Ge-tetrahedra, 3) Ge-centered tetrahedron with an corner forming a Te-Te bond with the Te adjacent atom.

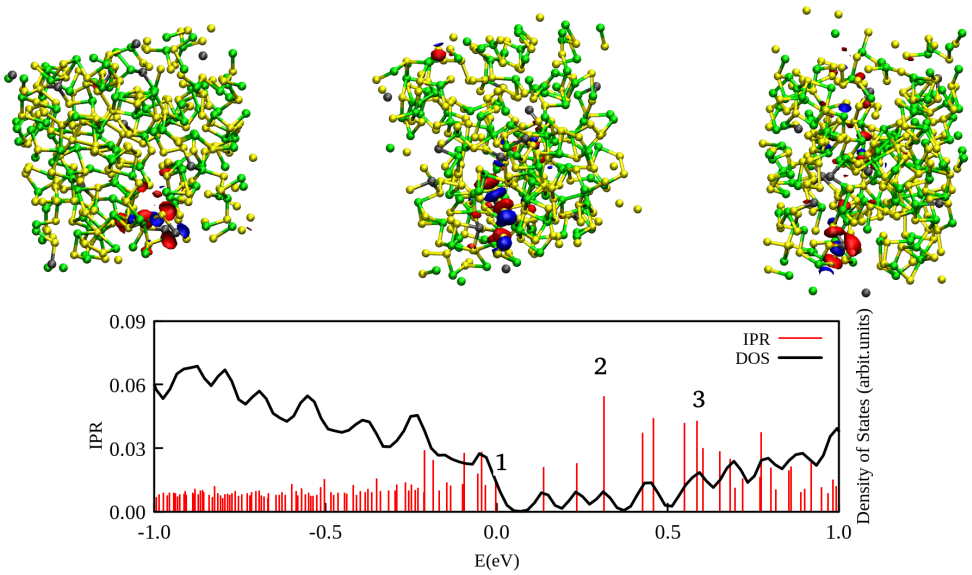

Figure 5.70: The top graphs show electronic wave function plots of selected defect states in the mobility gap of Te-doped a-$Ge_{0.4}Se_{0.6}$ at 3 %. Red (blue) isosurfaces indicate the single-particle wave function's positive (negative) sign. The bottom graph show the density of states (black) and the inverse participation ratio (red) of the a-$Ge_{0.4}Se_{0.6}$ at 3 %; the localized states are due to: 1) Te-Se bond, 2) Se-Se bond, and 3) Te-Se bond.

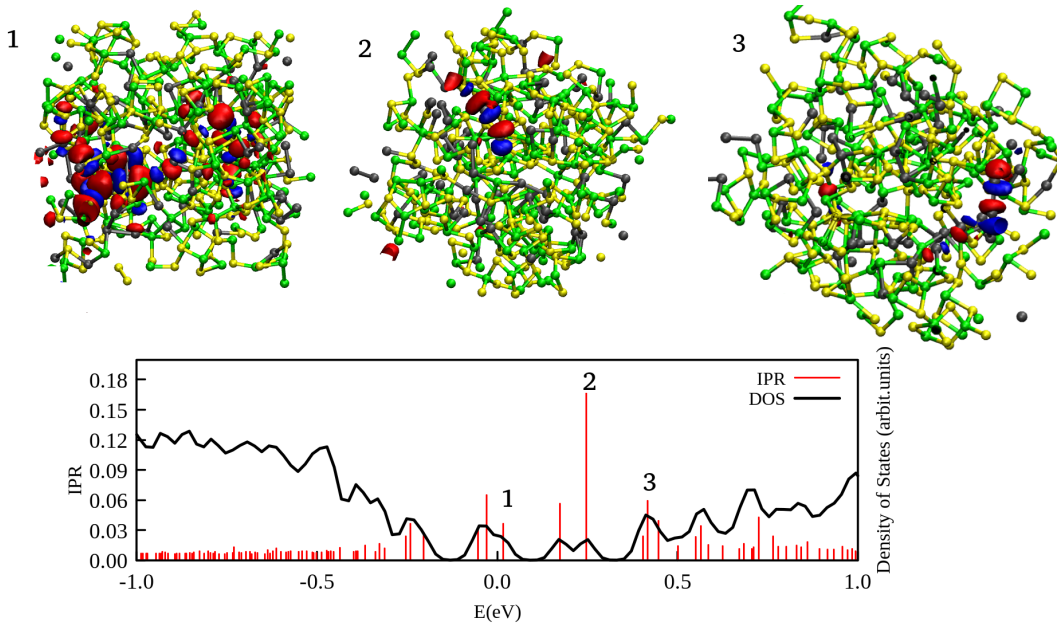

Figure 5.71: The top graphs show electronic wave function plots of selected defect states in the mobility gap of Te-doped a-$Ge_{0.5}Se_{0.5}$ at 15 %. Red (blue) isosurfaces indicate the single-particle wave function's positive (negative) sign. The bottom panel show the density of states (black) and the inverse participation ratio (red) of the a-$Ge_{0.5}Se_{0.5}$ at 15 %. The localized states are due to 1) Ge-centered tetrahedron, 2) valence alternation pair: 1 fold Te, the Te is singly coordinated up to a cut-off of 3.1 Å which is far belong the first neighbor shell as we can see from the RDF 5.45 and 3) VAP: trivalent Te.

Summary

The Ge-Ge RDFs in S- and Te-doped a-$Ge_{0.5}Se_{0.5}$ and a-$Ge_{0.4}Se_{0.6}$ mainly show second-neighbor shells, while in a-$Ge_{0.6}Se_{0.4}$, Ge-Ge bonds are more prominent. As S concentration increases, Se-Se bonds become more prominent in the doped samples. The S-Se RDFs resemble Se-Se RDFs, and no S-S bonds are detected in any stoichiometry.

Se-Se bonds form predominantly in Te-doped a-$Ge_{0.4}Se_{0.6}$ but remain second-neighbor shells at low concentrations of S in the stoichiometric sample. Ge-Se RDFs show well-defined peaks at 2.5 Å, with MRO observed only in the Ge-rich sample at low Te concentrations. Te-Ge RDFs show first-neighbor peaks, and Te-Se bonds appear in a-$Ge_{0.4}Se_{0.6}$ but not in the Ge-rich sample (only Te-Ge bonds exist). The Te-Te bond is observed in a-$Ge_{0.5}Se_{0.5}$ stoichiometry at high Te concentrations, with bond distances matching literature values for elemental Te.

In the Ge-centered ADFs we notice trigonal pyramidal structure, while Se-centered ADF, we observe a border distribution indicating a large electronegative difference between Ge and Se. As S concentration increases, the ADF broadens due to S higher electronegativity compared to Se.

Ge-centered ADFs in all stoichiometries display greater symmetry in the Te-doped samples, with broader distributions in Se-rich and Ge-rich samples. Se-centered ADFs show a bump at 90°and a broad tail at larger angles in the stoichiometric sample. When the Ge and Se content increases, the probability of finding larger angles increases, indicating the formation of more tetrahedra structural motifs. As Te concentration increases, the distribution flattens, indicating low coordination of Te and its preference to bond with Ge rather than Se. The Te-centered ADFs in Se-rich and stoichiometric samples show flatter angles, suggesting the presence of a bent (V-shaped) Te chain structure.

In the stoichiometric and Se-rich S-doped samples, Ge are predominantly 3- and 4-fold coordinated and the relative proportion change with the dopant concentration, while in the Ge-rich sample, Ge is mostly 4-fold coordinated. Se shows primary 3-fold coordination in the stoichiometric and Ge-rich samples, and in Se-rich samples, Se is mainly 2- and 3-fold coordinated. S is primarily 3-fold coordinated in all compositions.

In addition to the specificities found in S-doped a-Ge_xSe_{1-x}, Te atoms are found in 1-fold coordination in some cases, suggesting the presence of valence alternation pairs.

Several molecular structures exist in a-Ge_xSe_{1-x}, including tetrahedra ($Ge(Se_{1/2})_4$), trigonal bipyramidal, see-saw configurations, and an ethane-like $Ge_2(Se_{1/2})_6$ struc-

ture. These molecular structures are at the origin of the localized state in the mobility gap.

In S- and Te-doped a-Ge_xSe_{1-x}, we observe the formation of a distinct molecular arrangement, the germanium chalcogenide cubane (Ge_4Ch_4). This structure features four Ge atoms and four chalcogen atoms positioned at the corners of a cube, forming an ordered pattern within the otherwise disordered material. In this cuboid configuration, the Ge atoms are positively charged, while the chalcogen atoms are negatively charged. This marks the first identification of the cubane structure in germanium-based amorphous chalcogenides using DFT.

5.5 Conclusions

We used Density Functional Theory to develop realistic DFT-based models of doped a-Ge_xSe_{1-x}. We studied the structural and electronic properties of the generated samples, unveiling the link between localized states and the structural motifs within the amorphous network. Structural analysis revealed that elements with similar electronegativity tend to behave similarly when interacting with Ge or Se. Table 5.1 summarizes our main findings regarding the structural and electronic properties of doped a-Ge_xSe_{1-x}.

We demonstrate dopant-induced modifications at the edge of the band, pushing the Fermi level from the middle of the gap towards the valence or conduction band, thereby introducing p- and n-type dopants into the amorphous network. However, as in the undoped case, dopants can stabilize the Fermi level at its intrinsic position, implying that some of them act as defect compensators. Adding P and As passivates Ge dangling bonds in the amorphous network and pushes the edge states deeper into the conduction band, increasing the material's mobility gap. This results in a decrease in the number of traps contributing to conduction.

We observe substitutional doping for Si- and pnictogen-doped a-Ge_xSe_{1-x}. In contrast, no substitutional doping occurs for S and Te dopants, but chalcogen lone pairs, bonds, and valence alternation pairs lead to localized states.

Dopant	Se-rich	Stoichiometric	Ge-rich
Crystallogen	Structural: Si behaves like Ge Electronic: LS mostly near the CB	Structural: Si behaves like Ge Electronic: Similar to undoped a-$Ge_{0.6}Se_{0.4}$	Structural: Si behaves like Ge Electronic: Reduces the metallic character
Pnictogen	Structural: Pnictogen behaves similar to Ge Electronic: LS mostly at the edge of CB	Structural: RDF doesn't change significantly Electronic: LS mostly at the edge of CB	Structural: Pnictogen behaves like Se Electronic: As results in metallic-like structure; P opens the band gap
Chalcogen	Structural: Chalcogen behaves similar to Se Electronic: LS mostly near the conduction band	Structural: Chalcogen similar to Se Electronic: Increasing S clears spectral BG; Increase Te leads to in-gap states	Structural: Chalcogen behaves like Se Electronic: Reduces Ge-Ge clustering; opening of the band gap

Table 5.1: Behavior of dopants in a-Ge_xSe_{1-x}, LS: Localized States, BG: Band Gap, CB: Conduction Band.

6 Conclusions & Outlook

6.1 Summary

In this thesis, we have developed and presented realistic DFT-based models for a-Ge_xSe_{1-x} (Chapter 3). We studied their structural and electronic properties and revealed the link between them for the undoped systems (Chapter 4) and the crystallogen-, pnictogen-, and chalcogen-doped a-Ge_xSe_{1-x} (Chapter 5). Our results show that the a-Ge_xSe_{1-x} exhibit a clear relationship between the structural and the electronic properties. Even though our approach has been specifically applied to a-Ge_xSe_{1-x}, it can be universally used to characterize and understand defects in amorphous structures.

The structural features, including the radial distribution function, the angle distribution function and the coordination number distribution have been calculated. We found Ge and Se clustering in Ge- and Se-rich structures, respectively. The Ge-rich structures tend to have larger coordination numbers than the Se-rich structures. Our samples are qualitatively incompatible with the chemically ordered random network in which each Ge should be 4-fold coordinated to chalcogen atoms, and the chalcogen is 2-fold. The electronic properties including the inverse partition ratio, the electron occupation, and the density of states have been analyzed and we identify the structural origin of the localized states. The mobility gap decreases with Ge content. The Ge concentration plays a crucial role in determining the different behaviors of materials in terms of their electrical conductivity. More Ge leads to metallic conduction, marked by Ge-Ge bonds spanning the mobility gap. The localized states are mostly due to Se-Se bonds and a minor contribution to the Se lone pairs and tetrahedra.

Moreover, the doping of crystallogen, pnictogen, and chalcogen atoms has revealed a substantial impact on the structural properties and electronic band structures. The dopants behave similarly with their iso-valent hosting ions, with some subtle differences, of which the structural and electronic properties have also been explored. We found a new kind of structural motif, the germanium chalcogenide cubane, symbolizing the presence of structurally ordered assemblies in disordered materials. 2-fold Ge gave rise to a localized state in the dopants. In crystallogen-doped a-GeSe, we observe substitutional doping, as in pnictogen-doped samples.

However, no substitutional doping is found in chalcogenide-doped materials, where instead, we observe a specific type of defect: the Valence Alternation Pair.

Overall, this thesis provides a comprehensive investigation that not only adds to the fundamental understanding of a-Ge_xSe_{1-x} but also offers practical insights that can be utilized in various technological advancements. The specific defects identified, such as the Valence alternation pair, contribute to a deeper understanding of defect in amorphous semiconductors. This knowledge can help in developing strategies for controlling defects to enhance material performance.

6.2 Outlook

Our work lays the foundation for several promising avenues.
The models we generated will be the starting point for future studies concerning the behavior of the a-Ge_xSe_{1-x} in the presence of external fields (the electrical cycling of the device), which determine the device's properties and the suitability of the material for memory selectors. We developed a three-step approach [Sla+23]:

- The experimental setting involves the amorphous GeSe sample preparation, the device fabrication, and the electrical characteristics (I–V) measurement.
- The experimental output is used as the input of specific defect spectroscopy functionality, implemented in the device-oriented modeler Ginestra, which is specifically developed to extract intrinsic material properties and characteristics of the defects (thermal ionization and relaxation energies, distribution within the bandgap) from the electrical measurements.
- The resulting defect mapping is interpreted in terms of ab-initio simulations based on density functional theory.

Another possibility is to make the process in the opposite direction, starting from the results of the ab-initio simulations and going to the interpretation of the electric characteristics of the devices. This approach is being explored with our collaborators at CNR-Nano (Modena), and an article is being prepared.

On the other hand, heat flowing through a solid is critical for the OTS applications. Understanding how the heat flows in crystal GeSe and amorphous Ge_xSe_{1-x}, while changing compositions or doping, is vital for evaluating the device's efficiency. This requires finding electrically conductive materials with a thermal conductivity as low as possible. We have started studying the thermal properties of the crystal and a-Ge_xSe_{1-x} with different theoretical approaches (paper in preparation) to take into account the different physical aspects of the crystal and amorphous materials.

Another possible avenue we have started exploring is using machine learning to correlate localized states and the microscopic structure of our models. To do so, we include information on some global and local descriptors:

- global descriptors:
  - the chemical composition which is represented by a vector consisting of the proportion of the species (p(Ge), p(Se), p(Si), p(P), p(As), p(Te)).
  - the density: number of atoms per unit volume
  - the global radial/angle distribution functions
- local descriptors:
  - the species at the atomic site
  - the electronegativity
  - the number of valence electrons of the atom
  - the local RDF /ADF, centered at one atom.
  - We also used more advanced descriptors to describe the local environment that we obtained with existing software packages such as the SOAP (Smooth Overlap of Atomic Positions).

For the electronic structure, we represented each atom's PDOS as a vector. To focus on the states near the Fermi energy, we multiply the DOS with a Gaussian to enhance the states closer to the Fermi level while smoothing the remaining energy range. Additionally, we add some features (e.g., gap state, Mulliken charge) to the electronic feature vector to predict them directly.

We then have an input vector (structure descriptors) and an output vector (DOS) for each atom. We gather the data for all the samples in this format, divide them into a training set and a test set, and proceed with the usual machine learning.

Using existing code, we start with the most simple machine learning model (linear regression model). Our preliminary result using linear regression can predict the DOS from the structure. With some machine learning techniques (e.g. dimension reduction), we could know which features correlate more to the localized state or the band gap.

List of Publications

Published Article

- A. Slassi, **L.-S. Medondjio**, A. Padovani, F. Tavanti, X. He, S. Clima, D. Garbin, B. Kaczer, L. Larcher, P. Ordejón, A. Calzolari, **Device-to-Materials Pathway for Electron Traps Detection in Amorphous GeSe-Based Selectors.** Adv. Electron. Mater. 2023, 0, 2201224. https://doi.org/10.1002/aelm.202201224

Articles in preparation

- **L.-S. Medondjio**, R. Farris and P. Ordejón, **Electronic and structural properties of amorphous GeSe**, (2024)

- **L.-S. Medondjio**, R. Farris and P. Ordejón, **Electronic and structural properties of doped-amorphous GeSe**, (2024)

- F. Tavanti, A. Padovani, **L.-S. Medondjio**, X. He, S. Clima, D. Garbin, B. Kaczer, L. Larcher, P. Ordejón, A. Calzolari, (2024)

Bibliography

[ACB15] Luis A Agapito, Stefano Curtarolo, and Marco Buongiorno Nardelli. **Reformulation of DFT+U as a Pseudohybrid Hubbard Density Functional for Accelerated Materials Discovery**. *Physical Review X* 5:1 (2015), 011006.

[Adl81] D. Adler. **Defects in Amorphous Chalcogenides and Silicon**. *Journal de Physique Colloques* 42:C4 (1981). Supplement ECU n°10, October 1981, C4–3.

[AE73] F. W. Averill and D. E. Ellis. **An Efficient Numerical Multicenter Basis Set for Molecular Orbital Calculations: Application to $FeCl_4$**. *The Journal of Chemical Physics* 59:12 (Nov. 1973), 6412–6418. ISSN: 0021-9606, 1089-7690. DOI: 10.1063/1.1680020.

[Aga+13] Luis A. Agapito, Andrea Ferretti, Arrigo Calzolari, Stefano Curtarolo, and Marco Buongiorno Nardelli. **Effective and accurate representation of extended Bloch states on finite Hilbert spaces**. *Phys. Rev. B* 88 (16 Oct. 2013), 165127. DOI: 10.1103/PhysRevB.88.165127. URL: https://link.aps.org/doi/10.1103/PhysRevB.88.165127.

[Ahn+13] H. W. Ahn, D. Seok Jeong, B. K. Cheong, H. Lee, H. Lee, S. D. Kim, S. Y. Shin, D. Kim, and S. Lee. **Effect of density of localized states on the ovonic threshold switching characteristics of the amorphous GeSe films**. *Applied Physics Letters* 103:4 (2013).

[And58] P.W. Anderson. **Absence of Diffusion in Certain Random Lattices**. *Physical Review* 109 (1958), 1492–1505.

[And75] P. W. Anderson. **Model for the Electronic Structure of Amorphous Semiconductors**. *Phys. Rev. Lett.* 34 (15 Apr. 1975), 953–955. DOI: 10.1103/PhysRevLett.34.953. URL: https://link.aps.org/doi/10.1103/PhysRevLett.34.953.

[Ang+02] Eduardo Anglada, José M. Soler, Javier Junquera, and Emilio Artacho. **Systematic Generation of Finite-Range Atomic Basis Sets for Linear-Scaling Calculations**. *Physical Review B* 66:20 (Nov. 2002), 205101. ISSN: 0163-1829, 1095-3795. DOI: 10.1103/PhysRevB.66.205101.

[Art+99] E. Artacho, D. Sánchez-Portal, P. Ordejón, A. García, and J. M. Soler. **Linear-Scaling Ab-Initio Calculations for Large and Complex Systems**. *physica status solidi (b)* 215:1 (1999), 809–817. ISSN: 1521-3951. DOI: 10.1002/(SICI)1521-3951(199909)215:1<809::AID-PSSB809>3.0.CO;2-0.

[AT16] Rakesh Aluguri and Tseung Yuen Tseng. **Overview of Selector Devices for 3-D Stackable Cross Point RRAM Arrays**. *IEEE Journal of the Electron Devices Society* 4 (2016), 294–306. URL: https://api.semanticscholar.org/CorpusID:23377857.

[ATB75] R. Azoulay, H. Thibierge, and A. Brenac. **Devitrification characteristics of Ge_xSe_{1-x} glasses**. *Journal of Non-Crystalline Solids* 18 (1975), 33–53. DOI: 10.1016/0022-3093(75)90006-X.

[Ava+17] Naga Sruti Avasarala, B. Govoreanu, K. Opsomer, W. Devulder, S. Clima, C. Detavernier, Marleen van der Veen, Jan Van Houdt, Marc Henys, L. Goux, and G.S. Kar. **Doped GeSe materials for selector applications**. In: *2017 47th European Solid-State Device Research Conference (ESSDERC)*. IEEE. 2017, 168–171. DOI: 10.1109/essderc.2017.8066.

[Ava+22] Naga Sruti Avasarala, B. Govoreanu, K. Opsomer, W. Devulder, S. Clima, C. Detavernier, Marleen van der Veen, Jan Van Houdt, Marc Henys, L. Goux, and G.S. Kar. **Doped GeSe Materials for Selector Applications**. *IEEE* (2022).

[AY77] David Adler and Ellen J Yoffa. **Localized electronic states in amorphous semiconductors**. *Canadian journal of Chemistry* 55:11 (1977), 1920–1929.

[Bag74] B.G. Bagley. "The Nature of the Amorphous State." In: *Amorphous and Liquid Semiconductors*. Ed. by J. Tauc. Springer, 1974, 1–22. DOI: 10.1007/978-1-4615-8705-7_1.

[Bah18] Adam Abdullah Bahishti. **Laser Irradiation Effect & Photoconductivity in Amorphous Semiconductor**. 73, Dhaurahra, Balrampur, India 271604: AIJR Publisher, 2018.

[BBP10] J. F. Binder, P. Broqvist, and A. Pasquarello. *Applied Physics Letters* (2010). DOI: 10.1063/1.3486175. URL: https://doi.org/10.1063/1.3486175.

[BC69] S. K. Bahl and K. L. Chopra. **Electrical and Optical Properties of Amorphous vs Crystalline GeTe Films**. *Journal of Vacuum Science and Technology* 6 (1969), 561.

[Ber64] John Desmond Bernal. **The Bakerian lecture, 1962. The structure of liquids**. *Proceedings of the Royal Society of London. Series A, Mathematical and Physical Sciences* 280:1382 (1964), 299–322.

[Bha+86] K. L. Bhatia, D. P. Gosain, G. Parthasarasthy, E. S. T. Gopal, and A. K. Sharma. **Structural properties of doped n-type amorphous $(GeSe_{3.5})_{100-x}Bi_x$**. *Journal of Materials Science Letters* 5 (1986), 181–182.

[Blo29] Felix Bloch. **Über die Quantenmechanik der Elektronen in Kristallgittern**. *Zeitschrift für Physik* 52:7 (1929), 555–600.

[BO27] M. Born and R. Oppenheimer. **Zur Quantentheorie der Molekeln**. *Annalen der Physik* 389:20 (1927), 457–487.

[Boh13a] Niels Bohr. **On the Constitution of Atoms and Molecules**. *Philosophical Magazine* 26 (1913), 1–25.

[Boh13b] Niels Bohr. **On the Constitution of Atoms and Molecules, Part II: Systems Containing Only a Single Nucleus**. *Philosophical Magazine* 26 (1913), 476–502.

[Boo+86] P Boolchand, J Grothaus, M Tenhover, MA Hazle, and Robert K Grasselli. **Structure of GeS2 glass: Spectroscopic evidence for broken chemical order**. *Physical Review B* 33:8 (1986), 5421.

[Boy50] Samuel Francis Boys. **Electronic Wave Functions - I. A General Method of Calculation for the Stationary States of Any Molecular System**. *Proceedings of the Royal Society of London. Series A. Mathematical and Physical Sciences* 200:1063 (Feb. 1950), 542–554. ISSN: 0080-4630, 2053-9169. DOI: 10.1098/rspa.1950.0036.

[Bur+10] G. W. Burr, M. J. Breitwisch, M. Franceschini, D. Garetto, K. Gopalakrishnan, B. Jackson, B. Kurdi, C. Lam, L. A. Lastras, A. Padilla, B. Rajendran, S. Raoux, and R. S. Shenoy. **Phase Change Memory Technology**. *Journal of Vacuum Science and Technology B* 28:2 (2010), 223–262. DOI: 10.1116/1.3301579.

[CD97] M. Cobb and D. A. Drabold. **Ab initio molecular-dynamics study of liquid $GeSe_2$**. *Physical Review B* 56:6 (1997), 3054.

[CDC96] M. Cobb, D. A. Drabold, and R. L. Cappelletti. **Ab initio molecular-dynamics study of the structural, vibrational, and electronic properties of glassy $GeSe_2$**. *Physical Review B* 54:17 (1996), 12162.

[CFO69] M.H. Cohen, H. Fritzsche, and S.R. Ovshinski. **Simple Band Model for Amorphous Semiconductor Alloys**. *Physical Review Letters* 22 (1969), 1065–1072.

[CFP67] M. H. Cohen, L. M. Falicov, and W. A. Phillips. **Role of correlations in disordered systems**. *Physical Review Letters* 8:8 (1967), 316–318.

[Cha+19] Zheng Chai, Weidong Zhang, Robin Degraeve, Sergiu Clima, Firas Hatem, Jian Fu Zhang, Pedro Freitas, and et al. **Dependence of Switching Probability on Operation Conditions in Ge_xSe_{1-x} Ovonic Threshold Switching Selectors**. *IEEE Electron Device Letters* 40:8 (Aug. 2019), 1269–1272. DOI: 10.1109/LED.2019.2924270. URL: http://dx.doi.org/10.1109/LED.2019.2924270.

[Cha+21] Z. Chai, P. Freitas, W. Zhang, J. F. Zhang, and J. Marsland. **True Random Number Generator Based on Switching Probability of Volatile GeXSe1-X Ovonic Threshold Switching Selectors**. In: *2021 IEEE 14th International Conference on ASIC (ASICON)*. 2021, 1–4. DOI: 10.1109/ASICON52560.2021.9620374.

[Che+18] H. Y. Cheng, W. C. Chien, I. T. Kuo, C. W. Yeh, L. Gignac, W. Kim, E. K. Lai, Y. F. Lin, R. L. Bruce, C. Lavoie, C. W. Cheng, A. Ray, F. M. Lee, F. Carta, C. H. Yang, M. H. Lee, H. Y. Ho, M. BrightSky, and H. L. Lung. **Ultra-High Endurance and Low IOFF Selector based on AsSeGe Chalcogenides for Wide Memory Window 3D Stackable Crosspoint Memory**. In: *2018 IEEE International Electron Devices Meeting (IEDM)*. 2018, 37.3.1–37.3.4. DOI: 10.1109/IEDM.2018.8614580.

[Che+20] Yuhan Chen, Liang Sun, Yuxing Zhou, Getasew M Zewdie, Volker L Deringer, Riccardo Mazzarello, and Wei Zhang. **Chemical understanding of resistance drift suppression in Ge–Sn–Te phase-change memory materials**. *Journal of Materials Chemistry C* 8:1 (2020), 71–77.

[Dio+04] M. Dion, H. Rydberg, E. Schröder, D. C. Langreth, and B. I. Lundqvist. **Title of the Article**. *Physical Review Letters* 92 (2004), 246401. DOI: 10.1103/PhysRevLett.92.246401.

[DM70] E.A. Davis and N.F. Mott. **Conduction in non-crystalline systems V. Conductivity, optical absorption, and photoconductivity in amorphous semiconductors**. *Philosophical Magazine* 22 (1970), 903.

[E77] Sayers D. E. In: *Amorphous and Liquid Semiconductors*. Ed. by 1. E. Spear. Edinburgh: University of Edinburgh, 1977.

[ED01] Jeffrey R. Errington and Pablo G. Debenedetti. **Relationship between structural order and the anomalies of liquid water**. *Nature* 409:6818 (2001), 318–321. DOI: 10.1038/35053024.

[Ell89] S.R. Elliott. **The structure of amorphous hydrogenated silicon and its alloys: A review**. *Advances in Physics* 38:1 (1989), 1–88. DOI: 10.1080/00018738900101092. eprint: https://doi.org/10.1080/00018738900101092. URL: https://doi.org/10.1080/00018738900101092.

[Fon+10] Paul Fons, Alexander V. Kolobov, Milos Krbal, Junji Tominaga, K. S. Andrikopoulos, S. N. Yannopoulos, G. A. Voyiatzis, and T. Uruga. **Phase transition in crystalline GeTe: Pitfalls of averaging effects**. *Physical Review B* 82:15 (2010), 155209. DOI: 10.1103/PhysRevB.82.155209. URL: https://doi.org/10.1103/PhysRevB.82.155209.

[FT74] G. B. Fisher and J. Tauc. In: *Proc 5th Int Conf Amorphous and Liquid Semiconductors*. Ed. by I. Stuke and W. Brenig. London: Taylor & Francis, 1974, 1259.

[FWB79] P. Fuoss, W. Warburton, and A. Bienenstock. **Anomalous scattering determinations of the pair distribution functions in amorphous GeSe**. *Journal of Non-Crystalline Solids* 35-36 (1979), 1233–1238. DOI: 10.1016/0022-3093(80)90366-X.

[Gas79] PH Gaskell. **On the structure of simple inorganic amorphous solids**. *Journal of Physics C: Solid State Physics* 12:21 (1979), 4337.

[GK55] NA Goryunova and BT Kolomiets. **Electrical properties and structure in system of Selenide of Tl, Sb, and As**. *Zhurnal Tekhnicheskoi Fiziki* 25 (1955), 2669.

[Gu+22] R. Gu, M. Xu, C. Qiao, C. Wang, K. Ho, S. Wang, M. Xu, and X. Miao. **How arsenic makes amorphous GeSe a robust chalcogenide glass for advanced memory integration**. *Scripta Materialia* 218 (2022), 114834. DOI: 10.1016/j.scriptamat.2022.114834. URL: https://doi.org/10.1016/j.scriptamat.2022.114834.

[Guo+19] Yuzheng Guo, Huanglong Li, Wei Zhang, and John Robertson. **Structural changes during the switching transition of chalcogenide selector devices**. *Applied Physics Letters* 115:16 (2019), 163503. DOI: 10.1063/1.5125215.

[GV16] Tayfun Gokmen and Yurii Vlasov. **Acceleration of Deep Neural Network Training with Resistive Cross-Point Devices: Design Considerations**. *Frontiers in Neuroscience* 10 (2016), 203376. DOI: 10.3389/fnins.2016.00333. URL: https://doi.org/10.3389/fnins.2016.00333.

[GZ14] Mohsin Ganaie and Mohammad Zulfequar. **Study of Morphological, Electrical and Optical behaviour of Amorphous Chalcogenide Semiconductor**. *Advances in Condensed-Matter and Materials Research* 2014 (2014). DOI: 10.5772/intechopen.90512.

[HAJ06] G. Henkelman, A. Arnaldsson, and H. Jónsson. **A fast and robust algorithm for Bader decomposition of charge density**. *Computational Materials Science* 36:3 (2006), 354–360.

[Hao+16] Shiqiang Hao, Fengyuan Shi, Vinayak P. Dravid, Mercouri G. Kanatzidis, and Christopher Wolverton. **Computational prediction of high thermoelectric performance in hole doped layered GeSe**. *Chemistry of Materials* 28:9 (2016), 3218–3226.

[HK64] P. Hohenberg and W. Kohn. **Inhomogeneous Electron Gas**. *Phys. Rev.* 136 (3B Nov. 1964), B864–B871. DOI: 10.1103/PhysRev.136.B864. URL: https://link.aps.org/doi/10.1103/PhysRev.136.B864.

[Hol+13] R. Holomb, V. Mitsa, S. Akyuz, and E. Akalin. **New ring-like models and ab initio DFT study of the medium-range structures, energy and electronic properties of $GeSe_2$ glass**. *Philosophical Magazine* 93:19 (2013), 2549–2562. DOI: 10.1080/14786435.2013.778426. URL: https://doi.org/10.1080/14786435.2013.778426.

[Hua+13] Ruomeng Huang, Kai Sun, Kian S. Kiang, Ruiqi Chen, Yudong Wang, C.H. De Groot, Behrad Gholipour, Daniel W. Hewak, Andrew L. Hector, and Gillian Reid. **A novel top-down fabrication process for $Ge_2Sb_2Te_5$ phase change material nanowires**. In: *2013 13th Non-Volatile Memory Technology Symposium (NVMTS)*. 2013, 1–4. DOI: 10.1109/NVMTS.2013.6851047.

[Ibe09] James Ibers. **Tellurium in a twist**. *Nature Chemistry* 1:6 (2009), 508. DOI: 10.1038/nchem.350. URL: https://doi.org/10.1038/nchem.350.

[Iel08] Daniele Ielmini. **Threshold switching mechanism by high-field energy gain in the hopping transport of chalcogenide glasses**. *Phys. Rev. B* 78 (3 July 2008), 035308. DOI: 10.1103/PhysRevB.78.035308. URL: https://link.aps.org/doi/10.1103/PhysRevB.78.035308.

[IR60] A. F. Ioffe and A. R. Regel. **Non-crystalline, amorphous and liquid electronic semiconductors**. *Progress in Semiconductors* 4 (1960), 237–291.

[IZ07] Daniele Ielmini and Yuegang Zhang. **Analytical model for subthreshold conduction and threshold switching in chalcogenide-based memory devices**. *Journal of Applied Physics* 102:5 (2007), 54517. DOI: 10.1063/1.2773688.

[Jun+01] J. Junquera, Ó. Paz, D. Sánchez-Portal, and E. Artacho. **Numerical Atomic Orbitals for Linear-Scaling Calculations**. *Phys. Rev. B* 64 (2001), 235111.

[KAF76] Marc Kastner, David Adler, and H Fritzsche. **Valence-alternation model for localized gap states in lone-pair semiconductors**. *Physical Review Letters* 37:22 (1976), 1504.

[KB82] Leonard Kleinman and D. M. Bylander. **Efficacious Form for Model Pseudopotentials**. *Phys. Rev. Lett.* 48 (20 May 1982), 1425–1428. DOI: 10.1103/PhysRevLett.48.1425. URL: https://link.aps.org/doi/10.1103/PhysRevLett.48.1425.

[KF03] I. V. Kalinina and V. P. Fedin. **Cubane Chalcogenide Complexes of Group IV–VI Metals: Synthesis, Structure, and Properties**. *Russian Journal of Coordination Chemistry* 29:9 (2003), 597–615. DOI: 10.1023/a:1025604609072.

[Kon+19] K. Konstantinou, F. C. Mocanu, T.-H. Lee, and S. R. Elliott. **Revealing the Intrinsic Nature of the Mid-Gap Defects in Amorphous $Ge_2Sb_2Te_5$**. *Nature Communications* 10 (2019), 3065. DOI: 10.1038/s41467-019-10967-3.

[Kon+21] A. Konashuk, E. Filatova, A. Sokolov, V. Afanas'ev, M. Houssa, and A. Stesmans. **Structural and Electronic Rearrangement in Ovonic Switching Ge_xSe_{1-x} ($0.4 \leq x \leq 0.72$) Films**. *Solid-State Electronics* 186 (2021), 108084. DOI: 10.1016/j.sse.2021.108084. URL: https://doi.org/10.1016/j.sse.2021.108084.

[KS15] S. Kugler and K. Shimakawa. **Amorphous Semiconductors**. Publisher Name, 2015, 86–116. DOI: 10.1017/cbo9781139094337.0.

[KS65a] W. Kohn and L. J. Sham. **Self-Consistent Equations Including Exchange and Correlation Effects**. *Phys. Rev.* 140 (4A Nov. 1965), A1133–A1138. DOI: 10.1103/PhysRev.140.A1133. URL: https://link.aps.org/doi/10.1103/PhysRev.140.A1133.

[KS65b] W. Kohn and L. J. Sham. **Self-Consistent Equations Including Exchange and Correlation Effects**. *Phys. Rev.* 140 (4A Nov. 1965), A1133–A1138. DOI: 10.1103/PhysRev.140.A1133. URL: https://link.aps.org/doi/10.1103/PhysRev.140.A1133.

[KYW13] D. Kuzum, S. Yu, and H. S. Wong. **Synaptic electronics: materials, devices, and applications**. *Nanotechnology* 24 (38 Sept. 2013). DOI: 10.1088/0957-4484/24/38/382001. URL: https://link.aps.org/doi/10.1103/PhysRevB.41.7892.

[LE11] T. H. Lee and S. R. Elliott. **Ab Initio Computer Simulation of the Early Stages of Crystallization: Application to $Ge_2Sb_2Te_5$ Phase-Change Materials**. *Physical Review Letters* 107:14 (2011), 145702. DOI: 10.1103/PhysRevLett.107.145702. URL: https://doi.org/10.1103/PhysRevLett.107.145702.

[LE22] T. H. Lee and S. R. Elliott. **Hypervalency in amorphous chalcogenides**. *Nature Communications* 13:1 (2022), 1–12. DOI: 10.1038/s41467-022-29054-5.

[Liu+16] Ming-Yang Liu, Yang Huang, Qing-Yuan Chen, Chao Cao, and Yao He. **Unexpected electronic structure of the alloyed and doped arsenene sheets: First-Principles calculations**. *Scientific Reports* 6 (July 2016), 29114. DOI: 10.1038/srep29114.

[Liu+19a] D. Liu, L. Xu, J. Xie, and J. Yang. **A Perspective of Chalcogenide Semiconductor-Noble Metal Nanocomposites through Structural Transformations**. *Nano Materials Science* 1 (2019), 184–197.

[Liu+19b] Guangyu Liu, Tao Li, Liangcai Wu, Ying Chen, Bo Liu, Zhongyuan Ma, Sannian Song, and Zhitang Song. **Increasing Trapped Carrier Density in Nanoscale GeSeAs Films by As Ion Implantation for Selector Devices in 3D-Stacking Memory**. *ACS Applied Nano Materials* 2:9 (2019), 5373–5380. DOI: 10.1021/acsanm.9b00734. URL: https://doi.org/10.1021/acsanm.9b00734.

[Liu+19c] Xinyu Liu, Sanghoon Lee, Jacek K. Furdyna, Tengfei Luo, and Yong Hang Zhang. **Chalcogenide: From 3D to 2D and beyond**. Elsevier, 2019, 385. ISBN: 9780081026878.

[Lon+12] Christophe Longeaud, Jennifer Luckas, Daniel Krebs, R Carius, J Klomfass, and Matthias Wuttig. **On the density of states of germanium telluride**. *Journal of Applied Physics* 112:11 (2012).

[LR19] Huanglong Li and John Robertson. **Materials Selection and Mechanism of Non-linear Conduction in Chalcogenide Selector Devices**. *Scientific Reports* 9:1 (2019), 1–9. DOI: 10.1038/s41598-018-37717-x.

[LR20] H. Li and J. Robertson. **A Unified Mid-Gap Defect Model for Amorphous GeTe Phase Change Material**. *Applied Physics Letters* 116:052103 (2020).

[Luc+13] Jennifer Luckas, Daniel Krebs, Stephanie Grothe, Josef Klomfaß, Reinhard Carius, Christophe Longeaud, and Matthias Wuttig. **Defects in amorphous phase-change materials**. *Journal of Materials Research* 28:9 (2013), 1139–1147.

[Luc72] G. Lucovsky. **Optic Modes in Amorphous As_2S_3 and As_2 Se_3**. *Phys. Rev. B* 6 (4 Aug. 1972), 1480–1489. DOI: 10.1103/PhysRevB.6.1480. URL: https://link.aps.org/doi/10.1103/PhysRevB.6.1480.

[LZF17] M. Lai, X. Zhang, and F. Z. Fang. **Crystal Orientation Effect on the Subsurface Deformation of Monocrystalline Germanium in Nanometric Cutting**. *Nanoscale Research Letters* 12 (2017), 296.

[MD71] N. F. Mott and E. A. Davis. **Electronic Processes in Non-Crystalline Materials**. Oxford, England: Clarendon Press, 1971.

[Mea90] Carver Mead. **Neuromorphic electronic systems**. *Proceedings of the IEEE* 78:10 (1990), 1629–1636. DOI: 10.1109/5.58356.

[Mer+14] P. A. Merolla, J. V. Arthur, R. Alvarez-Icaza, A. S. Cassidy, J. Sawada, F. Akopyan, B. L. Jackson, N. Imam, C. Guo, Y. Nakamura, B. Brezzo, I. Vo, S. K. Esser, R. Appuswamy, B. Taba, A. Amir, M. D. Flickner, W. P. Risk, R. Manohar, and D. S. Modha. **A million spiking-neuron integrated circuit with a scalable communication network and interface**. *Science* 345 (6197 Aug. 2014), 668–673. DOI: 10.1126/science.1254642.

[MO71] J. M. Marshall and A. E. Owen. **Drift mobility studies in vitreous arsenic triselenide**. *Philosophical Magazine* 24 (1971), 1281–1290.

[Mot67] N. F. Mott. **Electrons in disordered structures**. *Advances in Physics* 16:64 (1967), 49–144. DOI: 10.1080/00018736700101265.

[Mot98] Nevill Mott. **Reminiscences and Appreciations**. Ed. by E. A. Davis. 1st Edition. London: CRC Press, 1998, 368. ISBN: 9780429204678. DOI: 10.4324/9780203484395.

[MP08] C. Massobrio and A. Pasquarello. **Short and intermediate-range order in amorphous $GeSe_2$**. *Physical Review B* 77:14 (2008), 144207.

[MP76] Hendrik J. Monkhorst and James D. Pack. **Special points for Brillouin-zone integrations**. *Physical Review B* 13:12 (1976), 5188–5192. DOI: 10.1103/physrevb.13.5188.

[MPC01] Carlo Massobrio, Alfredo Pasquarello, and Roberto Car. **Short-and intermediate-range structure of liquid GeSe 2**. *Physical Review B* 64:14 (2001), 144205.

[MS92] Juana Moreno and José M. Soler. **Optimal meshes for integrals in real- and reciprocal-space unit cells**. *Phys. Rev. B* 45 (24 June 1992), 13891–13898. DOI: 10.1103/PhysRevB.45.13891. URL: https://link.aps.org/doi/10.1103/PhysRevB.45.13891.

[MT61] N. F. Mott and W. D. Twose. **Advantages of a Periodic Lattice of Dislocations**. *Advances in Physics* 10:38 (1961), 107–203.

[NRV81] P. Nagels, M. Rotti, and S. Vikhrov. **Doping of chalcogenide glasses in the Ge-Se and Ge-Te systems**. *J. Phys. Colloques* 42:C4 (1981), C4-907–C4-910. DOI: 10.1051/jphyscol:19814197. URL: https://doi.org/10.1051/jphyscol:19814197.

[NS75] E. A. Davis N. F. Mott and R. A. Street. **States in the gap and recombination in amorphous semiconductors**. *The Philosophical Magazine: A Journal of Theoretical Experimental and Applied Physics* 32:5 (1975), 961–996. DOI: 10.1080/14786437508221667. URL: https://doi.org/10.1080/14786437508221667.

[ORK81] E. P. O'Reilly, J. Robertson, and M. J. Kelly. **The Structure of Amorphous GeSe and GeTe**. *Solid State Commun.* 38 (1981), 565–568.

[Oya+81] H. Oyanagi, K. Tanaka, S. Hosoya, and S. Minomura. **EXAFS Studies on the Local Structure in Amorphous GeS and GeSe**. *Journal de Physique Colloques* 42:C4 (1981). JPA-00220903, C4-221–C4-224. DOI: 10.1051/jphyscol:1981446. URL: https://doi.org/10.1051/jphyscol:1981446.

[Pay+92] M. C. Payne, M. P. Teter, D. C. Allan, T. A. Arias, and J. D. Joannopoulos. **Iterative minimization techniques for ab initio total-energy calculations: molecular dynamics and conjugate gradients**. *Rev. Mod. Phys.* 64 (4 Oct. 1992), 1045–1097. DOI: 10.1103/RevModPhys.64.1045. URL: https://link.aps.org/doi/10.1103/RevModPhys.64.1045.

[PBE96] John P. Perdew, Kieron Burke, and Matthias Ernzerhof. **Generalized Gradient Approximation Made Simple**. *Phys. Rev. Lett.* 77 (18 Oct. 1996), 3865–3868. DOI: 10.1103/PhysRevLett.77.3865. URL: https://link.aps.org/doi/10.1103/PhysRevLett.77.3865.

[PCR18] Andrew Pinkard, Anouck M. Champsaur, and Xavier Roy. **Molecular Clusters: Nanoscale Building Blocks for Solid-State Materials**. *Accounts of Chemical Research* 51:4 (2018). Copyright © 2018 American Chemical Society. This publication is licensed under these Terms of Use., 919–929. DOI: 10.1021/acs.accounts.8b00016. URL: https://doi.org/10.1021/acs.accounts.8b00016.

[Per+82] John P. Perdew, Robert G. Parr, Mel Levy, and Jose L. Balduz. **Density-Functional Theory for Fractional Particle Number: Derivative Discontinuities of the Energy**. *Phys. Rev. Lett.* 49 (23 Dec. 1982), 1691–1694. DOI: 10.1103/PhysRevLett.49.1691. URL: https://link.aps.org/doi/10.1103/PhysRevLett.49.1691.

[Phi79] J. C. Phillips. **Topology of Covalent Non-Crystalline Solids I: Short-Range Order in Chalcogenide Alloys**. *Journal of Non-Crystalline Solids* 34 (1979), 153–181.

[PL83] John P. Perdew and Mel Levy. **Physical Content of the Exact Kohn-Sham Orbital Energies: Band Gaps and Derivative Discontinuities**. *Phys. Rev. Lett.* 51 (20 Nov. 1983), 1884–1887. DOI: 10.1103/PhysRevLett.51.1884. URL: https://link.aps.org/doi/10.1103/PhysRevLett.51.1884.

[Pol71] D. E. Polk. **Structural model for amorphous silicon and germanium**. *Journal of Non-Crystalline Solids* 5:5 (1971), 365–376. ISSN: 0022-3093. DOI: 10.1016/0022-3093(71)90038-X. URL: https://www.sciencedirect.com/science/article/pii/002230937190038X.

[PSV80] M. Popescu, H. Stotzel, and L. Vescan. In: *Proc Int Conf Amorp Semicond'80*. Vol. 1. Chisinau, 1980, 44.

[PZ81] J. P. Perdew and Alex Zunger. **Self-interaction correction to density-functional approximations for many-electron systems**. *Phys. Rev. B* 23 (10 May 1981), 5048–5079. DOI: 10.1103/PhysRevB.23.5048. URL: https://link.aps.org/doi/10.1103/PhysRevB.23.5048.

[Rat+01] J. Y. Raty, V. V. Godlevsky, J. P. Gaspard, C. Bichara, M. Bionducci, R. Bellissent, R. Céolin, J. R. Chelikowsky, and P. Ghosez. **Distance Correlations and Dynamics of Liquid GeSe: An Ab Initio Molecular Dynamics Study**. *Physical Review B* 64:23 (2001), 235209. DOI: 10.1103/PhysRevB.64.235209.

[RJ10] S. Le Roux and P. Jund. **Ring statistics analysis of topological networks: New approach and application to amorphous GeS_2 and SiO_2 systems**. *Computational Materials Science* 49:1 (2010), 70–83. DOI: 10.1016/j.commatsci.2010.04.023. URL: https://doi.org/10.1016/j.commatsci.2010.04.023.

[RS09] G. Román-Pérez and J. M. Soler. **Title of the Article by Román-Pérez and Soler**. *Physical Review Letters* 103:9 (2009), 096102. DOI: 10.1103/PhysRevLett.103.096102.

[Rut11] Ernest Rutherford. **The Scattering of α and β Particles by Matter and the Structure of the Atom**. *Philosophical Magazine* 21 (1911), 669–688.

[Rut19] Ernest Rutherford. **Nuclear Constitution of Atoms**. *Proceedings of the Royal Society A* 97 (1919), 374–400.

[Rut20] Ernest Rutherford. **The Origin of the α and β Particles in the Scattering of Polonium Particles**. *Proceedings of the Royal Society A* 97 (1920), 374–400.

[San+07] E. Sanville, S. D. Kenny, R. Smith, and G. Henkelman. **An improved grid-based algorithm for Bader charge allocation**. *Journal of Computational Chemistry* 28:5 (2007), 899–908.

[SBS87] M. Stutzmann, D. K. Biegelsen, and R. A. Street. **Detailed investigation of doping in hydrogenated amorphous silicon and germanium**. *Phys. Rev. B* 35 (11 Apr. 1987), 5666–5701. DOI: 10.1103/PhysRevB.35.5666. URL: https://link.aps.org/doi/10.1103/PhysRevB.35.5666.

[Seo+14] Juhee Seo, Hyung-Woo Ahn, Sang-yeol Shin, Byung-ki Cheong, and Suy-oun Lee. **Anomalous reduction of the switching voltage of Bi-doped Ge0.5Se0.5 ovonic threshold switching devices**. *Applied Physics Letters* 104:15 (2014), 153503. DOI: 10.1063/1.4871385.

[Set+18] M. J. van Setten, M. Giantomassi, E. Bousquet, M. J. Verstraete, D. R. Hamann, X. Gonze, and G.-M. Rignanese. **The PseudoDojo: Training and Grading a 85 Element Optimized Norm-Conserving Pseudopotential Table**. *Computer Physics Communications* 226 (2018), 39–54. DOI: 10.1016/j.cpc.2018.01.012.

[Shi+14] S. Y. Shin, J. M. Choi, J. Seo, H. W. Ahn, Y. G. Choi, B. Cheong, and S. Lee. **The effect of doping Sb on the electronic structure and the device characteristics of Ovonic Threshold Switches based on Ge-Se**. *Scientific Reports* 4 (2014), 7099.

[Sin+17] Arunima K. Singh, Lan Zhou, Aniketa Shinde, Santosh K. Suram, Joseph H. Montoya, Donald Winston, John M. Gregoire, and Kristin A. Persson. **Electrochemical Stability of Metastable Materials**. *Chemistry of Materials* (2017). DOI: 10.1021/acs.chemmater.7b03980.

[Sis+17] Mattia Sist, Carlo Gatti, Peter Nørby, Simone Cenedese, Hidetaka Kasai, Kenichi Kato, and Bo B. Iversen. **High-Temperature Crystal Structure and Chemical Bonding in Thermoelectric Germanium Selenide (GeSe)**. *Chemistry - A European Journal* (2017). DOI: 10.1002/chem.201700536.

[SL75] W. Spear and P. Le Comber. **Substitutional doping of amorphous silicon**. *Solid State Communications* 17:9 (1975), 1193–1196. DOI: 10.1016/0038-1098(75)90284-7. URL: https://doi.org/10.1016/0038-1098(75)90284-7.

[Sla+23] Ahmed Slassi, Shona Medondjio, Andrea Padovani, Francesco Tavanti, Xianfeng He, Slobodan Clima, Davide Garbin, Ben Kaczer, Luca Larcher, Pablo Ordejón, and Arrigo Calzolari. **Device-to-Materials Pathway for Electron Traps Detection in Amorphous GeSe-Based Selectors**. *Advanced Electronic Materials* 9:4 (2023), 2201224. DOI: 10.1002/aelm.202201224.

[Sla30] J. C. Slater. **Atomic Shielding Constants**. *Physical Review* 36:1 (July 1930), 57–64. ISSN: 0031-899X. DOI: 10.1103/PhysRev.36.57.

[SM75] R.A. Street and N.F. Mott. **States in the Gap in Glassy Semiconductors**. *Physical Review Letters* 35:19 (1975), 1293–1295.

[SN89] Otto F. Sankey and David J. Niklewski. **Ab Initio Multicenter Tight-Binding Model for Molecular-Dynamics Simulations and Other Applications in Covalent Systems**. *Physical Review B* 40:6 (Aug. 1989), 3979–3995. ISSN: 0163-1829. DOI: 10.1103/PhysRevB.40.3979.

[SN91] G. Srinivasan and A. Nigavekar. **Role of dopants in the electronic structure of hydrogenated amorphous silicon**. *Materials Science and Engineering: B* 8:1 (1991), 23–37. DOI: 10.1016/0921-5107(91)90015-N. URL: https://doi.org/10.1016/0921-5107(91)90015-N.

[Sol+02] José M Soler, Emilio Artacho, Julian D Gale, Alberto García, Junquera Javier, Pablo Ordejón, and Daniel Sánchez-Portal. **The SIESTA Method for Ab Initio Order-N Materials Simulation**. *Journal of Physics Condensed Matter* 14:11 (2002), 2745–2779.

[SSA73] R A Street, T M Searle, and I G Austin. **Photoluminescence in amorphous As2S3**. *Journal of Physics C: Solid State Physics* 6:10 (1973), 1830. DOI: 10.1088/0022-3719/6/10/016.

[SSA74a] R. A. Street, T. M. Searle, and I. G. Austin. **Proceedings of the Fifth International Conference on Amorphous and Liquid Semiconductors**. In: *Proceedings of the Fifth International Conference on Amorphous and Liquid Semiconductors*. Ed. by J. Stuke and W. Brenig. London: Taylor and Francis, 1974, 953.

[SSA74b] R. A. Street, T. M. Searle, and I. G. Austin. **Proceedings of the Fifth International Conference on Amorphous and Liquid Semiconductors**. In: *Proceedings of the Fifth International Conference on Amorphous and Liquid Semiconductors*. Ed. by J. Stuke and W. Brenig. London: Taylor and Francis, 1974, 953.

[Ste23] Ken Stewart. *Atomic model*. Encyclopedia Britannica. Accessed 28 10 2023. 2023. URL: https://www.britannica.com/science/atomic-model.

[Str82] R. A. Street. **Doping and the Fermi Energy in Amorphous Silicon**. *Phys. Rev. Lett.* 49 (16 Oct. 1982), 1187–1190. DOI: 10.1103/PhysRevLett.49.1187. URL: https://link.aps.org/doi/10.1103/PhysRevLett.49.1187.

[Tan89] Koichi Tanaka. **Structural Phase Transitions in Chalcogenide Glasses**. *Phys. Rev. B* 39 (1989), 1270–1279. DOI: 10.1103/PhysRevB.39.1270.

[Tav+20] Francesco Tavanti, Behnood Dianat, Alessandra Catellani, and Arrigo Calzolari. **Hierarchical Short- and Medium-Range Order Structures in Amorphous Ge_xSe_{1-x} for Selectors Applications**. *ACS Applied Electronic Materials* 2:9 (2020), 2961–2969. DOI: 10.1021/acsaelm.0c00581. URL: https://doi.org/10.1021/acsaelm.0c00581.

[Tho13a] J.J. Thomson. **Rays of Positive Electricity**. *Philosophical Magazine* 26 (1913), 209–253.

[Tho13b] J.J. Thomson. **Rays of Positive Electricity**. *Proceedings of the Royal Society A* 89 (1913), 1–20.

[Tho97] J.J. Thomson. **Cathode Rays**. *Philosophical Magazine* 44 (1897), 293–316.

[TJD00] M. Thorp, D. Jacbos, and B. Djordjrvic, 95–146. In: *Insulating and Semiconducting Glasses*. Ed. by P. Boolchand. World Scientific, 2000.

[TM91] N. Troullier and José Luís Martins. **Efficient pseudopotentials for plane-wave calculations**. *Physical Review B* 43 (Jan. 1991), 1993. DOI: 10.1103/PhysRevB.43.1993.

[TMT80] Noboru Tohge, Tsutomu Minami, and Masami Tanaka. **Electrical transport in n-type semiconducting $Ge_{120}Bi_xSe_{70-x}Te_{10}$ glasses**. *Journal of Non-Crystalline Solids* 37:1 (1980), 23–30.

[Toh+80] Noboru Tohge, Tsutomu Minami, Yoshitaka Yamamoto, and Masami Tanaka. **Electrical and optical properties of n-type semiconducting chalcogenide glasses in the system Ge-Bi-Se**. *Journal of applied physics* 51:2 (1980), 1048–1053.

[Tro+77] P. Tronc, M. Bensoussan, A. Brenac, and C. Sebenne. **Vibrational Properties of Ge_xSe_{1-x} Glasses: Comments**. *Solid State Communications* 24:1 (1977), 79–80. DOI: 10.1016/0038-1098(77)90570-1. URL: https://doi.org/10.1016/0038-1098(77)90570-1.

[Tro82] H. J. Trodahl. **Far infrared absorption of a-GeSe**. *Solid State Communications* 44:3 (1982), 319–321. DOI: 10.1016/0038-1098(82)90863-8.

[Tro84] H. J. Trodahl. **Vibrational Studies of the Short Range Order in a-Ge_xSe_{1-x} Films**. *J. Phys. C: Solid State Phys.* 17 (1984), 6027–6033.

[TS09] Alexandre Tkatchenko and Matthias Scheffler. **Accurate Molecular Van der Waals Interactions from Ground-State Electron Density and Free-Atom Reference Data**. *Physical Review Letters* 102 (7 2009), 073005. DOI: 10.1103/PhysRevLett.102.073005.

[TSH09] W. Tang, E. Sanville, and G. Henkelman. **A grid-based Bader analysis algorithm without lattice bias**. *Journal of Physics: Condensed Matter* 21:8 (2009), 084204.

[TSS82] T. Takahashi, H. Sakurai, and T. Sagawa. **Photoemission (UPS and XPS) Study of Crystallization of Amorphous GeTe Film**. *Solid State Communications* 44 (1982), 723–726.

[VSD88] C. Vautier, J.M. Saiter, and T. Derrey. **Nature of defects in amorphous Bi-Se alloys**. *Journal of Non-Crystalline Solids* 103:1 (1988), 65–72. DOI: 10.1016/0022-3093(88)90416-4.

[WG08] Lucas K. Wagner and Jeffrey C. Grossman. **Microscopic Description of Light Induced Defects in Amorphous Silicon Solar Cells**. *Phys. Rev. Lett.* 101 (26 Dec. 2008), 265501. DOI: 10.1103/PhysRevLett.101.265501. URL: https://link.aps.org/doi/10.1103/PhysRevLett.101.265501.

[WY19] H. Wang and X. Yan. **Overview of Resistive Random Access Memory (RRAM): Materials, Filament Mechanisms, Performance Optimization, and Prospects**. *Physica status solidi (RRL) – Rapid Research Letters* 13:9 (2019).

[Yan+19] J. Yang, Q. Fan, B. Xiao, and Y. Ding. **Evolution of the Structural, Mechanical, and Phonon Properties of GeSe Polymorphs in a Pressure-Induced Second-Order Phase Transition**. *Materials* 12:21 (2019), 3612. DOI: 10.3390/ma12213612.

[YJ20] Alberto García Nick Papior Arsalan Akhtar Emilio Artacho Volker Blum Emanuele Bosoni Pedro Brandimarte Mads Brandbyge J. I. Cerdá Fabiano Corsetti Ramón Cuadrado Vladimir Dikan Jaime Ferrer Julian Gale Pablo García-Fernández V. M. García-Suárez Sandra García Georg Huhs Sergio Illera Richard Korytár Peter Koval Irina Lebedeva Lin Lin Pablo López-Tarifa Sara G. Mayo Stephan Mohr Pablo Ordejón Andrei Postnikov Yann Pouillon Miguel Pruneda Roberto Robles Daniel Sánchez-Portal Jose M. Soler Rafi Ullah Victor Wen-zhe Yu and Javier Junquera. **Siesta: Recent Developments and Applications.** *The Journal of Chemical Physics* 142:20 (2020), (see pages 23, 86, 108).

[Yoo+18] Sijung Yoo, Chanyoung Yoo, Eui-Sang Park, Woohyun Kim, Yoon Kyeung Lee, and Cheol Seong Hwang. **Chemical Interactions in the Atomic Layer Deposition of Ge–Sb–Se–Te Films and Their Ovonic Threshold Switching Behavior**. *Journal of Materials Chemistry C* 6:18 (2018). CODEN: JMCCCX, 5025–5032. ISSN: 2050-7534. DOI: 10.1039/C8TC01041B.

[YR14] X. Yu and J. Robertson. **Nature of gap states in GeSbTe phase change memory materials**. *Canadian Journal of Physics* 92:7/8 (2014), 671–674. DOI: 10.1139/cjp-2013-0531.

[YSS12] J. Joshua Yang, Dmitri B. Strukov, and Duncan R. Stewart. **Memristive devices for computing**. *Nature Nanotechnology* 8:1 (2012), 13–24. DOI: 10.1038/nnano.2012.240. URL: https://doi.org/10.1038/nnano.2012.240.

[Zac32] W. H. Zachariasen. **The Atomic Arrangement in Glass**. *Journal of the American Chemical Society* 54:10 (1932), 3841–3851.

[Zei+17] Anita Zeidler, Philip S. Salmon, Dean A. J. Whittaker, Keiron J. Pizzey, and Alex C. Hannon. **Topological Ordering and Viscosity in the Glass-Forming Ge–Se System: The Search for a Structural or Dynamical Signature of the Intermediate Phase**. *Frontiers in Materials* 4 (2017), 304563. DOI: 10.3389/fmats.2017.00032.

[Zha+21] Hui Zhang, Jia Wang, Fabien Guégan, Shanshan Yu, and Gilles Frapper. **Prediction of allotropes of tellurium with molecular, one- and two-dimensional covalent nets for photofunctional applications**. *RSC Advances* 11:48 (2021), 29965–29975. DOI: 10.1039/d1ra04997f. URL: https://doi.org/10.1039/d1ra04997f.

[Zhd+79] V. G. Zhdanov, B. T. Kolomiets, V. M. Lyubin, and V. K. Malinovbskii. **Photoinduced Optical Anisotropy in Chalcogenide Vitreous Semiconducting Films**. *Physica Status Solidi A* 52 (1979), 621–626.

[ZKC16] Federico Zipoli, Daniel Krebs, and Alessandro Curioni. **Structural Origin of Resistance Drift in Amorphous GeTe**. *Physical Review B* 93 (11 2016), 115201. DOI: 10.1103/PhysRevB.93.115201.